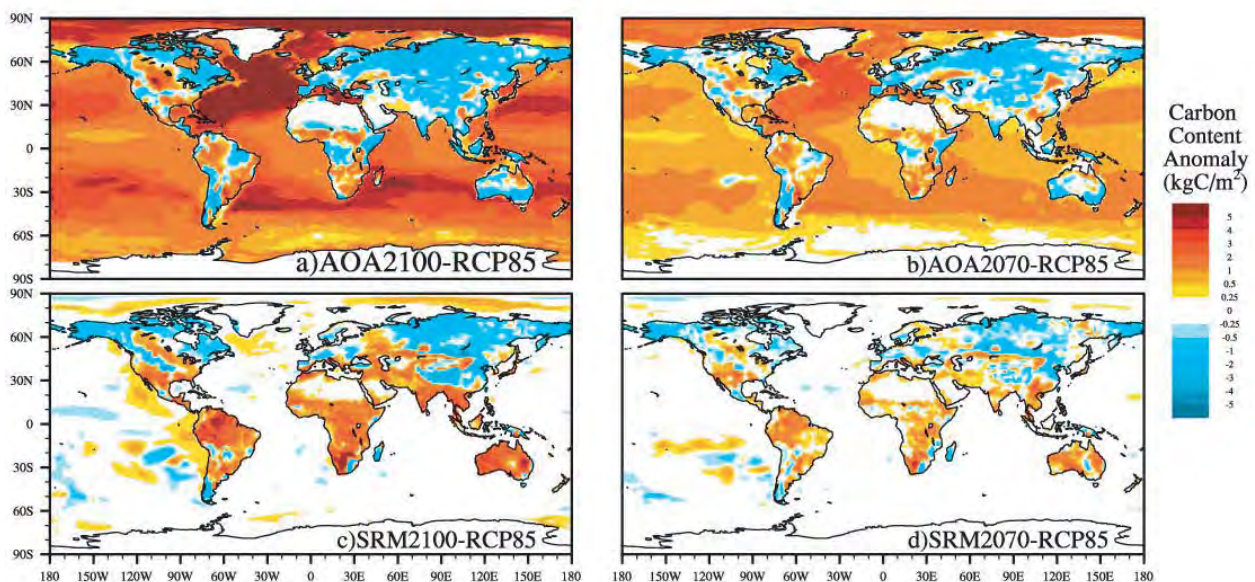# Climate engineering by enhancement of ocean alkalinity: impacts on the Earth system and a comparison with solar radiation management

Miriam Ferrer González

Hamburg 2017

Hinweis

Die Berichte zur Erdsystemforschung werden vom Max-Planck-Institut für Meteorologie in Hamburg in unregelmäßiger Abfolge herausgegeben.

Sie enthalten wissenschaftliche und technische Beiträge, inklusive Dissertationen.

Die Beiträge geben nicht notwendigerweise die Auffassung des Instituts wieder.

Die "Berichte zur Erdsystemforschung" führen die vorherigen Reihen "Reports" und "Examensarbeiten" weiter.

Anschrift / Address

Max-Planck-Institut für Meteorologie
Bundesstrasse 53
20146 Hamburg
Deutschland

Tel./Phone: +49   (0)40 4 11 73 - 0
Fax: +49   (0)40 4 11 73 - 298

name.surname@mpimet.mpg.de
www.mpimet.mpg.de

Notice

The Reports on Earth System Science are published by the Max Planck Institute for Meteorology in Hamburg. They appear in irregular intervals.

They contain scientific and technical contributions, including Ph. D. theses.

The Reports do not necessarily reflect the opinion of the Institute.

The "Reports on Earth System Science" continue the former "Reports" and "Examensarbeiten" of the Max Planck Institute.

Layout

Bettina Diallo and Norbert P. Noreiks
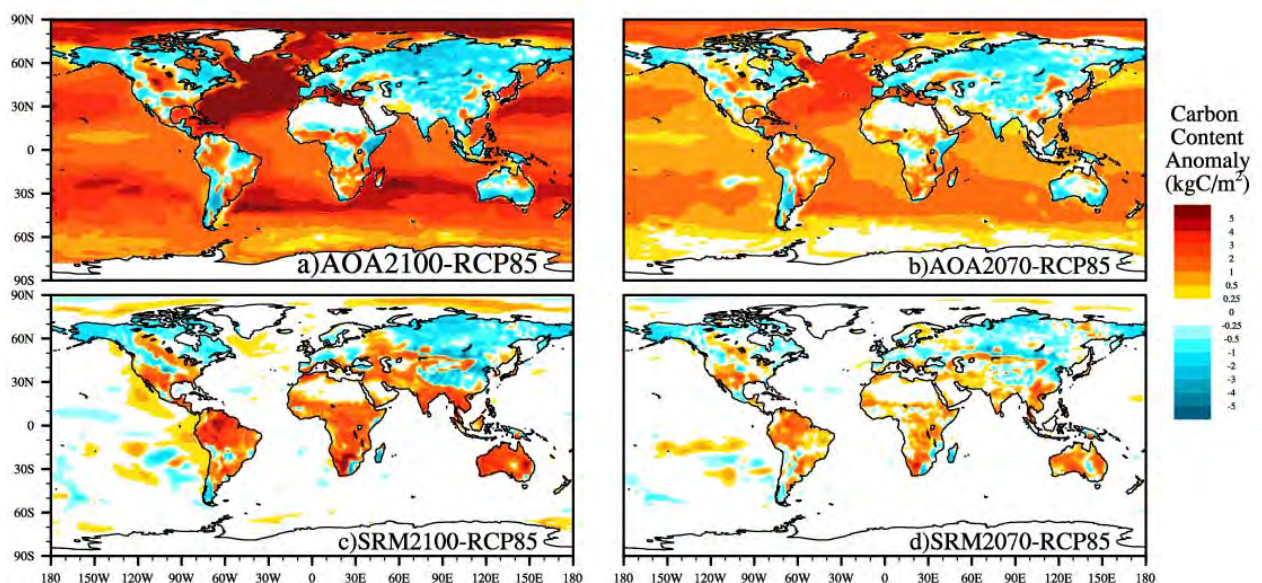Communication

Copyright

Photos below: ©MPI-M
Photos on the back from left to right:
Christian Klepp, Jochem Marotzke,
Christian Klepp, Clotilde Dubois,
Christian Klepp, Katsumasa Tanaka

Climate engineering by enhancement of ocean alkalinity: impacts on the Earth system and a comparison with solar radiation management

Dissertation with the aim of achieving a doctoral degree
at the Faculty of Mathematics, Informatics and Natural Sciences
Department of Earth Sciences of Universität Hamburg

submitted by

Miriam Ferrer González

from Candelaria, Tenerife

Hamburg 2017

Miriam Ferrer González

Max-Planck-Institut für Meteorologie
Bundesstrasse 53
20146 Hamburg

Tag der Disputation: 22.05.2017

Folgende Gutachter empfehlen die Annahme der Dissertation:

Prof. Dr. Johanna Baehr
Dr. Tatiana Ilyina

Abstract

Climate engineering (CE) methods are intended to mitigate the environmental perturbations caused by anthropogenic climate change. Artificial ocean alkalinization (AOA) strengthens the ocean carbon sink whilst decreasing seawater acidity via enhancement of the buffering capacity. Solar radiation management (SRM) by stratospheric sulfur injection tempers surface warming through increasing the Earth's albedo. For the first time, the CE-driven effects on the Earth system of large-scale AOA and SRM scenarios are consistently compared in a comprehensive Earth system model with interactive carbon cycle. Using the Max Planck Institute Earth System Model (MPI-ESM) forced by fossil-fuel CO_2 emissions, I explore the impacts of these CE methods on the global carbon uptake and ocean biogeochemistry. I design and run AOA scenarios that reduce atmospheric CO_2 levels to the trajectory of the Representative Concentration Pathway (RCP) 4.5 in a high CO_2 world following the RCP8.5 scenario. The effects of these large-scale AOA scenarios on the Earth system are analyzed and compared to SRM simulations that target the radiative forcing of the RCP4.5 scenario under RCP8.5 forcing.

Global addition of 114 Pmol of alkalinity into the surface ocean during the 21st century stabilizes atmospheric CO_2 concentration to RCP4.5 levels under RCP8.5 emissions. The entire surface ocean turns into a carbon sink. Half of the CO_2 emitted into the atmosphere (940 GtC) is removed by the ocean, preventing 1.5 K of global warming by 2100. Still, surface temperatures remain 0.5 K higher than the targeted RCP4.5, due to the unmitigated forcing of non-CO_2 agents. The impacts of ocean acidification are largely offset, despite the enhanced carbon sink. However, as a side effect surface seawater pH and Ω exceed regionally historical levels, with potential adverse ecological effects. By 2100, much higher values of pH (up to 0.6 higher units) and Ω (fivefold increase) are reached over the Arctic Ocean while Ω doubles in tropical oceans. After termination of AOA in 2070, the seawater chemical

environment undergoes rapid perturbations: local rates of change in surface pH and Ω become up to one order of magnitude higher than in RCP8.5, being highest over the Arctic Ocean and tropical oceans. The seasonal amplitude of Ω is amplified (threefold increase) by AOA everywhere, except for the Southern Ocean where AOA compensates the projected damping of the seasonal amplitude of Ω in the RCP8.5.

Small differences arise in the ocean biogeochemistry between SRM simulations and the unmitigated RCP8.5 mainly due to the effect of surface seawater temperature on the carbonate chemistry. The small mitigation potential of SRM in terms of atmospheric CO_2 reduction, dominated by the enhanced land sink, completely vanishes within the following decades after termination of SRM. As expected, local rates of surface warming after termination of SRM largely exceed those of the unmitigated RCP8.5 scenario (up to 0.14 K/yr). Termination of large-scale AOA, leads to local rates of warming that are broadly similar to those of the RCP8.5 but spatial patterns differ at high latitudes of the Northern hemisphere. Moreover, in some small regions warming rates become as large as in the terminated SRM scenario, albeit with large internal variability. Biogeochemical variables, such as ocean primary production and oxygen, behave in accordance to the changes in the physicochemical environment brought about by the CE scenarios. Large-scale AOA scenarios reveal that their potential to mitigate changes in the Earth's climate implies an unprecedented perturbation in the seawater chemical environment. Moreover, the termination of large-scale AOA and SRM scenarios induces faster local environmental changes than those intended to alleviate.

Zusammenfassung

Die Anwendung von Climate Engineering (CE)-Methoden hat zum Ziel, eine Abmilderung der negativen Folgen durch den anthropogenen Klimawandel zu bewirken. So führt eine künstliche Alkalinisierung des Ozeans (AOA) zu einer verstärkten ozeanischen Kohlenstoffaufnahme, da die Acidität des Ozeans verringert respektive das Puffervermögen erhöht wird. Bei der Methode des Solar Radiation Management (SRM) bewirkt eine Injektion von Schwefel in die Stratosphäre eine Erhöhung der planetaren Albedo und daraus folgend eine Abkühlung der Erdoberflächentemperatur. In dieser Arbeit werden, zum ersten Mal, die CE-Effekte durch AOA und SRM auf das Erdsystem mit Hilfe eines globalen Erdsystem-Modells mit interaktivem Kohlenstoffkreislauf untersucht. Ich verwende das Erdsystem-Modell des Max-Planck-Instituts für Meteorologie (MPI-ESM), angetrieben durch vorgeschriebene CO_2-Emissionen, um den Einfluss der oben genannten CE-Methoden auf die globale Aufnahme von Kohlenstoff sowie auf die Biogeochemie des Ozeans zu erforschen. Ausgehend von einem hohen CO_2-Emissionsszenario (dem Representative Concentration Pathway (RCP) 8.5 folgend) entwickle und untersuche ich AOA-Szenarien, die die atmosphärische CO_2-Konzentration auf einem deutlich niedrigeren Niveau, entsprechend der Werte der RCP4.5-Trajektorie, halten. Die Auswirkungen dieser grossrätumigen Anwendung der AOA werden analysiert und dann mit SRM-Simulationen verglichen, die, ebenfalls ausgehend von einem RCP8.5-Szenario, einen RCP4.5-Strahlungsantrieb anvisieren.

Der Eintrag von 114 Pmol Alkalinität in die Ozeanoberfläche im Verlauf des 21. Jahrhunderts stabilisiert die atmosphärische CO_2-Konzentration auf das RCP4.5-Niveau, trotz anhaltend hoher Emissionen auf dem Level von RCP8.5. Die gesamte Ozeanoberfläche wird zu einer Kohlenstoffsenke. Die Hälfte des emittierten anthropogenen CO_2 (940 GtC) wird vom Ozean aufgenommen und somit die Erderwärmung um 1.5 Grad Kelvin im Jahr 2100 gemindert. Jedoch sind die Temperaturen an der Erdoberfläche um 0.5 K höher als die in RCP4.5 anvisierten, da die AOA keinen

Einfluss auf andere Treibhausgase, die kein CO_2 sind, hat. Die Auswirkungen der Ozeanversauerung werden grösstenteils ausgeglichen, obwohl eine stärkere Kohlenstoffsenke vorliegt. Allerdings zeigen sich als Nebeneffekt der AOA Höchstwerte von pH und Ω an der Ozeanoberfläche, zu denen es kein historisches Analogon gibt, die aber einen potentiell negativen Einfluss auf die Ozeanökologie haben können. Bis 2100 werden höhere Werte für pH (bis zu +0.6) und Ω (verfünffacht) im arktischen Ozean erreicht. In den tropischen Ozeanen verdoppelt sich Ω. Bei einer Beendigung der AOA im Jahr 2070 erfährt die Biogeochemie des Ozeans rapide Veränderungen: die Änderungsraten von pH und Ω an der Ozeanoberfläche übersteigen die für RCP8.5 prognostizierten Werte um bis zu einer Grössenordnung, mit Maxima im arktischen und den tropischen Ozeanen. Die saisonale Amplitude von Ω wird durch die AOA in allen Regionen erhöht (verdreifacht). Eine Ausnahme bildet der südliche Ozean, wo die AOA eine für RCP8.5 prognostizierte Dämpfung der saisonalen Amplitude von Ω kompensiert.

Kleine Unterschiede in der Biogeochemie des Ozeans zeigen sich zwischen der SRM-Simulation und dem ungemilderten RCP8.5-Szenario. Diese lassen sich durch den Einfluss der Oberflächentemperatur auf den ozeanischen Kohlenstoffkreislauf erklären. Das ohnehin geringe Potential des SRM, die atmosphärischen CO_2-Konzentrationen zu verringern, welches sich im Wesentlichen aus einer Verstärkung der Landbiosphärensenke ergibt, verschwindet vollständig in den folgenden Dekaden nach Beendigung des SRM. Wie erwartet, übersteigen die lokalen Raten der Oberflächenerwärmung nach Beendigung des SRM die Werte des RCP8.5-Szenarios deutlich (bis zu 0.14 K/Jahr). Die Beendigung der AOA führt zu lokalen Erwärmungsraten, die weitestgehend mit denen aus dem RCP8.5-Szenario übereinstimmen, aber das räumliche Verteilungsmuster der Erwärmung in den hohen Breiten der Nordhemisphäre unterscheidet sich. Zudem erreichen die Raten in einzelnen Regionen Werte, die vergleichbar sind mit denen nach Beendigung der SRM-Massnahmen, jedoch mit einer höheren internen Variabilität. Ozeanische biogeochemische Grössen, wie die Primärproduktion oder der Sauerstoffgehalt, verhalten sich entsprechend der physikalisch-chemischen Veränderungen, welche mit den CE-Szenarien assoziiert sind. Es

zeigt sich, dass eine grossräumige Anwendung der AOA zwar das Potential hat, den Klimawandel abzumildern, aber gleichzeitig eine beispiellose Veränderung der ozeanischen Biogeochemie herbeigeführt wird. Zudem verursacht die Beendigung der jeweiligen CE-Massnahme schnellere Umweltveränderungen als die, die durch die Anwendung der CE hätten abgemildert werden sollen.

Contents

Chapter 1

Introduction

1.1 Anthropogenic Climate Change

Since the industrial revolution, 240 GtC of anthropogenic carbon has accumulated in the atmosphere, causing a global warming of 0.78 K (IPCC 2013). If CO_2 emissions follow the Representative Concentration Pathway (RCP) 8.5 scenario, $\sim$1200 GtC may accumulate in the atmosphere, leading to a radiative forcing of 8.5 W/m^2 by the year 2100. Within a century, the global surface temperature would be expected to increase by 4 K. The accumulation of CO_2 in the atmosphere has been tempered by the terrestrial and oceanic sinks (Le Quéré et al. 2015). The enhanced ocean carbon uptake alters the partitioning of the carbonate species in seawater (H_2CO_3, HCO_3^-, CO_3^{2-}), rising the hydrogen ion concentration ($[H^+]$) (Zeebe and Wolf-Gladrow 2001). This is termed *ocean acidification*, and it is measured with the pH scale defined as the negative common logarithm of $[H^+]$ in seawater. In other words, after CO_2 enters the upper ocean, seawater becomes more acidic (i.e. pH decreases) due to the perturbed partitioning of the carbonate species. The concentration of carbonates ($[CO_3^{2-}]$) decreases, leading to a lowering of the saturation state with respect to carbonate minerals (Ω). Following the RCP8.5 scenario, the average surface ocean pH is projected to decrease around 0.3 units by 2100 (Bopp et al. 2013). This implies an increase in global acidity of around 150% (relative to

preindustrial levels) in a bit more than a century. Besides, surface seawater in the Arctic Ocean which is currently supersaturated with respect to carbonate minerals (i.e. $\Omega > 1$), is projected to become undersaturated ($\Omega < 1$) already by the end of the century under this high emissions scenario.

Rapid changes in biological influential environmental properties, such as surface temperatures, seawater pH and Ω, threat global biodiversity and ecosystem services (e.g., Williamson and Turley 2012). Some organisms present higher sensitivity to the pace of change rather than its magnitude. For instance, the coralline algae *Lithothamnion glaciale* suffer structural damages when exposed to a fast drop in pH. If the same pH fall occurs at a slower pace, their structure remains unharmed (Kamenos et al. 2013). It is unknown how biological systems will cope with the future environmental changes. Many uncertainties arise not only because of the high complexity involved and their resilience to perturbations, but also due to their adaptation potential to a changing environment. Yet, it has been estimated that in order to adapt to the projected rates of climate change in a high emissions scenario until 2100, most clades of major tetrapods (i.e. amphibians, birds, mammals and reptiles) would need rates of evolution that are 4 orders of magnitude higher than those generally surveyed among species (Quintero and Wiens 2013).

Changes in the future environmental conditions are not only expected over multi-decadal time scales, perturbations in seasonal variability are also projected. Disruptions in regional seasonality might induce further perturbations in biological systems, because life cycles and ecological interactions are often intertwined with the annual fluctuation in the environmental conditions (e.g., Ji et al. 2010; Pörtner et al. 2014). The impacts of a changing seasonal variability on marine biology are already being witnessed in the Arctic Ocean. Under-ice phytoplankton blooms under Arctic sea ice, develop in much colder water and earlier in the year because of multiyear old, thick ice being replaced by younger and thinner ice (Arrigo et al. 2012). The retreat of sea ice starts around 2 days earlier each year, leading to an altered pattern of organic matter production and consumption (Arrigo 2013). The growing season of ice algae shrinks whilst the open ocean phytoplankton blooms occur earlier and they

are more intense. A more productive Arctic Ocean does not directly imply benefits for the ecosystem functioning. Early blooms might reduce the available biomass required by higher trophic levels during their breeding season (Arrigo 2013). The early timing of phytoplankton blooms might increase the chances of survival of the larvae in certain fish species (Platt et al. 2003), leading to shifts in the ecosystem composition and disruptions in the Arctic Ocean food web structure (e.g., Sundby et al. 2016).

1.2 Deliberate Climate Intervention

Climate engineering (CE) is the technological intervention in the Earth's climate with the purpose of counteracting the effects of climate change (e.g., National Research Council 2015a,b; IPCC 2012). There are two major groups of CE methods: solar radiation management (SRM) and carbon dioxide removal (CDR) methods. SRM and CDR methods modulate surface temperatures by their effects on different atmospheric forcings. The former aims at decreasing the solar irradiance that reaches the Earth's surface whilst the latter deals with the root cause of the issue by reducing atmospheric CO_2 levels. CDR methods might also alleviate the effects of surface ocean acidification, either due to their impact on atmospheric CO_2 levels, or owing to direct effects on seawater carbonate chemistry. Commonly discussed CDR methods are, for instance, carbon capture and storage, reforestation, iron fertilization and artificial ocean alkalinization (AOA). Popular techniques of SRM are space mirrors, marine cloud brightening by artificial sea salt emissions and stratospheric sulfur injection. Among all these different CE techniques, SRM by injecting sulfur into the stratosphere and the ocean-based CDR method of AOA have been suggested to have large mitigation potential (e.g., National Research Council 2015a,b).

SRM via stratospheric sulfur injection involves the scattering of sulfur into the low stratosphere to form aerosol particles aiming at mimicking the effects of volcanic eruptions on surface temperatures (e.g., Crutzen 2006; Schmidt et al. 2012). These

particles would increase the portion of incoming shortwave radiation that is reflected back to space. Due to the reduction in the shortwave radiation reaching the Earth's surface, the net top-of-atmosphere (TOA) radiation would also decrease, leading to lower surface atmospheric temperatures.

This method could indirectly modify atmospheric CO_2 through an enhancement of the land and ocean sinks caused by the mitigated warming in surface atmospheric temperatures. Nevertheless, this reduction in atmospheric CO_2 would not lead to significant changes in the effects of ocean acidification (e.g., Keller et al. 2014; Tjiputra et al. 2016).

AOA is an ocean-based CDR method by which atmospheric carbon is chemically sequestered in seawater (Kheshgi 1995). AOA aims at accelerating the slow process of weathering that naturally occurs in timescales ranging between 10k-100k years (Hartmann et al. 2013). AOA consists in the enhancement of surface seawater total alkalinity (TA) by the spreading of processed alkaline compounds (e.g., calcium carbonate ($CaCO_3$), olivine (($Mg,Fe)_2SiO_4$)) or their dissociation products (e.g., calcium hydroxide ($Ca(OH)_2$), quicklime (CaO)). TA characterizes the charge balance of weak ions in seawater and its value is often dominated by the concentration of bicarbonate (HCO_3^-) and carbonate (CO_3^{2-}) ions (Zeebe and Wolf-Gladrow 2001). By increasing seawater TA at the ocean-atmosphere interface, the buffering capacity of seawater is modified to enhance the uptake and storage of carbon whilst seawater acidity decreases (Wolf-Gladrow et al. 2007).

1.3 Scope of This Study

The overall goal of this thesis is to examine the mitigation potential and associated side effects of large-scale AOA scenarios. For the first time, AOA model scenarios aiming at reducing atmospheric CO_2 concentrations to specific levels are designed. I implement and carry out large-scale AOA scenarios targeting CO_2 levels in a comprehensive Earth system model with interactive carbon cycle. Then I study the

impacts of these AOA scenarios on the global carbon uptake and ocean biogeo-chemistry. I further analyze the AOA-driven effects on the system by consistently comparing the impacts of the AOA scenarios to those of SRM simulations within the same modeling framework.

Different aspects of AOA have been already addressed in previous modeling stud-ies which were based either on ocean stand-alone configurations, or Earth system models of intermediate complexity. A preliminary analysis revealed that the pre-processing of rocks required for AOA is an energy- and carbon-intensive process (Kheshgi 1995). Based on an ocean stand-alone model, it has been estimated that the AOA scenario in which two moles of TA per mol of emitted CO_2 is distributed widely into the upper ocean, is the only one that stabilizes global surface seawater pH and Ω to current levels (Ilyina et al. 2013b). However, this large-scale AOA scenario may only reduce atmospheric CO_2 by 300 ppm by the end of this century. Besides, surface seawater Ω reaches levels in which the inorganic precipitation of $CaCO_3$ can be triggered, thereby reaching an upper biogeochemical threshold of this method. Another uncoupled model study on olivine-based AOA concluded that the concomitant addition of iron would exert a greater boost of marine primary pro-duction than the increase associated with the silicic acid enrichment (e.g., Köhler et al. 2013; Hauck et al. 2016). There is only one study that simulated this method with an Earth system model of intermediate complexity (Keller et al. 2014). Their AOA scenario showed a rather modest CDR mitigation potential because it was constrained by present-day transport capacity and only small amounts of TA were added into the surface ocean.

So far, AOA has not been examined with a state-of-the-art Earth System Model forced by fossil fuel CO_2 emissions. Using an Earth system model with this level of complexity, I include previously neglected interactions between the different ele-ments of the Earth system. I simulate an idealized AOA scenario within the 21st century, based on the RCP scenarios of climate change (van Vuuren et al. 2011). My modeling tool is the Max Planck Institute Earth System Model (MPI-ESM) in the configuration of the fifth phase Coupled Model Intercomparison Project (CMIP5)

(Giorgetta et al. 2013). I consider the high CO_2 emission scenario RCP8.5 to evaluate an upper limit response of the Earth system to a large-scale AOA scenario in which the growing atmospheric CO_2 concentrations of the RCP8.5 are reduced to RCP4.5 levels.

> How much does the buffering capacity of the ocean need to be enhanced in order to stabilize the atmospheric CO_2 to RCP4.5 levels in a high CO_2 emission scenario RCP8.5?

I only focus on the effects that AOA has on the Earth system regardless of potential socio-economical and technical limitations (e.g. finite mining and transport capacity, elevated energy demands). My modeling strategy carries several advantages. First, it provides a holistic perspective on the impacts of AOA on the global carbon cycle and the Earth's climate. Second, this approach allows to compare the different regional sensitivities to growing concentrations of TA in seawater. Thus, I explore these different aspects by addressing the following research question:

> What would be the consequences of a large-scale alkalinization scenario in the Earth system?

I extend my study of CE by including in the analysis a large-scale SRM scenario whose effects on the Earth system will be compared to those of the alkalinization scenario. Previous attempts at comparing different CE methods compare results between simulations that were calculated with different models and based on different scenarios (e.g., National Research Council 2015a,b; IPCC 2012). This approach complicates the comparison and it might even result in biased conclusions. Following this approach, the comparison between different CE methods includes not

only the differences between the methods, but also differences between the CE scenarios and models. The response of the Earth's system to CE is determined by the peculiarities of the assumed scenario, and model results will always depend on the parameterizations that describe the underlying processes. Differences in the response of the system to CE caused by the particular characteristics of the scenario are unavoidable. Yet, comparing different CE methods using the same model filters out discrepancies caused by differences in model parameterizations.

So far, only one study compares several CE methods using scenarios calculated using one model. Keller et al. (2014) studied the effectiveness and side effects of different CE methods (including AOA and SRM) with an Earth system model of intermediate complexity that did not include an interactive carbon cycle. I go beyond this study by exploring the impacts of AOA and SRM using the MPI-ESM with prognostic carbon cycle. My modeling approach includes a more realistic representation of atmospheric processes and the interaction between elements of the Earth system that were not previously considered. Both methods are simulated using the same model, which allows the consistent comparison of their effects and excludes differences due to model parameterizations. Finally, unlike previous studies, this modeling approach includes model internal variability which enables the comparison of the forced signal with internal variability.

In the AOA simulation, the target is atmospheric CO_2 whose concentrations are stabilized to RCP4.5 levels under RCP8.5 emissions, but SRM can only target radiation. This is why the intensity in the implementation of CE in the SRM scenario is defined by reducing the radiative forcing of the RCP8.5 scenario to RCP4.5 levels via stratospheric sulfur injection. I focus on the 21st century, and compare AOA and SRM scenarios in which the methods are either continuously applied until 2100 or terminated in 2070. Particularly, I would like to answer:

> What is the potential of large-scale AOA and SRM scenarios to exceed the rates of environmental change that they were intended to mitigate?

I pay special attention to regional patterns of surface temperatures because differences in the modified forcings by each of these schemes might lead to differential spatial patterns of warming (e.g., Govindasamy and Caldeira 2000; Schmidt et al. 2012). I also study the effects of these large-scale CE scenarios on the biogeochemical cycling of carbon in the ocean. Direct and indirect effects of AOA on seawater biogeochemistry differ strongly from those associated with SRM. They depend on the joint responses and synergies between the different elements of the Earth system. For that reason, the effects of these methods on the oceanic carbon cycle are not yet fully understood (e.g., Partanen et al. 2016; Tjiputra et al. 2016). In addition, I address the impacts of CE on seasonal variability of surface warming and seawater biogeochemistry. The comparative assessment that studied AOA and SRM using only one model (Keller et al. 2014) did not include the effects of CE in the seasonal cycle. Thus, I extend the comparison of these CE schemes by answering the following research question:

> How large-scale AOA and SRM scenarios affect the seasonal variability of biologically relevant ocean biogeochemical properties?

1.4 Thesis Outline

This thesis aims at studying the potential of AOA to mitigate the effects of climate change and the associated unintended consequences of AOA. I follow a novel modeling strategy by implementing large-scale AOA scenarios that target specific atmospheric CO_2 levels: I implement and carry out large-scale AOA scenarios targeting CO_2 levels in a comprehensive Earth system model with interactive carbon cycle. Chapter 2 of this thesis addresses the impacts on the climate system of a continuous large-scale AOA scenario until the end of the 21st century, with special focus on the ocean carbon cycle. This chapter has been published in *Geophysical Research Letters* (González and Ilyina 2016) (verbatim quote, but with references merged in the thesis bibliography). I further analyze the AOA-driven effects on the system by consistently comparing the impacts of the AOA scenarios to those of SRM simulations within the same modeling framework. Chapter 3 considers a comparison of different CE scenarios including: continuous large-scale AOA and SRM scenarios during this century until 2100 or terminated in 2070. The thesis ends in the chapter 4, in which the stated research questions in this introduction are answered and possible future steps are shortly described.

Chapter 2

Impacts of Artificial Ocean Alkalinization on the Carbon Cycle and Climate in Earth System Simulations

2.1 Introduction

Geoengineering techniques have been suggested to tackle climate change and ocean acidification; however, knowledge about their effectiveness and side effects remains sparse (e.g., The Royal Society 2009; National Research Council 2015a). Artificial ocean alkalinization (AOA) is one of the ocean-based carbon dioxide removal (CDR) methods that aims at enhancing the natural and slow (timescales of 10k-100k years) process of weathering by which CO_2 is taken out of the atmosphere via chemical sequestration (e.g., Kheshgi 1995; Hartmann et al. 2013). Total alkalinity (TA) describes the charge balance of weak ions in seawater (Wolf-Gladrow et al. 2007), and the method of ocean alkalinization involves the release of processed alkaline minerals (e.g. olivine, calcium carbonate), or their dissociation products (e.g. quicklime,

calcium hydroxide) at the ocean-atmosphere interface. By increasing surface TA, CO_2 uptake and storage is enhanced and, the buffering capacity of seawater is modified such that seawater pH increases. The amount of added alkalinity varies depending upon the used chemical substance.

Previous modelling studies have addressed some aspects of AOA. For instance, Ilyina et al. (2013b) based on an ocean stand-alone model configuration, showed that addition of large amounts of alkalinity might elevate Ω to values at which inorganic fallout of $CaCO_3$ starts, thereby reaching a natural biogeochemical threshold of AOA. A study with an Earth system model of intermediate complexity (Keller et al. 2014), constrained by present-day transport capacity and thus adding small amounts of alkalinity, suggested a low potential of AOA to mitigate atmospheric CO_2 rise. Köhler et al. (2013), studying olivine-based alkalinity enhancement projected changes in the marine biology and biological carbon pumps due to the silicic acid enrichment associated with AOA using olivine. The greatest impact on marine biology of AOA via olivine dissolution, however, was shown to be due to the concomitant iron enrichment (Hauck et al. 2016).

While the effects of AOA on marine biota are not yet fully understood, a laboratory study reveals that addition of alkalinity could disrupt the acid-base balance of marine organisms such as littoral crabs (Cripps et al. 2013). Besides, the addition of alkaline substances releases conjointly toxic heavy metals (e.g. cadmium, nickel, chromium) leading to further perturbations that would likely impact ocean biogeochemical cycling and marine ecosystem services (e.g., Hartmann et al. 2013; Hauck et al. 2016).

We explore an idealized alkalinity enhancement scenario focusing on the current century based on the representative concentration pathways (RCP) scenarios of climate change. We use the Max Planck Institute Earth System Model (MPI-ESM) in the configuration of the fifth phase Coupled Model Intercomparison Project (CMIP5) (Giorgetta et al. 2013) forced by fossil fuel CO_2 emissions. By testing the high CO_2 emission scenario RCP8.5, we address the question whether in a high CO_2 world fol-

lowing the RCP8.5 scenario, it is possible to stabilize atmospheric CO_2 to RCP4.5 levels by AOA alone. If so, how much does the buffering capacity of the ocean need to be enhanced? What will be the consequences of such a large-scale AOA scenario in the Earth system? We also address the response of the different ocean basins to AOA, revealing the different regional sensitivities to increasing seawater TA. Despite of the inherent limitations of AOA (e.g. finite shipping capacity, high energy demands, etc), we solely focus on the response of the Earth system to this geoengineering method.

2.2 Methodology

2.2.1 Model Description

In the ocean biogeochemical model HAMOCC which is part of MPI-ESM, seawater TA varies due to $CaCO_3$ formation and dissolution, CO_2 fixation and respiration by biota, changes in freshwater and weathering fluxes as well as seawater-sediment interaction. Natural weathering fluxes of $CaCO_3$ and silicate are prescribed so that they compensate the losses of these materials to the sediments (Ilyina et al. 2013a). The globally uniform input of $CaCO_3$ does not vary over time and increases the TA content by 56.84 TmolC/yr in all the scenarios described in this study. Dissolved inorganic carbon (DIC) is not only altered due to these natural processes that vary TA, but also due to atmosphere-ocean gas exchange. Variations in the DIC to TA ratio determine hydrogen ion concentrations and therefore seawater pH. HAMOCC is embedded into the free-surface ocean circulation model (MPIOM) including a sea ice component; both modules have a nominal resolution of $1.5°$ and 40 unevenly spaced vertical levels (Jungclaus et al. 2013). Terrestrial biogeochemistry and land-atmosphere interaction are simulated with the land vegetation model JSBACH (Reick et al. 2013), which is directly coupled to the atmospheric general circulation model (ECHAM6) (Stevens et al. 2013) and runs on the same horizontal grid ($1.9°$ horizontal grid resolution and 47 pressure levels). This is the low resolu-

tion version of the emissions-driven MPI-ESM as used in CMIP5 (Giorgetta et al. 2013).

2.2.2 Alkalinization Scenario

Alkalinity enhancement is designed to stabilize the increasing atmospheric CO_2 concentration of the RCP8.5 to RCP4.5 levels (Figure 2.1d). The cumulative carbon emissions of the RCP8.5 scenario ($\sim$1850 GtC) are higher than those of the RCP4.5 by around 940 GtC by the year 2100 (Figure 2.2). The RCPs reference simulations are calculated with the MPI-ESM and their description can be found in van Vuuren et al. (2011). RCP4.5 takes into account mitigation efforts and therefore different (than RCP8.5) land management, air pollutants and greenhouse gases emissions are assumed. Land-use transitions and emissions of air pollutants and greenhouse gases (such as CO_4, N_2O and CFCs) in the alkalinization scenario are given by the RCP8.5 scenario. Alkalinity is added every time step increasingly over time and spatially homogeneous (same amount per unit area) into the first ocean model level including oceanic areas covered by sea ice (i.e. first 12 meters modified by the surface elevation). DIC, nutrients or trace metals are not added during the alkalinization scenarios. The simulation starts in 2006 and AOA begins when atmospheric CO_2 differs from the one of the RCP4.5 scenario by around 1% (year 2018). AOA lasts until 2100 when also the simulation period ends. Model internal variability is addressed with an ensemble of three members. The forcing in each run is identical but they were initialized from the end of different ensemble members of historical CMIP5 experiments (Giorgetta et al. 2013).
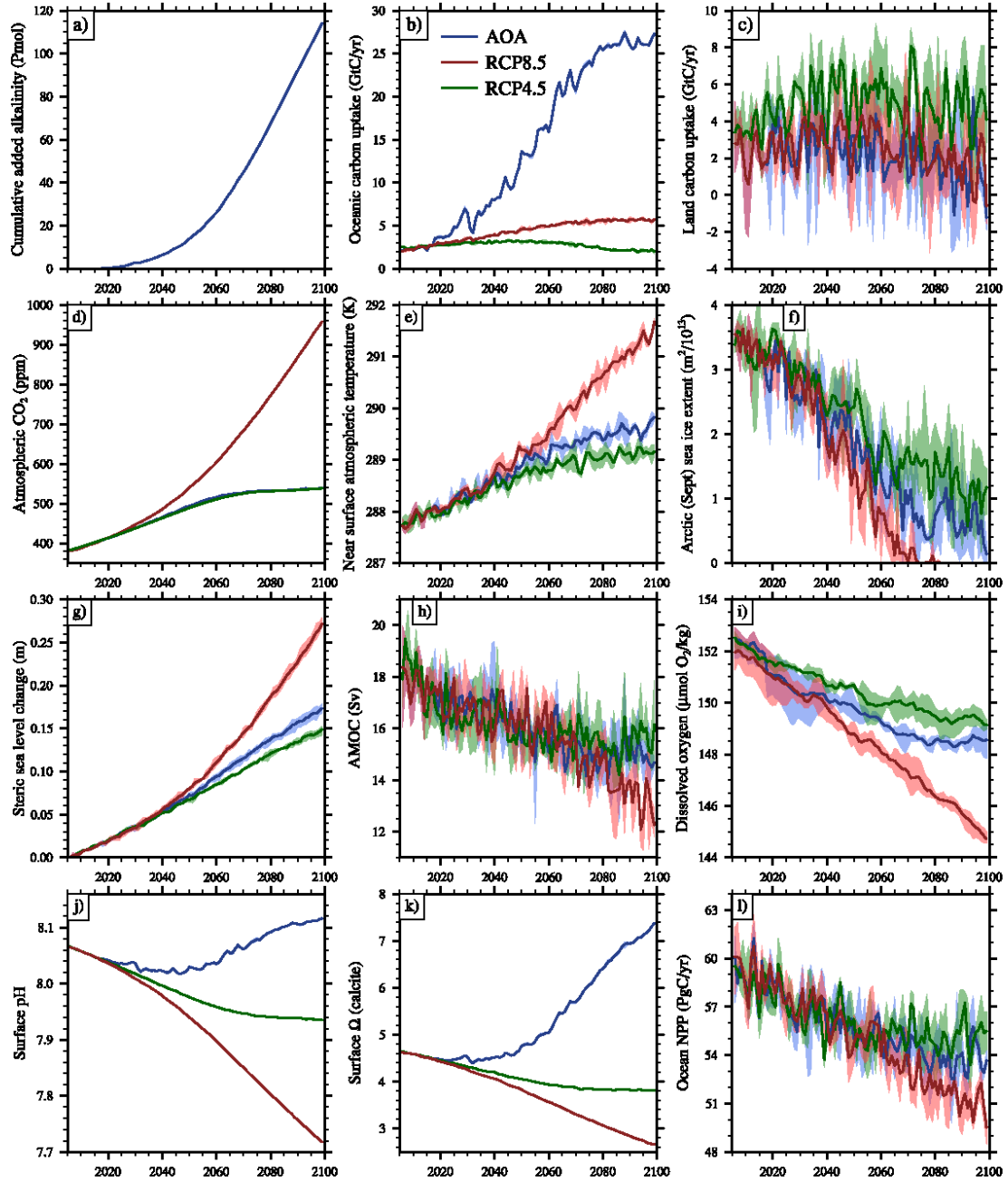
Figure 2.1: (Continued on the following page.)

Figure 2.1: Temporal evolutions of various Earth system variables in different scenarios. Solid lines depict 3 year running means under the scenarios RCP8.5 (red), AOA (blue) and RCP4.5 (green). (a) Cumulative added alkalinity (Pmol), (b) total ocean carbon uptake per year (Gt/yr), (c) total terrestrial carbon uptake per year (Gt/yr), (d) global annual mean of atmospheric CO_2 (ppm), (e) global annual mean of near-surface atmospheric temperature (K), (f) monthly mean (September) of Arctic sea ice extent (m^2), (g) global annual mean of steric sea level rise (m), (h) Atlantic meridional overturning circulation zonally averaged at 26° N (Sv; sverdrup (10^6 m^3/s)), (i) global annual mean of O_2 concentration vertically averaged over 200-600 m ($\mu mol O_2$/kg), (j) global annual mean of surface seawater pH, (k) global annual mean of surface Ω with respect to calcite, (l) global annual mean of ocean net primary production (NPP) vertically integrated (PgC/yr). Colored area is model internal variability including three ensemble members.
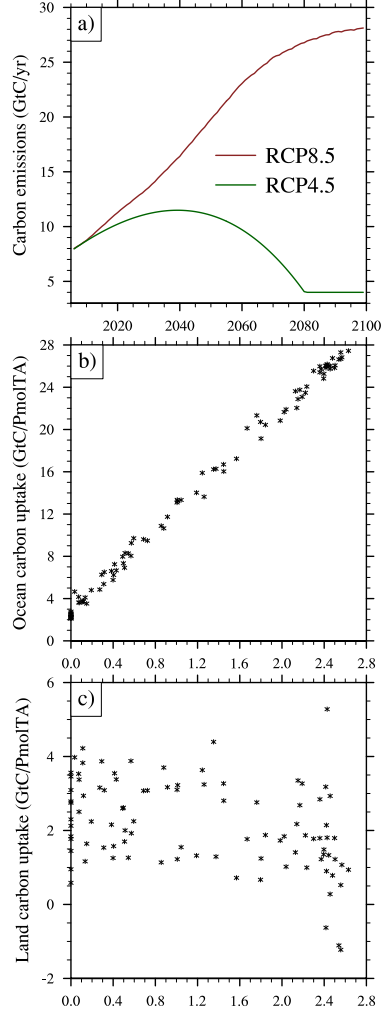
Figure 2.2: (a) CO_2 emission rates (GtC/yr) of the representative concentration pathways RCP8.5 (red) and RCP4.5 (green) scenarios. (b) Globally integrated oceanic carbon uptake as a function of the added total alkalinity (GtC/PmolTA) in the alkalinization scenario. (c) Globally integrated terrestrial carbon uptake as a function of the added total alkalinity (GtC/PmolTA) in the alkalinization scenario.

2.3 Fate of Added Alkalinity

In order to maintain atmospheric CO_2 at RCP4.5 levels under the high emission scenario RCP8.5, approx. $114 \cdot 10^{15}$ mol (Pmol) of added alkalinity would be needed until the year 2100 in total (Figure 2.1a). This implies an increase in the globally averaged surface TA concentration of around 30%. In order to produce 114 Pmol of TA, about $4.01 \cdot 10^{12}$ metric tons (Tt) of olivine would be needed, which would require an increase of 3 orders of magnitude in the total olivine production until 2100. The total production of lime until 2100 would need to be enhanced by 2 orders of magnitude to supply around 4.22 Tt of lime which are required to produce 114 Pmol of TA (details of these estimations can be found in section 2.8).

The amount of needed alkalinity increases over time due to the growing atmospheric CO_2 concentrations of the RCP8.5 scenario (up to 950 ppm in 2100 (Figure 2.1d)). The fate of added alkalinity is different in each ocean basin due to its dissimilar current dynamics (Figure 2.7). Surface TA in the Atlantic, Pacific and the Indian Ocean basins, increments by ~0.05% (relative to their present-day value) in 2045. Then, surface TA further increases over time so that at the end of this century in both the south Atlantic and the entire Pacific, present-day TA is exceeded by ~35% (i.e. from an initial value of ~2.300 µmol/kg to ~3.100 µmol/kg in a time-lapse of 55 years). Even higher values are reached in the north Atlantic and Indian Oceans (up to 50% higher than present-day levels). Alkalinity is only added in the first 12 meters of the ocean (± surface elevation) and then it is mixed with deeper water masses through the processes of advection and diffusion. This vertical mixing leads to TA changes in these basins reaching water masses within the first 1000 meters of the water column during the last decades of this century. The Arctic and Southern Ocean present a different temporal and spatial evolution compared to other ocean basins and between each other. This is due to the volume of water involved in the dissolution of the added alkalinity which is, comparing all the basins, much lower in the Arctic and much higher in the Southern ocean, leading to a different increment of TA per unit volume in these two basins.

2.4 Impact on Carbon Uptake and Storage

In the modern ocean, tropical and subtropical regions act as sources of carbon to the atmosphere (Takahashi et al. 2009). The MPI-ESM projects some of these regions to change from source to sink of carbon at the end of this century under the RCP8.5 high emission scenario (Figure 2.3). In the alkalinization experiment, all regions of the ocean absorb atmospheric carbon due to the changes in the buffering capacity. The equator presents the lowest carbon uptake ($\sim$20 gC/m^2) while areas within latitudes from 30 to 80 degrees show the highest values ($\sim$100 gC/m^2). The globally integrated uptake of carbon by the ocean responds linearly to the addition of TA (Figure 2.2b), with much lower variability compared to the globally integrated carbon uptake by land (Figure 2.2c).

The enhanced oceanic CO_2 uptake (Figure 2.1b) in the AOA scenario greatly increases the marine DIC pool (Figure 2.4). Compared to the RCP8.5, the vertically integrated increase in DIC content by 2100 is up to one order of magnitude higher in some regions, as for instance the high-latitudes of the North Atlantic Ocean (i.e. increasing from around 2-5 kgC/m^2 in RCP8.5 and up to 10-15 kgC/m^2 in the AOA scenario). Because of the great volume of seawater involved in the transport of carbon in the Southern Ocean, the DIC increment per unit volume is much smaller compared to the other basins (Figure 2.8). Changes in carbon uptake and storage over land in the AOA scenario are similar to those associated with the RCP8.5 scenario (Figures 2.1c and 2.4). However, carbon storage over land is slightly lower in the AOA scenario compared to the RCP8.5 due to the decrease in atmospheric CO_2 concentration that lowers the CO_2 fertilization effect on the terrestrial biosphere. Variations in land carbon uptake and storage in our AOA scenario relative to RCP4.5 are due to anthropogenic land use, CO_2 fertilization (Schneck et al. 2013) and regional changes in temperature and precipitation (Giorgetta et al. 2013; Reick et al. 2013).
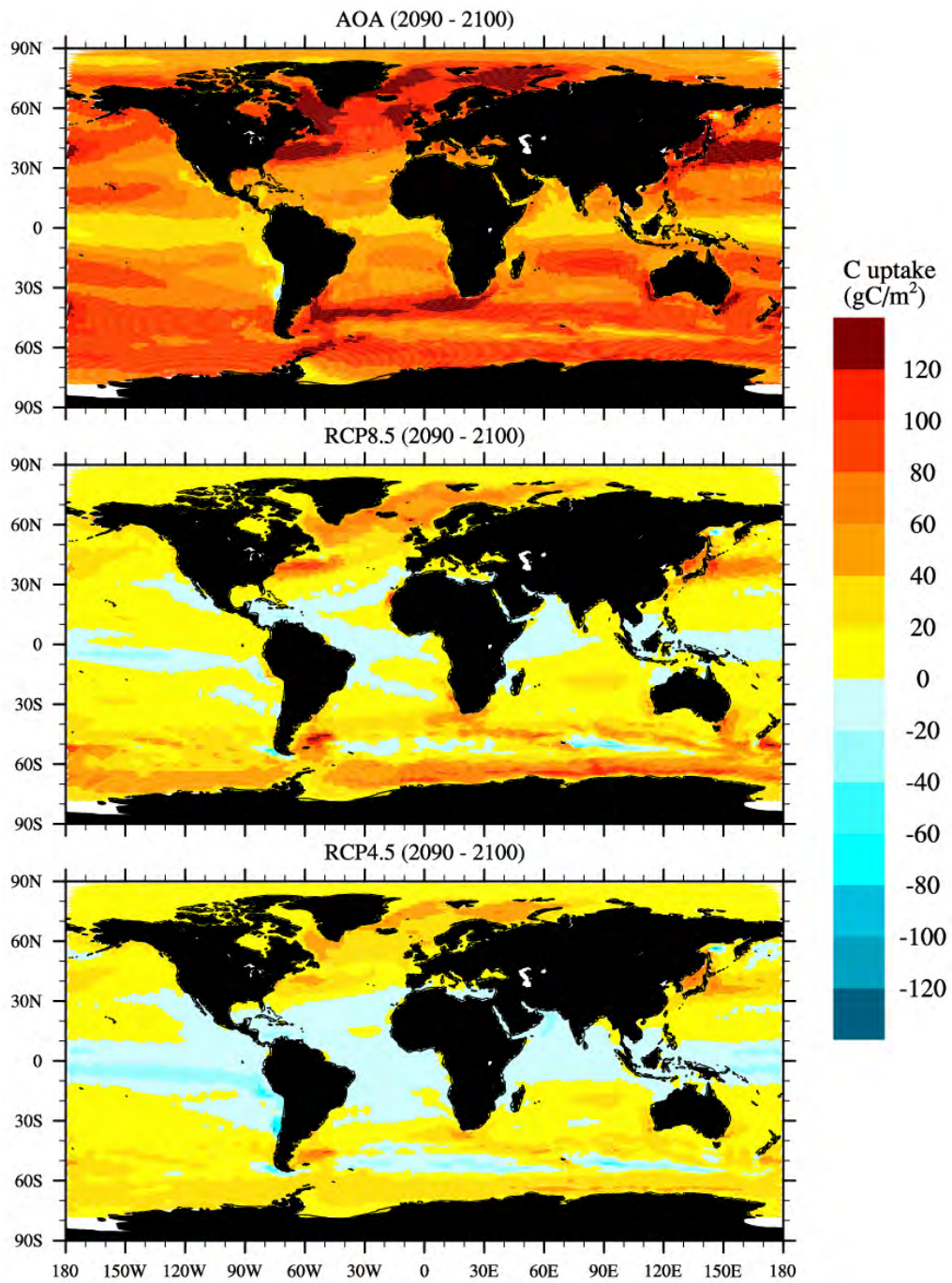
Figure 2.3: Cumulative annual marine carbon uptake (gC/m^2) averaged over the period between 2090 and 2100 for the experiments: AOA (top), RCP8.5 (middle) and RCP4.5 (bottom).
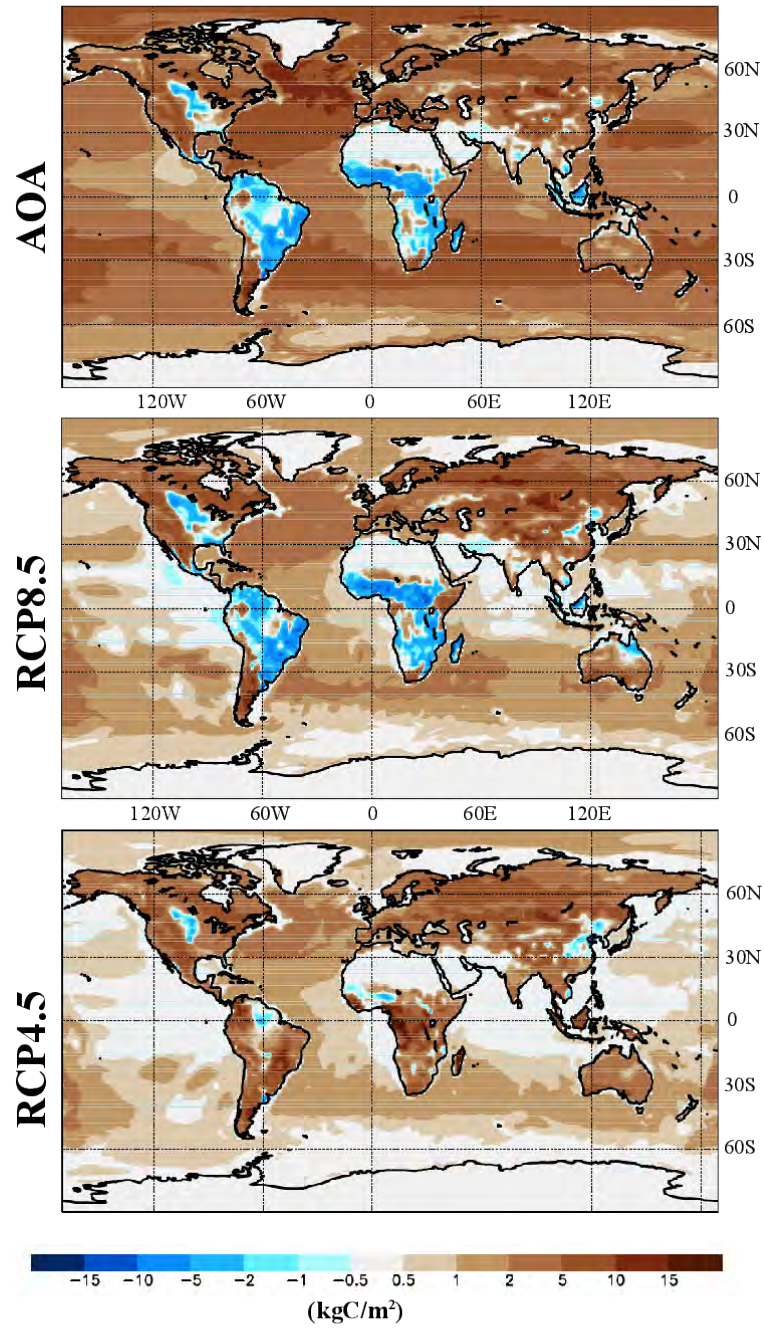
Figure 2.4: Changes in the terrestrial and oceanic carbon budgets: difference between the annual mean carbon reservoirs (vertically integrated) of the year 2100 and the year 2006 in the scenarios (top) AOA, (middle) RCP8.5, and (bottom) RCP4.5 (bottom). Note the nonlinear color bar.

2.5 Effects on the Climate System

The alkalinization scenario leads to a large oceanic carbon uptake enhancement (up to 27 GtC/yr at the end of this century) (Figure 2.1b) and therefore, much lower atmospheric CO_2 concentrations and surface atmospheric temperatures (Figures 2.1d and 2.1e). Compared to the reference scenario RCP8.5, the AOA experiment leads to a reduction in the annual global mean of air surface temperature of around 1.5 K, following more closely the RCP4.5 scenario. The slightly higher temperature (0.5 K) of AOA compared to RCP4.5 is because AOA only reduces atmospheric CO_2 so that the other GHGs remain unmitigated. Not only GHGs emissions differ between RCP8.5 and RCP4.5, land-use and pollutant emissions are also specifically defined for each scenario. Because of that, differences in the state of the climate between the targeted (solely in terms of atmospheric CO_2 levels) RCP4.5 and the strongly mitigated RCP8.5 by means of the AOA scenario are expectable.

Boreal summer sea ice extent is projected to shrink as global temperature rises during the 21st century (IPCC 2013; Notz et al. 2013). While the summer sea ice is projected to disappear under the RCP8.5 scenario around the year 2070 (Figure 2.1f), this does not occur under the AOA scenario, even so a reduction to $\sim$15% of its current value (i.e., to $\sim$5$\cdot$10^{12} m^2) is obtained because of the higher temperatures relative to the current climate state. Such slightly higher temperatures are also the reason why this geoengineering scenario only reduces $\sim$75% of the projected steric (due to thermal expansion) sea level rise in the RCP8.5, differing from the targeted RCP4.5 by $\sim$0.03 meters (Figure 2.1g). The Atlantic Meridional Overturning Circulation (AMOC) has been projected to weaken under the RCP8.5 scenario (IPCC 2013). This weakening is reduced under the AOA scenario leading to a similar value than the one projected under the RCP4.5 scenario (Figure 2.1h).

The above-mentioned set of variables present different ranges of internal model variability. For instance, the internal model variability of oceanic carbon uptake and atmospheric CO_2 levels is small and is driven by the trajectory prescribed by the

emissions scenarios. In contrast, variability associated with parameters such as the Arctic summer sea ice, terrestrial carbon uptake and the AMOC is much larger (up to one order of magnitude lower than the values of these parameters). In spite of the large internal model variability in some of the variables, the AOA signal is clear and trends are consistent among different ensemble members.

Regarding regional differences in near-surface atmospheric temperatures (Figure 2.5), the higher effect is found in the Arctic due to the Arctic amplification and over the continents due to the different heat capacity of land and ocean surfaces. Compared with the unmitigated RCP8.5, the large-scale AOA scenario prevents $\sim$2.8 K of warming over the Arctic and the sub-polar regions of the North hemisphere.
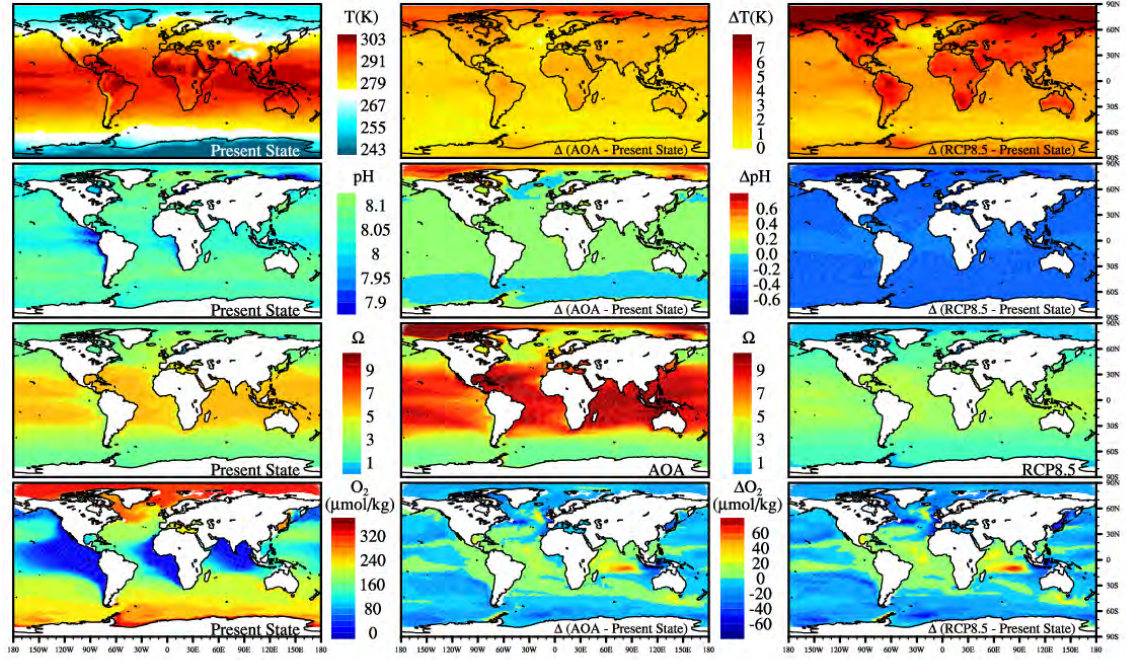
Figure 2.5: Annual means (averaged over 10 years period) and anomalies of near-surface atmospheric temperature (first row), surface seawater pH (second row), surface seawater Ω (third row) with respect to calcite and O_2 concentration vertically averaged over intermediate waters (200-600 m water depth, fourth row). (left column) Present-day state (2006-2015); Differences between the AOA (2090-2099, middle column) and the RCP8.5 (2090-2099, right column) scenarios and present-day state except for the 3rd row where only absolute values of Ω are depicted. Color-bars for the maps in the left column are to their right side. Maps in the middle and right columns share the color bars located between them.

2.6 Effects on Ocean Biogeochemistry

The AOA scenario strongly mitigates ocean acidification over the whole period of integration, albeit leading to much higher global surface ocean pH and Ω (calcite) values than those of the RCP4.5 scenario (Figures 2.1j and 2.1k). In the last decades of this century, higher than present-day values of surface ocean pH are reached. Regarding Ω, higher than modern ocean levels are achieved from 2050 until the end of the simulated period.

Considering regional surface seawater values (Figure 2.5), under the RCP8.5 scenario pH and Ω decline so that, for instance, most of the Arctic Ocean becomes undersaturated by the end of the century in our model. AOA mitigates ocean acidification effects, but modern ocean pH and Ω values are strongly exceeded in several regions which is an unintended consequence of this method that may induce negative effects on marine biota (e.g., Cripps et al. 2013; Haigh et al. 2015). As a result of our idealized implementation scheme, in large regions of the Arctic Ocean, surface seawater pH greatly exceeds current levels. Besides, much higher levels of supersaturation are also reached in the Arctic surface seawater regionally (five times larger than modern ocean levels) and in most of the tropical and subtropical oceans (doubling present-day values). Hence, a large-scale AOA scenario, along with perturbations in the biogeochemical cycles due to warming (e.g., Vancoppenolle et al. 2013; Steiner et al. 2014), is likely to cause strong unintended side effects in these ocean basins. Still, values higher than 20 (best current estimate but not well constrained), when inorganic sinking of $CaCO_3$ is estimated to be triggered (Morse and He 1993), are not obtained in the open ocean.

Within this century, the MPI-ESM under the RCP8.5 scenario projects the most pronounced decrease in global mean pH and Ω within approx. the upper 500 meters of the water column (Figures 2.6, 2.11 and 2.13). This is consistent with CMIP5 models (e.g., Bopp et al. 2013; Gehlen et al. 2014). In tropical oceans where warm-water corals grow, Ω values largely drop. These changes in seawater pH and Ω do
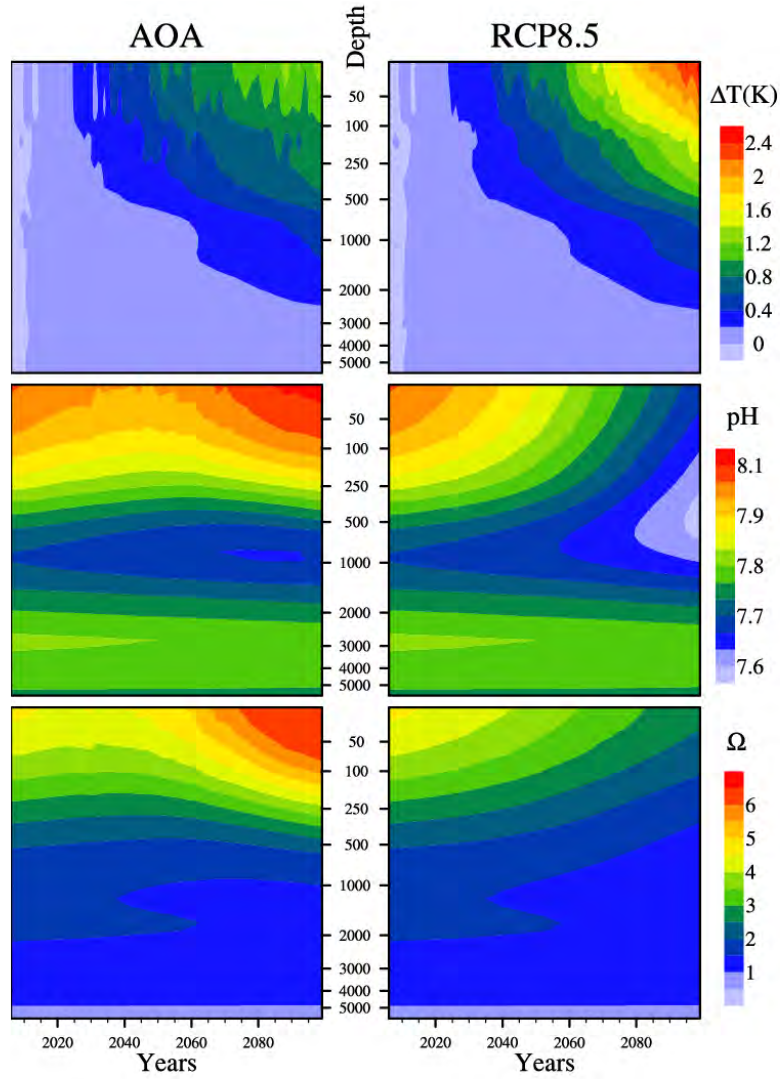
Figure 2.6: Temporal evolution of the vertical profiles (globally averaged annual means) of seawater potential temperature anomaly with respect to present-day ocean state (2006-2015), absolute values of seawater pH and Ω with respect to calcite under the experiments (left column) AOA and (right column) RCP8.5. Note the nonlinear vertical axis in which resolution decreases with depth.

not occur under the AOA scenario (Figures 2.6, 2.10 and 2.12). Between approx. 250 and 1000 meters depth, pH and Ω are restored to levels of the modern ocean during the last decades of this century. However, as a side effect in most of the ocean basins, modern levels are exceeded in shallower than 250 meters depth. At deeper levels than 1000 meters under the AOA scenario, the propagation of ocean acidification continues. Over time scales of several centuries, the ocean acidification signal would reach the bottom ocean and trigger reaction with carbonate sediments (Ilyina and Zeebe 2012). Thus, in the course of the 21st century, large-scale AOA can only partially prevent the projected deep ocean acidification (Gehlen et al. 2014). These are general features present in most of the ocean basins. Still, the response of each basin under the strong AOA mitigation shows differences; indicating different seawater pH and Ω sensitivities owing to their particular physical and biogeochemical states. In the Southern Ocean, seawater pH and Ω remain similar to present-day values over the whole period of integration under the AOA scenario because of its fairly constant DIC to TA ratio over time (Figure 2.9). The Indian, Atlantic, Pacific and Arctic Oceans show different sensitivities to the homogeneous alkalinization, with the Indian basin reaching the highest Ω levels in upper 250 meter. The response to AOA of the carbonate system in this study is consistent with results of previous studies where different model setups have been used under different AOA scenarios (e.g., Köhler et al. 2013; Ilyina et al. 2013b; Keller et al. 2014). The obtained high values of pH and Ω are driven by the large-scale alkalinization assumed with large amounts of alkalinity being added in our experimental design. Compared to the current ocean state, the higher Ω values at deeper ocean layers under the AOA scenario for all the ocean basins during the last decades of this century (Figure 2.12), imply a deepening of the calcite saturation horizon (Ω=1) and lower $CaCO_3$ dissolution rates at these depths. The opposite effect occurs under the RCP8.5 scenario. Ocean acidification lowers Ω within the water column (Figure 2.13), increasing the $CaCO_3$ dissolution rates at these depths and shallowing the calcite saturation horizon.

Changes in the ocean thermal state indirectly driven by AOA (via atmospheric

CO_2 reduction) penetrate until similar depths as the pH and Ω signals (Figure 2.6). Besides, these changes in the thermal state show a much more homogeneous vertical profile, not only compared to the above discussed biogeochemical variables but also compared to the thermal state anomaly under the RCP8.5 scenario. This is due to the lower rate of warming over time and the concomitant lower thermal stratification in the AOA scenario relative to the RCP8.5.

Ocean biogeochemistry is not only directly affected by AOA, it is also indirectly altered through changes in the climate state brought about by alkalinity enhancement. For instance, marine net primary production is projected to decrease over time under the high emission scenario RCP8.5 (Figure 2.1l). This is due to higher nutrient limitation driven by an enhancement in ocean thermal stratification (Bopp et al. 2013). The mitigated ocean warming under the AOA scenario decreases such an enhanced stratification. Besides, in case of using olivine, net primary production might be further boosted in the AOA scenario due to the addition of iron and silicic acid (e.g., Hauck et al. 2016; Köhler et al. 2013). The projected decline in oxygen at mid-depths (within the upper 200-600 meters) is also indirectly mitigated by the AOA scenario. Temporal evolution of oxygen at mid-depths (global annual means) paralelly follows the RCP4.5 projection hampering the steep decline under the RCP8.5 scenario (Figure 2.1i). Regionally, changes in oxygen indirectly driven by AOA follow the same spatial patterns projected in the RCP8.5, however the magnitude of change is reduced (Figure 2.5). Internal model variability, is much lower in pH and Ω values and higher for ocean net primary production and oxygen concentrations. This is confirmed in previous modelling studies, suggesting high (but likely underestimated in ESMs) internal variability of oxygen concentration variations (e.g., Andrews et al. 2013). However, temporal trends are consistent and it is clear that state of the system is close to the one of the RCP4.5 scenario.

2.7 Summary and Conclusions

We focus on the consequences of a large-scale AOA scenario in the Earth system in which atmospheric CO_2 concentrations of the RCP8.5 scenario are reduced to RCP4.5 levels until the year 2100 after addition of ca. 114 Pmol of alkalinity. This large amount of added alkalinity determines the response of the Earth system. The entire ocean turns into a carbon sink removing 940 GtC from the atmosphere. The global warming of the RCP8.5 world is mitigated by about 1.5 K at the end of this century. The 0.5 K higher global surface atmospheric temperature of the AOA scenario compared to the targeted RCP4.5 is due to the radiative forcing effect of non-CO_2 GHGs. Precipitation, Arctic sea ice extent, and steric sea level rise adjust to the slightly warmer (than RCP4.5) climate state with the extreme sea level rise and ice loss being prevented. Biogeochemical parameters such as oxygen and net primary production behave in accordance to the changes in the climate system, albeit indicating large internal variability.

The enhanced ocean carbon uptake and storage nearly doubles the marine DIC content increase projected under the RCP8.5 scenario by 2100. This invasion of CO_2 into the ocean would lead to stronger acidification than the one projected under the RCP8.5 and RCP4.5 scenarios. Yet, the alkalinization fully compensates the decreasing seawater pH with the side effect of surface pH and Ω values exceeding levels of the modern ocean. Given the length of our simulation, AOA only partially addresses effects of climate change and ocean acidification in the deep ocean.

Our AOA scenario reveals the different regional sensitivities to increasing seawater TA. Alkalinity addition is spatially homogeneous. Still, pronounced regional differences arise on the pH and Ω response to AOA due to the varying physical regimes and biogeochemical states of the different ocean basins. In our alkalinization scenario, the Arctic Ocean is a hot spot for unintended changes brought about by a large-scale AOA. This is because a dissimilar rise of DIC and TA under the AOA scenario, increases surface seawater pH (up to 0.6 higher units) and Ω (fivefold

increase) to greater than modern ocean levels. In the tropical oceans, surface Ω doubles present-day values due to synergies between growing seawater temperatures and increasing carbonate concentrations. Thus, the strong CO_2 removal potential of AOA implicates an unprecedented ocean biogeochemistry perturbation. The consequences of these regional perturbations in the seawater chemical environment are completely unknown, but they may be negative, not only due to the magnitude of the changes but also owing to their pace.

2.8 Details of Lime and Olivine Estimations

- **Lime** (calcium hydroxide, $Ca(OH)_2$) dissolution in water follows the following reaction:

$$Ca(OH)_2 + 2\,CO_2 \longrightarrow Ca_2^+ + 2\,HCO_3^-$$
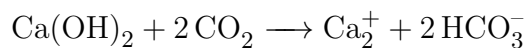
Dissolution of lime leads to an increase in TA of 2 mol per mol of dissolved lime (theoretical upper limit).

Lime molar mass (g/mol) = Ca + 2·O + 2·H = 40.08 + 2·16.00 + 2·1.01

= 74.1 g/mol $\Rightarrow$ 1 mol of $Ca(OH)_2$ weighs 74.1 grams

AOA scenario requires (in total until 2100) 114 Pmol of TA = $114 \cdot 10^{15}$ mol TA.

1 mol $Ca(OH)_2$ increases TA by 2 moles $\Rightarrow$ to obtain $114 \cdot 10^{15}$ mol of TA

$(1/2) \cdot 114 \cdot 10^{15}$ mol $Ca(OH)_2$ are needed

$57 \cdot 10^{15}$ mol $Ca(OH)_2$ = $74.1 \cdot 57 \cdot 10^{15}$ grams of $Ca(OH)_2$

= $4,224 \cdot 10^{18}$ grams of $Ca(OH)_2$

$4,224 \cdot 10^{18}$ grams of $Ca(OH)_2$ = $4,224 \cdot 10^{12} \cdot 10^6$ grams of $Ca(OH)_2$

= $4,224 \cdot 10^{12}$ metric ton (t) of $Ca(OH)_2$ (= needed in total until 2100 in the AOA scenario)

Comparison with current estimates of lime production:

Estimated world lime production during 2015 was 350000 thousand metric tons (The United States Geological Survey 2016).

350000 thousand metric tons of lime = $350 \cdot 10^6$ t of lime = 350 Mt of lime.

Assuming constant global lime production until 2100:

84 years $\cdot$ $350 \cdot 10^6$ t of lime per year = $29400 \cdot 10^6$ t of lime (= assumed to be produced in total until 2100)

Comparing the needed amount of TA until 2100 in the AOA scenario with this lime production estimate:

Total TA needed in AOA scenario / assumed total TA produced using lime

= $4.224 \cdot 10^{12}$ (t of lime) / $29400 \cdot 10^6$ (t of lime) = $1.44 \cdot 10^2$

The total production of lime until the end of the century would need to be increased by 2 orders of magnitude to obtain the required TA in the AOA scenario using lime as TA source. This number represents a theoretical minimum. Namely, it is the lowest amount required to obtain the 114 Pmol of TA using lime because it is based on the theoretical maximum of the dissolution reaction (i.e. each mol of lime is "fully available" and exactly 2 moles of TA are obtained out of this mol of lime). Real conditions would increase (never decrease) the amount of lime needed to obtain the 114 Pmol of TA. Some of the effects that would increase (because they decrease the efficiency of the reaction) the amount of needed lime associated with the required 114 Pmol of TA are:

1) the incomplete dissolution of lime due to the limiting effect of the surface of the lime grains that is in contact with the water and therefore is available for the reaction,

2) the aggregation of lime grains into larger particles diminishing the available surface for reaction,

3) the sinking of the added lime into ocean depths at which the change in TA would not lead to the simulated impact on the carbon cycle.

Besides, this estimation of the required lime production enhancement does not account for the demand for lime by different industrial sectors, which would further increase the required lime production until 2100.

- **Olivine** (Mg_2SiO_4) dissolution in water follows the following reaction:

$$Mg_2SiO_4 + 4\,CO_2 + 4\,H_2O \longrightarrow 2\,Mg_2^+ + 4\,HCO_3^- + H_4SiO_4$$
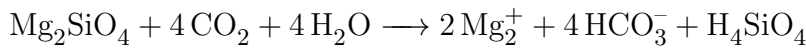
Dissolution of olivine leads to an increase in TA of 4 mol per mol of dissolved olivine (theoretical upper limit).

Olivine molar mass (g/mol) = 2·Mg + Si + 4·O = 2·24.30 + 28.09 + 4·16.00

= 140.69 g/mol $\Rightarrow$ 1 mol de olivine weighs 140.69 grams

AOA scenario requires (in total until 2100) 114 Pmol of TA = $114 \cdot 10^{15}$ mol TA.

1 mol Mg_2SiO_4 increases TA by 4 moles $\Rightarrow$ to obtain $114 \cdot 10^{15}$ mol of TA

$(1/4) \cdot 114 \cdot 10^{15}$ mol Mg_2SiO_4 are needed

$28.5 \cdot 10^{15}$ mol Mg_2SiO_4 = $140.69 \cdot 28.5 \cdot 10^{15}$ grams of Mg_2SiO_4

= $4.01 \cdot 10^{18}$ grams of Mg_2SiO_4

$4.01 \cdot 10^{18}$ grams of Mg_2SiO_4 = $4.01 \cdot 10^{12} \cdot 10^6$ grams of Mg_2SiO_4 = $4.01 \cdot 10^{12}$ metric ton (t) of Mg_2SiO_4 (= needed in total until 2100 in the AOA scenario)

Comparison with current estimates of olivine production:

The current total global production of olivine is about 8 Mt per year (= $8 \cdot 10^6$ t/yr of Mg_2SiO_4) (Hartmann et al. 2013).

Assuming constant global olivine production until 2100:

84 years · $8 \cdot 10^6$ t of olivine per year = $672 \cdot 10^6$ t of olivine (= assumed to be

produced in total until 2100)

Comparing the needed amount of TA until 2100 in the AOA scenario with this olivine production estimate:

Total TA needed in AOA scenario / assumed total TA produced using olivine

$$= 4.01 \cdot 10^{12} \text{ (t of olivine) } / \ 672 \cdot 10^{6} \text{ (t of olivine) } = 6 \cdot 10^{3}$$

The total production of olivine until the end of the century would need to be increased by 3 orders of magnitude to obtain the required TA in the AOA scenario using olivine as TA source. As in the case of the previously estimated lime production increase, this number represents a theoretical minimum. That is, it is the lowest amount required to obtain the 114 Pmol of TA using olivine as TA source because it is based on the theoretical maximum of the dissolution reaction (i.e. each olivine mol is "fully available" and exactly 4 moles of TA are obtained out of this mol of olivine). Real conditions would increase (never decrease) the amount of olivine needed to obtain the 114 Pmol of TA. The same effects that would increase the amount of needed lime would affect an AOA scenario using olivine (i.e. incomplete dissolution, aggregation, sinking and demand of olivine by different industrial sectors).
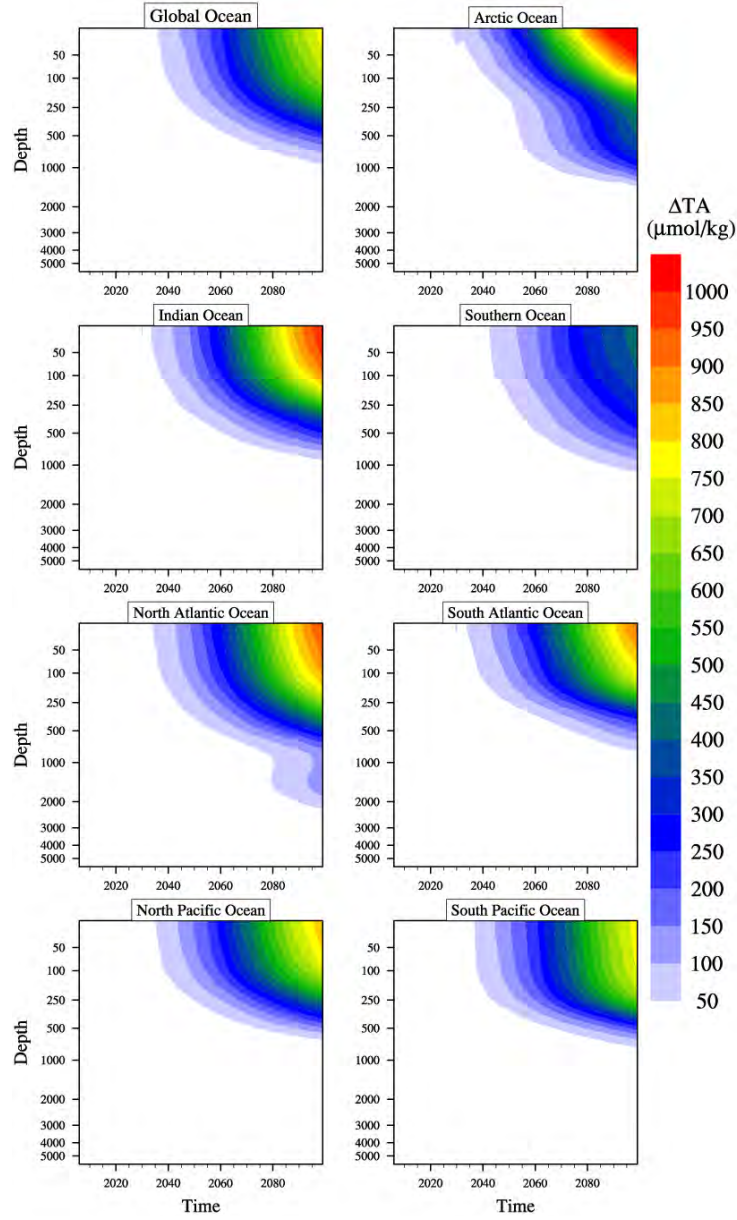
Figure 2.7: Temporal evolution of the vertical profiles of total alkalinity anomaly (ΔTA, μmol/kg) under the AOA scenario considering the difference between the annual means over time and the averaged value of the first ten years of the experiment (2006-2015). From left to right and top to bottom: Global, Arctic, Indian, Southern, North Atlantic, South Atlantic, North Pacific and South Pacific Ocean basins. Note the nonlinear vertical axis in which resolution decreases with depth.

46

Figure 2.8: Temporal evolution of the vertical profiles of dissolved inorganic carbon anomaly (ΔDIC, μmol/kg) under the AOA scenario considering the difference between the annual means over time and the averaged value of the first ten years of the experiment (2006-2015). From left to right and top to bottom: Global, Arctic, Indian, Southern, North Atlantic, South Atlantic, North Pacific and South Pacific Ocean basins. Note the nonlinear vertical axis in which resolution decreases with depth.

Figure 2.9: Temporal evolution of the vertical profiles of the DIC to TA ratio under the AOA scenario showing annual means. From left to right and top to bottom: Global, Arctic, Indian, Southern, North Atlantic, South Atlantic, North Pacific and South Pacific Ocean basins. Note the nonlinear vertical axis in which resolution decreases with depth.
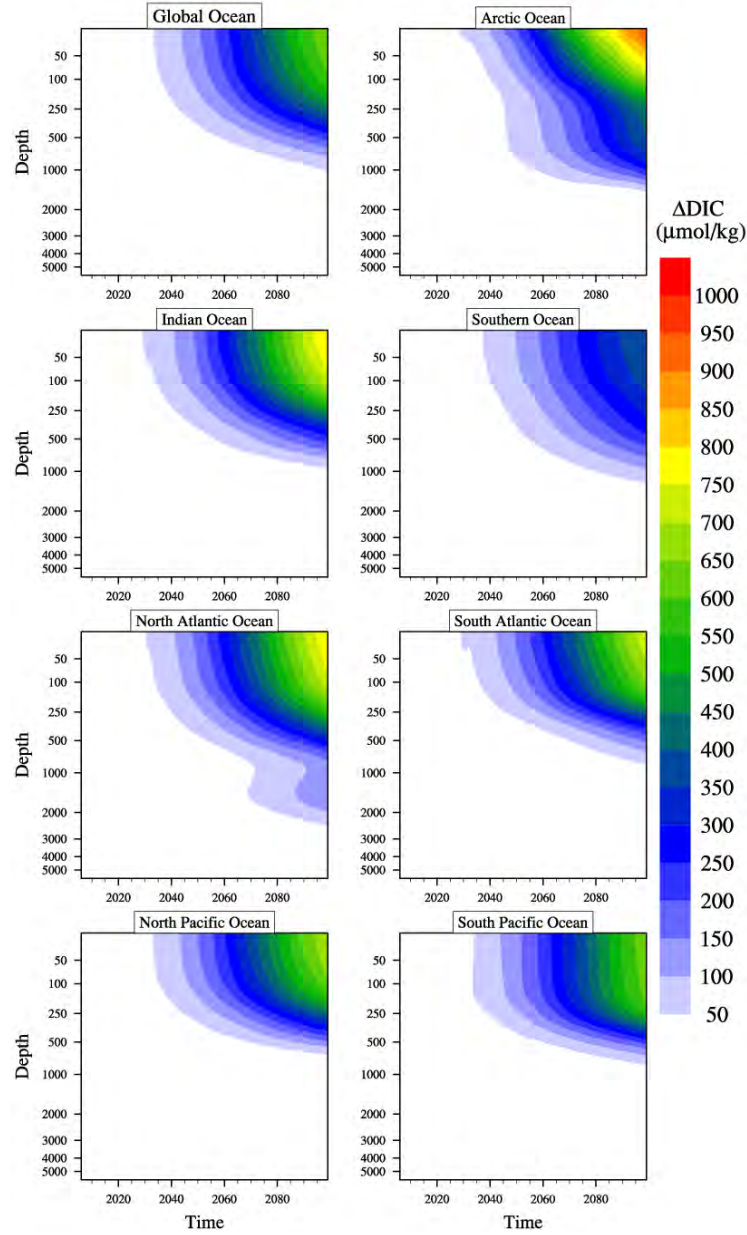
48

Figure 2.10: Temporal evolution of the vertical profiles of pH under the AOA scenario showing annual means. From left to right and top to bottom: Global, Arctic, Indian, Southern, North Atlantic, South Atlantic, North Pacific and South Pacific Ocean basins. Note the nonlinear vertical axis in which resolution decreases with depth.
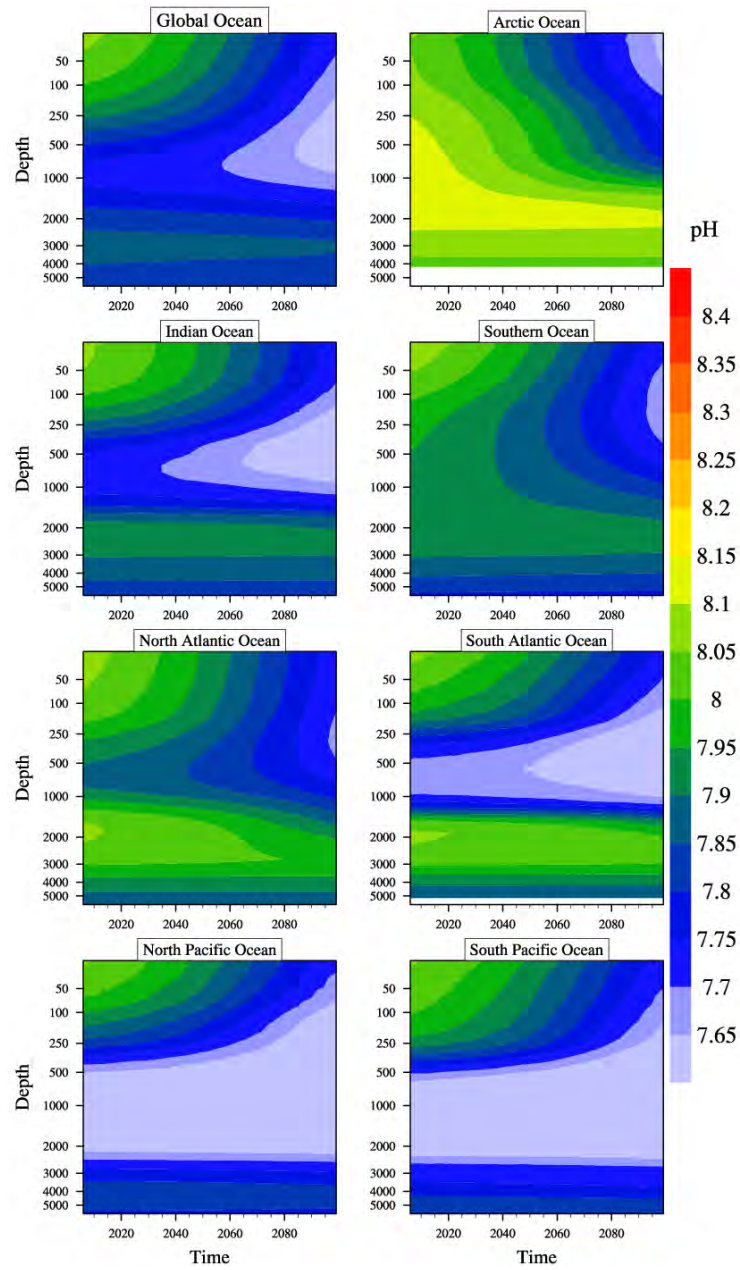
Figure 2.11: Temporal evolution of the vertical profiles of pH under the RCP8.5 scenario showing annual means. From left to right and top to bottom: Global, Arctic, Indian, Southern, North Atlantic, South Atlantic, North Pacific and South Pacific Ocean basins. Note the nonlinear vertical axis in which resolution decreases with depth.
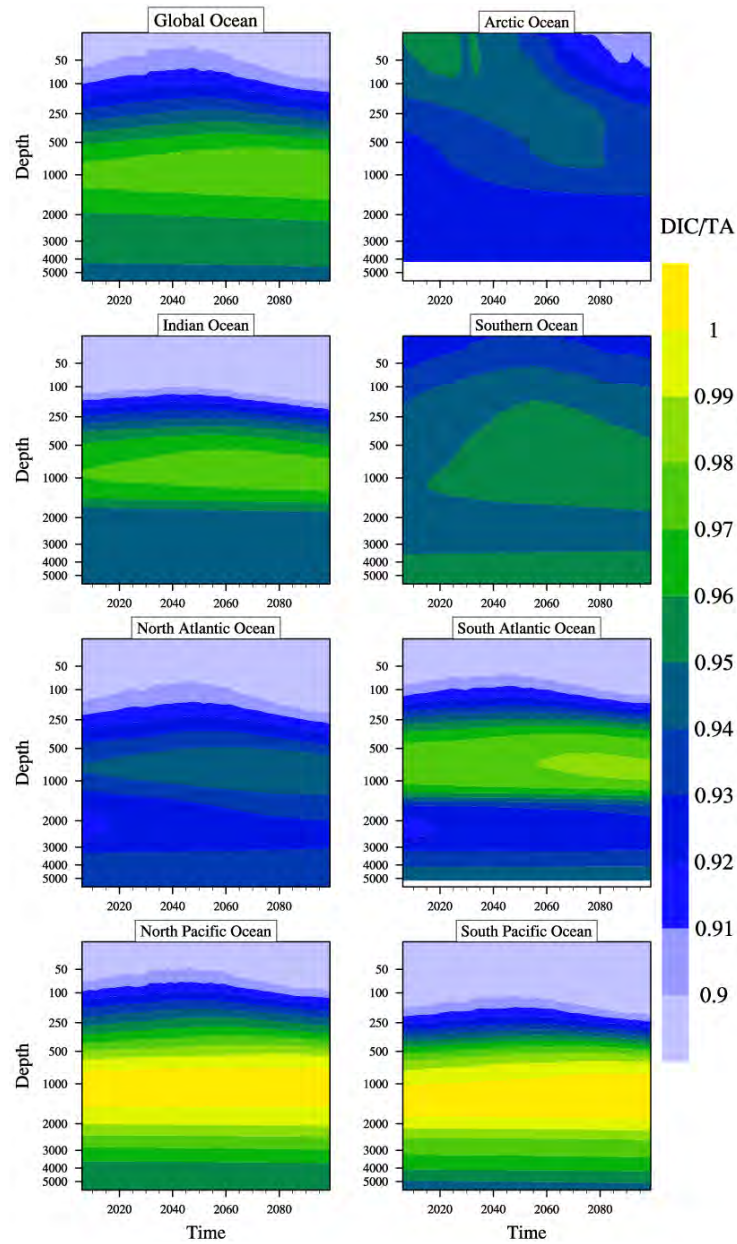
50
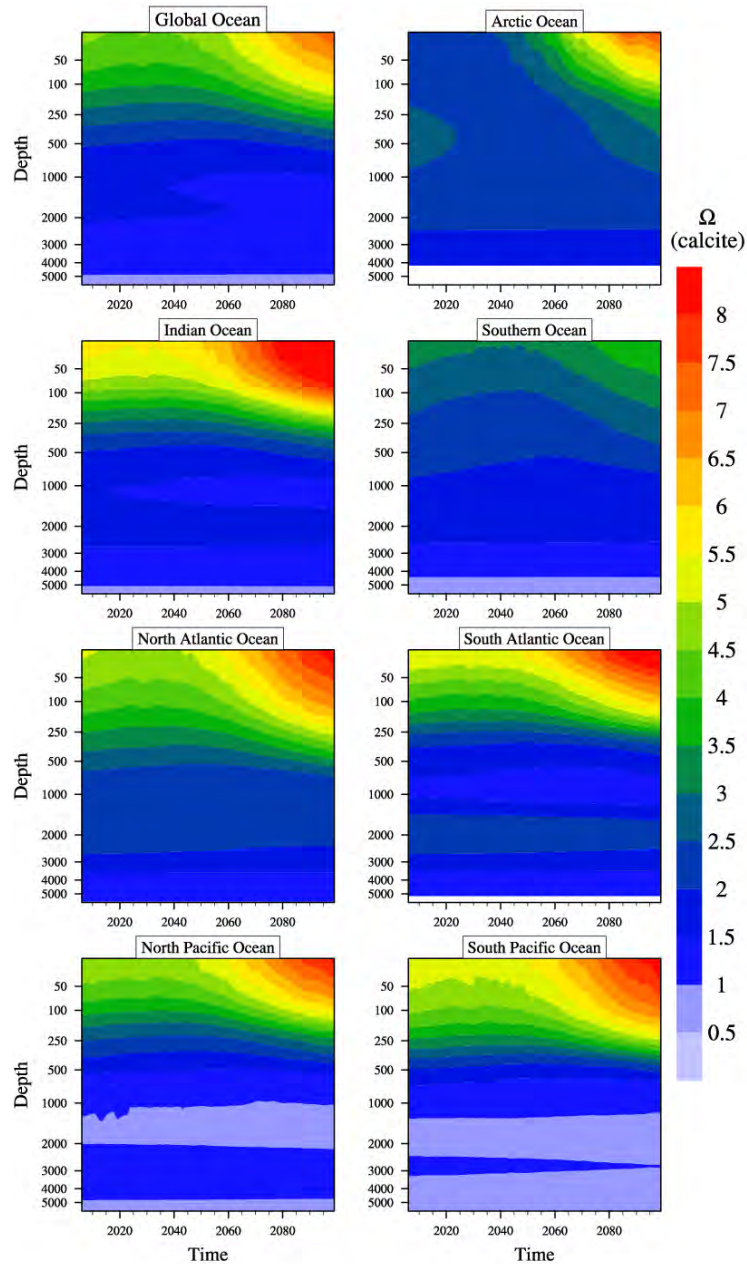
Figure 2.12: Temporal evolution of the vertical profiles of Ω (calcite) under the AOA scenario showing annual means. From left to right and top to bottom: Global, Arctic, Indian, Southern, North Atlantic, South Atlantic, North Pacific and South Pacific Ocean basins. Note the nonlinear vertical axis in which resolution decreases with depth.
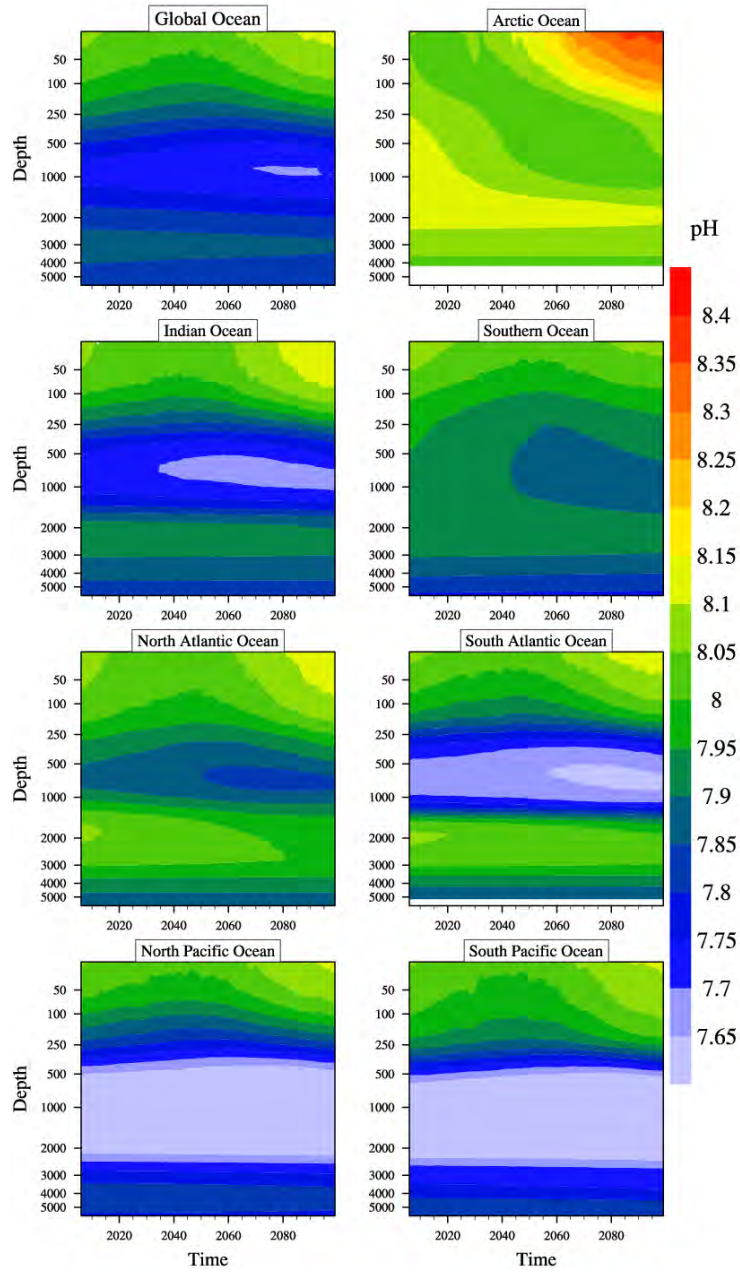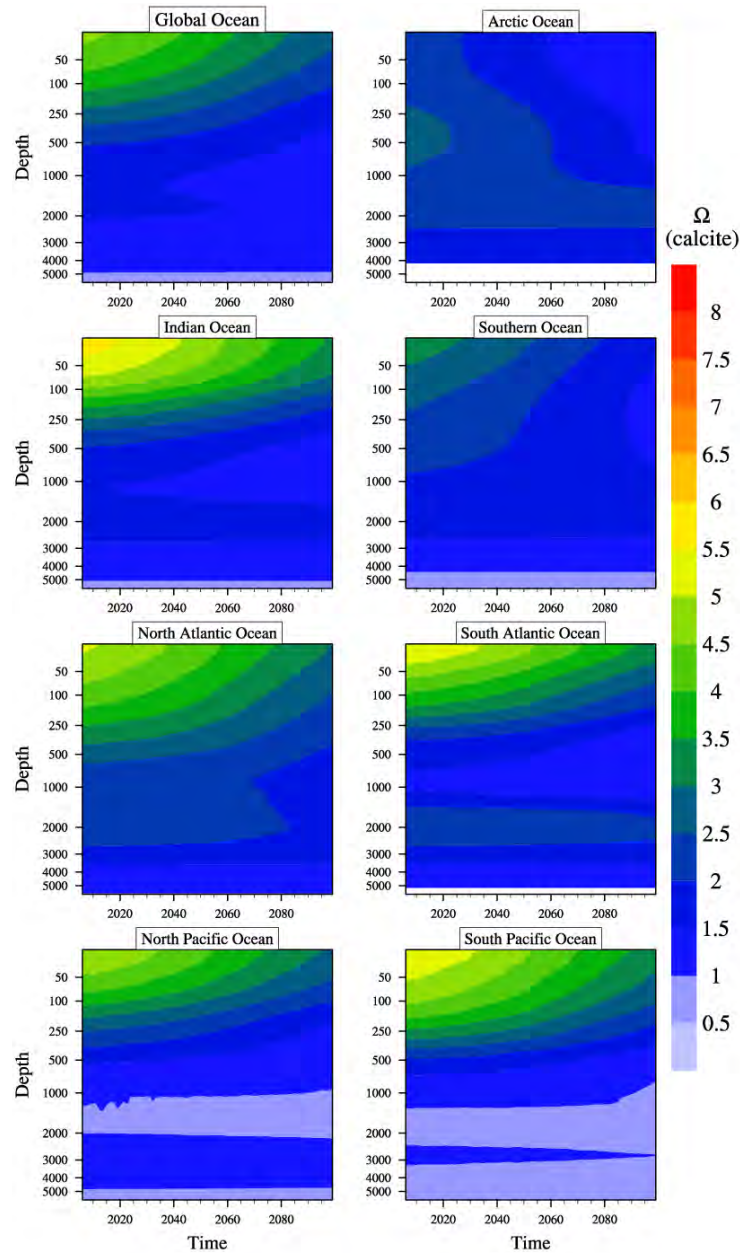
Figure 2.13: Temporal evolution of the vertical profiles of Ω (calcite) under the RCP8.5 scenario showing annual means. From left to right and top to bottom: Global, Arctic, Indian, Southern, North Atlantic, South Atlantic, North Pacific and South Pacific Ocean basins. Note the nonlinear vertical axis in which resolution decreases with depth.

52

Chapter 3

Comparing the Effects on Surface Temperature, Carbon Uptake & Ocean Biogeochemistry of Large-Scale AOA & SRM Scenarios

3.1 Introduction

Climate engineering (CE) methods are intended to mitigate environmental changes caused by climate change (e.g., National Research Council 2015a,b; IPCC 2012). There are two major groups of CE methods: carbon dioxide removal (CDR) methods which are intended to reduce atmospheric CO_2 levels, and solar radiation management (SRM) techniques with the goal of increasing the Earth's albedo. Thus, CDR and SRM methods modulate surface temperatures by their effects on different atmospheric forcings. Since CDR methods decrease atmospheric CO_2, they also alleviate the effects of ocean acidification. The ocean-based CDR method of artificial

ocean alkalinization (AOA) consists of the enhancement of surface seawater alkalinity by releasing alkaline compounds or their dissociation products (e.g., calcium carbonate, olivine, quicklime, calcium hydroxide) (e.g., Kheshgi 1995; González and Ilyina 2016). AOA lowers atmospheric CO_2 levels because this method enhances the seawater buffering capacity what intensifies the ocean carbon sink while seawater acidity decreases. Stratospheric sulfur injection is a SRM methods in which by scattering sulfur into the low stratosphere, aerosol particles are formed and the Earth's albedo is enhanced (e.g., Crutzen 2006; Schmidt et al. 2012). These aerosol particles reflect more incoming shortwave radiation back to space what diminishes the net top-of-atmosphere (TOA) radiation so that surface warming is mitigated. Because these CE techniques have fundamentally different effects on the Earth system, it is challenging to comparatively assess their consequences.

CE-driven effects on the Earth system are usually compared using results of CE simulations that were computed with different models and based on different scenarios (e.g., Keller et al. 2014; National Research Council 2015a,b; IPCC 2012). This approach complicates the comparison of the methods and may even lead to biased conclusions. This is because these comparisons include, not only the differences between the methods, but also differences between the models and CE scenarios. Model results depend upon their underlying parameterizations and the actual impact of CE on the Earth system is defined by the characteristics of the method and the intensity of the scenario. Differences in the Earth's system response to CE caused by the particular characteristics of the method and scenario are unavoidable. However, the comparison of different CE methods based on one model, filters discrepancies caused by differences in the parameterizations of the represented processes. There exists only one study that compares several CE methods which scenarios were simulated using the same model (Keller et al. 2014). The effectiveness and side-effects of different CE methods (including AOA and SRM) were assessed using an Earth system model of intermediate complexity without interactive carbon cycle. Here we study the CE methods of AOA and SRM using the Max Planck Institute Earth System Model (MPI-ESM) with prognostic carbon cycle. The MPI-

ESM simulates the Earth's climate system by coupling the atmospheric (ECHAM6) and ocean (MPIOM) general circulation models.

We compare the CE-driven effects on the Earth system with idealized large-scale simulations of AOA and SRM via stratospheric sulfur injection based on the Representative Concentration Pathways (RCP) scenarios (van Vuuren et al. 2011). The MPI-ESM is forced by CO_2 emissions with the configuration used in the fifth phase Coupled Model Intercomparison Project (CMIP5) (Giorgetta et al. 2013). The RCP scenarios (van Vuuren et al. 2011) serve as model forcing and they are also used to define the CE scenarios. The high CO_2 emissions scenario RCP8.5 is the reference scenario that forces the CE simulations. The intensity in the implementation of CE is determined by targeting different climatic parameters of the RCP4.5 scenario. In the AOA simulations, atmospheric CO_2 concentrations are stabilized to RCP4.5 levels by adding as much alkalinity as needed into the surface ocean. In the SRM experiments, the simulated stratospheric sulfate aerosol distribution reduces the radiative forcing of the RCP8.5 scenario to RCP4.5 levels. In order to study the effects of CE during the implementation and after the termination of these methods, we consider AOA and SRM scenarios in which the methods are either continuously applied until 2100 or terminated in 2070.

We explore the response of the Earth system to these large-scale AOA and SRM scenarios by taking two different perspectives: by considering their effects on the rate of environmental change and their effects on the seasonal variability. We give special focus to the effects of CE on the global carbon cycle and the ocean biogeochemistry. We go beyond previous comparisons of AOA and SRM because our modeling approach includes interactions between the different elements of the Earth system that were previously neglected. Both methods are simulated using the same model, which allows the consistent comparison of their effects and excludes differences due to model parameterizations. Further, unlike previous studies, our modeling approach includes internal model variability whereby the model trajectory can be discussed in the context of internal variability.

3.2 Methodology

3.2.1 Climate Engineering Scenarios

A detailed model description is given in Appendix A but the specific methodological approach of this chapter is described here. Idealized climate engineering (CE) scenarios are implemented in the Max Planck Institute Earth system model (MPI-ESM) simulating two completely different CE methods: artificial ocean alkalinization (AOA) and solar radiation management (SRM) via stratospheric sulfur injection (see overview in Table 3.1). The representative concentration pathways (RCP) scenarios RCP8.5 and RCP4.5, are compared with the CE simulations because whilst the CE experiments use the RCP8.5 forcing, they are defined such that they target different parameters of the RCP4.5 scenario. A detailed description of the RCPs experiments can be found in van Vuuren et al. (2011) and references therein.

The AOA scenario is formulated so that surface ocean alkalinity is enhanced as much as needed to stabilize atmospheric CO_2 concentrations to RCP4.5 levels under RCP8.5 emissions (Figure 3.1, left). In total, around $114 \cdot 10^{15}$ mol (Pmol) of added alkalinity are required to meet this scenario until the end of this century. Alkalinity is homogeneous (per unit area) and globally (including areas of sea ice growth) distributed in every time step into the first 12 meters of the ocean (slightly modified by the time-varying sea surface elevation). Dissolved inorganic content (DIC), trace metals and nutrients are not modified during the AOA scenario. The distribution of alkalinity starts in the year 2018, when atmospheric CO_2 concentration (global average) differs from the one of the RCP4.5 scenario by app. 1%.

The SRM scenario is defined such that the stratospheric sulfate aerosol distribution reduces the net radiative forcing of the RCP8.5 scenario to RCP4.5 levels (Figure 3.1, right). By the end of this century, the annual rate of sulfur injection reaches around 20 Megatons. ECHAM6 does not account for an explicit formulation of aerosols distribution. Thus, the radiative effects of the sulfate aerosols were considered by

Experiment Name	Brief Description
Historical	Initialized from preindustrial control. It runs from 1850 to 2005 with prescribed anthropogenic CO_2 emissions and imposed evolving forcings consistent with observations.
RCP8.5	Continuation of experiment Historical into the future until 2100 with prescribed anthropogenic CO_2 emissions and a radiative forcing reaching approx. 8.5 W/m^2 by 2100.
RCP4.5	Continuation of experiment Historical into the future until 2100 with prescribed anthropogenic CO_2 concentrations and radiative forcing reaching approx. 4.5 W/m^2 by 2100.
AOA2100	Model forced as in the RCP8.5 experiment with artificial ocean alkalinization (AOA) applied until 2100, such that atmospheric CO_2 concentrations are stabilized to RCP4.5 levels.
AOA2070	Same as AOA2100 but the AOA method ceases in 2070 and the experiment runs until 2100.
SRM2100	Model forced as in the RCP8.5 experiment with the solar radiation management (SRM) method of stratospheric aerosol enhancement applied until 2100, such that net radiative forcing follows the RCP4.5 trajectory.
SRM2070	Same as SRM2100 but SRM ceases in 2070 and the experiment runs until 2100.

Table 3.1: Overview of the experiments used in this chapter, more details are given in the text. The experiments Historical, RCP8.5, RCP4.5 (respectively referred to as *esmHistorical*, *esmrcp85*, *rcp45* in Giorgetta et al. (2013)), are the simulations run during the fifth phase Coupled Model Intercomparison Project (CMIP5).

prescribing their impact on the atmospheric optical properties which were determined using the aerosol microphysical model HAM (Stier et al. 2005) coupled to MAECHAM5 (Giorgetta et al. 2006). The release of sulfur into the stratosphere follows a similar approach to that of Niemeier et al. (2013). All the simulations of SRM were implemented and carried out in the MPI-ESM by Sebastian Sonntag.

The simulated period is between 2006 and 2100 for the all the RCP and CE experiments whilst the Historical experiment runs from 1850 to 2005. Two sets of CE experiments were carried out: one set in which the implementation of CE lasts continuously until the end of the 21st century (labeled as AOA2100 and SRM2100) another set in which CE is interrupted in 2070 but the simulations run until 2100 (referred to as *termination scenarios* and called AOA2070 and SRM2070). Model internal variability is considered with an ensemble of three members available for each and every of our scenarios. The forcing used to compute each ensemble member is identical but each member is initialized using the end of the associated ensemble member of the Historical experiments (defined as *esmHistorical* in Giorgetta et al. (2013).

3.2.2 Regression Analysis for Calculating the Rates of Change

The rates of decadal changes in some selected variables are analysed using the simple Theil-Sen (TS) regression technique (Gilbert 1987). The distribution-free TS method is more robust than the commonly used method of generalized least squares because it is less sensitive to outliers. The trends are estimated using three ensemble members of each simulation and by fitting the data of each grid point (annual means between 2070 to 2100) to $y_t = \alpha + \beta t$; where y_t is the data at time t, α is the intercept and β is the non-parametric estimate of the slope. The statistical significance of the linear trends is determined using the Mann-Kendall test that does not require normality (Mann 1945; Kendall 1975).
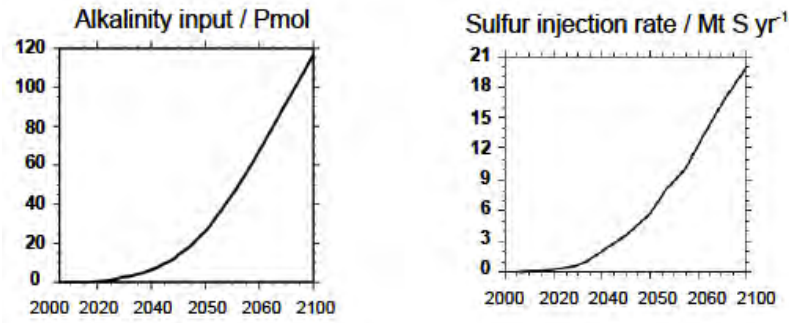
Figure 3.1: Cumulative alkalinity input and sulfur injection rate in the CE scenarios continuously implemented until 2100: artificial ocean alkalinization (AOA2100, left) and solar radiation management via stratospheric sulfur injection (SRM2100, right). For the experiments in which the implementation of CE ceases in 2070, the same alkalinity input and sulfur injection rate than in the experiments AOA2100 and SRM2100 are applied but only until the year 2070.

3.2.3 Metrics of Seasonality

To analyse potential changes in the seasonality of selected model variables, we use the so called *amplification factor* (AF). It is the ratio of the average seasonal amplitude (maximum monthly mean minus minimum within the year) at the end of the 21st century to the average seasonal amplitude of the historical period. We consider the seasonal amplitude of the historical period as simulated in the Historical experiment, which monthly output is averaged between the years 1986 and 2005 for the analysis of the surface temperatures, and between 1996 and 2005 for the analysis of the seawater biogeochemical variables. Projected seasonal amplitudes under the different climate change and CE scenarios are obtained by averaging monthly output of the last two decades of the 21st century of surface atmospheric/seawater temperature, and only the last decade of the 21st century for the analysis of seawater biogeochemical parameters (e.g. pH, Ω and marine net primary production). Thus, our seasonal metric AF is obtained in the following manner:

1) the maximum and minimum monthly means are extracted for each of the years in the considered time intervals,

2) for each year these pairs are subtracted (i.e. the maximum minus the minimum),

3) the set of differences obtained for the different periods is averaged in order to reduce bias due to interannual variability.

4) Finally, the AF of a variable "Y" is the ratio of the perturbed (due to climate change or geoengineering) seasonal amplitude to the reference one (i.e. seasonal amplitude as simulated during the last period of the historical simulation):

$$\text{AF} = \frac{(Y^{\max} - Y^{\min})_{\text{perturbed state}}}{(Y^{\max} - Y^{\min})_{\text{reference state}}} \qquad (3.1)$$

3.3 Effects on the Mean State

3.3.1 Surface Temperature & Sea Ice

Compared to pre-industrial times, the Earth's surface has warmed by 0.78 K mainly owing to the accumulation of atmospheric CO_2 released by human activities (IPCC 2013). Atmospheric CO_2 concentration at the surface rose from $\sim$277 parts per million (ppm) prior the onset of the industrial era (Joos and Spahni 2008) to above 400 ppm after 2015 (Le Quéré et al. 2015). The RCP8.5 emission scenario assumes high energy demand and greenhouse gases (GHGs) emissions without mitigation actions against climate change. Following the RCP8.5 scenario, atmospheric CO_2 is projected to exceed 950 ppm in ESM such as the MPI-ESM by the end of the 21st century (Figure 3.2a). The changes in the Earth's radiative budget mainly driven by the increasing CO_2 levels, are expected to warm global surface atmospheric temperatures by around 3.5 K by the year 2100 (Figure 3.2b). In this warmer climate state, the area covered by sea ice in both hemispheres halves its current values (Figure 3.3).

Further, the boreal summer sea ice is projected to disappear in ESM simulations under the RCP8.5 scenario around the year 2070. The projected warming is not geographically homogeneous. Over land the warming is more pronounced than over ocean (Figure 3.4) because of the lower heat capacity of land surfaces relative to the one of the ocean. Due to polar amplification, warming is larger at high latitudes, with the polar and subpolar regions of the Northern hemisphere emerging as the most affected areas. By the year 2100, near-surface atmospheric temperatures in the RCP8.5 scenario over the Arctic, reach up to 8 K higher temperatures relative to the historical period.

Our analysis of CE-driven effects on the Earth system includes surface temperatures and sea ice, not only due to their relevance for climate phenomena, but also because they determine seawater biogeochemistry, which is our main focus. In the large-scale SRM scenario continuously applied until the year 2100 (referred to as SRM2100), the net radiative forcing of the RCP8.5 scenario is reduced to RCP4.5 levels via stratospheric sulfur injection. This greatly lowers the near-surface atmospheric temperatures which closely follows the temporal evolution of the targeted RCP4.5 scenario (Figure 3.2b). During the last decade of the 21st century, global annual means of surface atmospheric temperature in the SRM2100 scenario are $\sim$0.2 K higher than in the RCP4.5 due to small differences in the surface energy fluxes between these simulations. The strong sea ice decay of the RCP8.5 scenario is reduced in the SRM2100 simulation because of the prevented warming over polar regions (Figure 3.4). In the large-scale AOA scenario in which the addition of alkalinity into the surface seawater lasts until 2100 (AOA2100), the atmospheric CO_2 is brought to RCP4.5 levels under RCP8.5 emissions. This reduces the CO_2 radiative forcing to RCP4.5 values, and thereby the surface atmospheric temperatures to similar values than those in the RCP4.5 scenario. AOA only alters atmospheric CO_2 levels and this method does not modify the radiative effects of different (than CO_2) forcing agents. That is why the AOA2100 scenario projects higher surface atmospheric temperatures ($\sim$0.5 K) compared to the RCP4.5 by the end of this century. Regarding the simulations with CE until 2100, AOA2100 has slightly warmer ($\sim$0.3

K) surface temperatures than the SRM2100 scenario. Internal model variability of surface atmospheric temperatures is relatively large compared to the one of atmospheric CO_2 levels, but still the CE signals are easily distinguishable. Trends of surface atmospheric warming in the AOA2100 and SRM2100 scenarios are consistent among the ensemble members, and their ranges of internal variability do not overlap during the last decades of integration. In contrast, the internal model variability of sea ice is so large that differences in the temporal evolution of sea ice between the AOA2100 and SRM2100 scenarios are indistinguishable.

The impact of the sudden termination of SRM on the climate state is one of the major concerns regarding the potential implementation of SRM methods. The effects of SRM cessation on the climate have been studied within the Geoengineering Model Intercomparison Project (GeoMIP). Specifically, the G2 experiment was designed to study this aspect of SRM (Jones et al. 2013). In the G2 experiment, the net radiative forcing of the CMIP5 simulation *1pctCO2* (i.e. 1% CO_2 increase per year from preindustrial levels (Taylor et al. 2012)) was counteracted by a gradual lowering of the solar constant simulating the effects of SRM deployment. The counterbalance in net radiative forcing was stopped in the year 2050. Then, surface atmospheric temperatures reach between 60 to 100% of the reference simulation without CE within the five years following the simulated sudden termination of SRM in all the climate models that took part in this study (Jones et al. 2013).

The results of our terminated SRM scenario (SRM2070), in which the net radiative forcing of the RCP8.5 is reduced to RCP4.5 levels via SRM until 2070, resemble those of the G2 experiment. Right after termination of SRM in 2070, near-surface atmospheric temperatures rapidly converge to the reference RCP8.5 scenario (rates of warming are discussed in more detail in section 3.4.1). By the year 2100, surface temperatures in the SRM2070 experiment are similar to those of the RCP8.5 scenario. The warming is spatially inhomogeneous. The highest values (up to 7 K relative to the historical period) are reached over polar regions in the Northern hemisphere, and the sea ice areas in both hemispheres in the SRM2070 scenario reach the same mean states projected in the RCP8.5 by 2100. Compared to the SRM2070

scenario, the global warming and sea ice melting after sudden termination of CE in the AOA2070 simulation are less pronounced following the pace set by the rates of atmospheric CO_2 increase. The increase in atmospheric carbon after the year 2070 in the AOA2070 experiment, is defined by the emissions of the reference RCP8.5 scenario, and the carbon stored in seawater via AOA remains bound in the ocean reservoir. The offset in atmospheric CO_2 levels ($\sim$ 160 ppm) between the RCP8.5 and AOA2070 scenarios, prevents the increase in global surface temperature by 0.5 K.
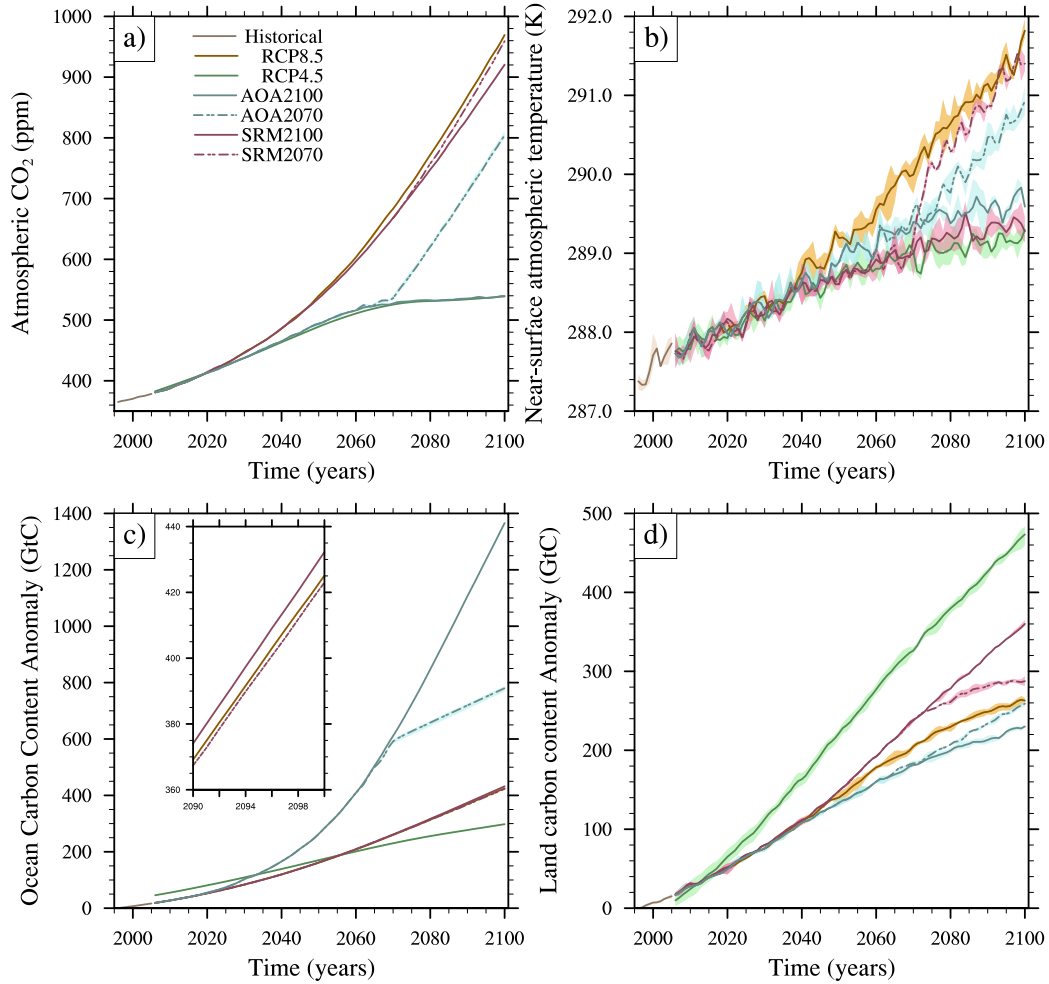
Figure 3.2: Temporal evolutions of various Earth system variables in different scenarios. Lines depict 5 year running means under the scenarios Historical (brown), RCP8.5 (orange), RCP4.5 (green), AOA2100 (solid blue), AOA2070 (dashed blue), SRM2100 (solid violet) and SRM2070 (dashed violet). (a) global annual mean of atmospheric CO_2 (ppm), (b) global annual mean of near-surface atmospheric temperature (K), (c) anomaly in carbon content in the ocean reservoir (GtC), (d) anomaly in carbon content in the land reservoir (GtC). Colored area is model internal variability including three ensemble members.

64

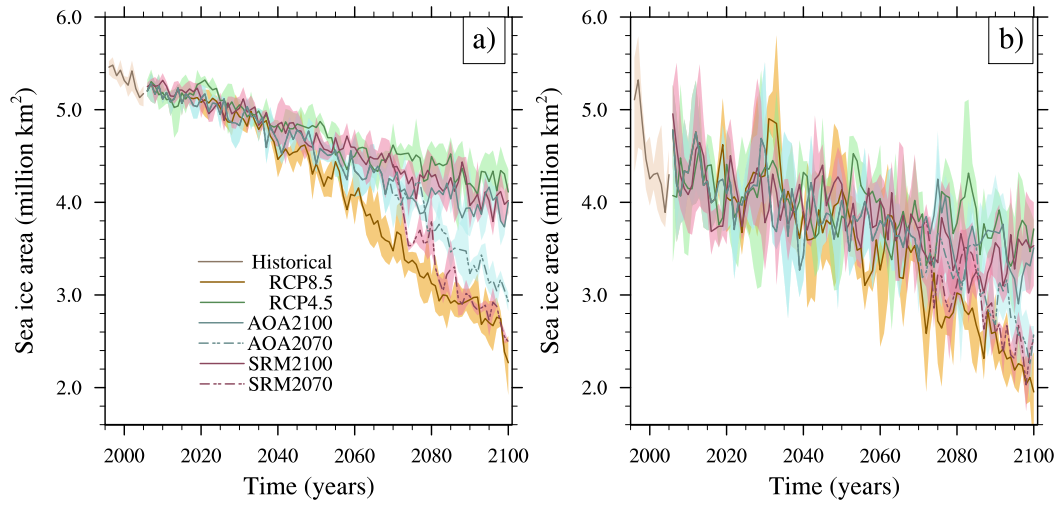Figure 3.3: Temporal evolutions (5 year running means) of sea ice area (million km^2) in the polar caps of the (a) Northern hemisphere and (b) Southern hemisphere under the scenarios Historical (brown), RCP8.5 (orange), RCP4.5 (green), AOA2100 (solid blue), AOA2070 (dashed blue), SRM2100 (solid violet) and SRM2070 (dashed violet). Colored area is model internal variability including three ensemble members.
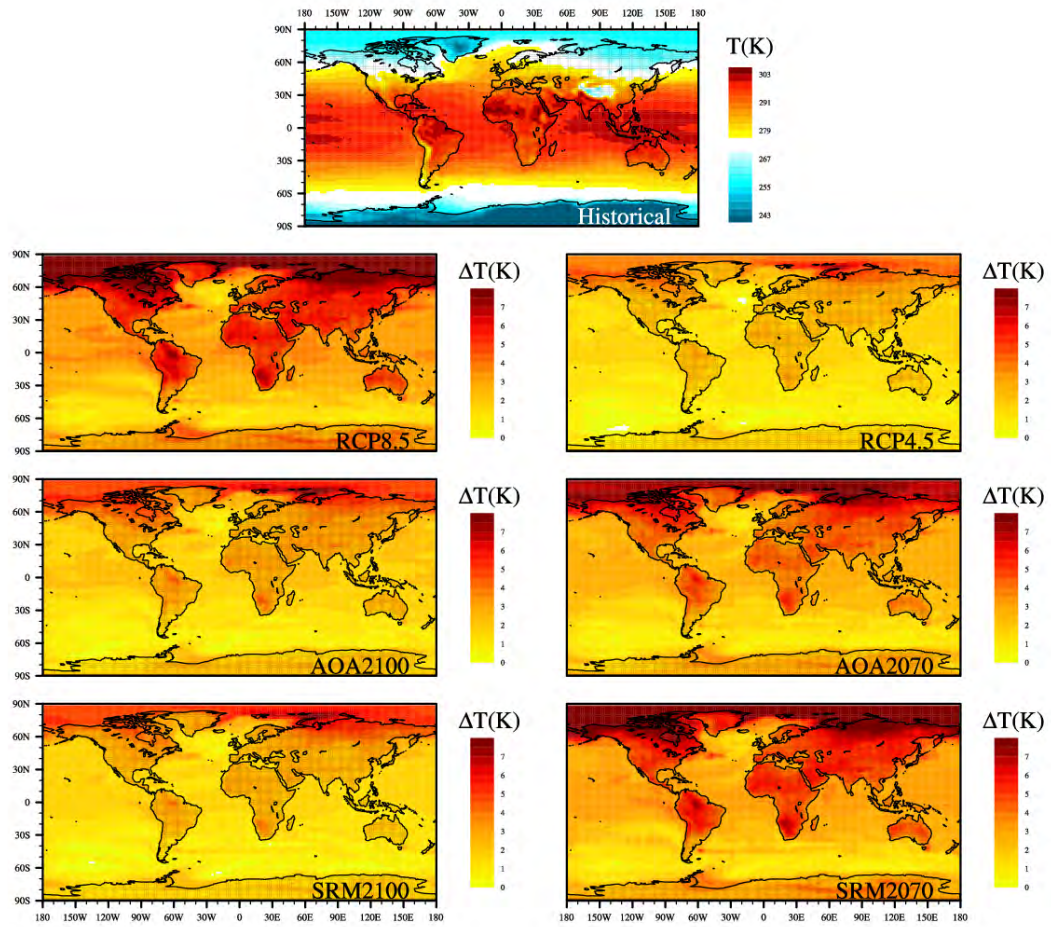
Figure 3.4: Average annual means (from 1985 to 2005) of near-surface atmospheric temperature in the Historical simulation (upper map) and the anomalies between this simulation and the last two decades of the scenarios (from left to right and top to bottom) RCP8.5, RCP4.5, AOA2100, AOA2070, SRM2100 and SRM2070.

66

3.3.2 Carbon Uptake

The projection of the responses of the ocean and land carbon sinks due to changes in climate is a big challenge ahead (Ilyina and Friedlingstein 2017). Substantial uncertainties arise not only because of the large variety of non-linear processes and feedbacks involved, but also due to our limited understanding of the underlying mechanisms. Some responses are better identified than others. For instance, increasing surface temperatures suppress the ocean sink because CO_2 is less soluble at warmer temperatures, which lowers the solubility pump (Heinze et al. 1991). Changes in ocean currents and stratification driven by global warming also induce the decline in ocean carbon uptake (Maier-Reimer 1993; Sarmiento et al. 1998). In our SRM2100 simulation, the cooling of sea surface temperatures (SST, Figure 3.5) alters the ocean carbon pumps which define seawater-atmosphere CO_2 exchange. CO_2 solubility increases with decreasing SST, thereby enhancing the solubility pump. The reduced warming also prevents the enhanced thermal stratification of the water column (Figure 3.6), and thus the decline in ocean net primary production (NPP) driven by the lower vertical entrainment of nutrient-rich waters into the euphotic zone (Behrenfeld et al. 2006). By the end of the simulated period, the storage of carbon in the ocean is enhanced by 8 GtC in the SRM2100 scenario relative to the reference RCP8.5 (Figure 3.2c).

Main mechanisms governing the land carbon sink, are less understood than those of the ocean sink (Ilyina and Friedlingstein 2017). Over timescales ranging from decades to millennia, changes in surface temperatures alter the terrestrial carbon sink primarily through their effect on the terrestrial biosphere. The moderate increase in temperatures may stimulate the net uptake of atmospheric CO_2 by primary producers over land (King et al. 1997). However, warming also enhances heterotrophic respiration in soils, thereby increasing the release of carbon from the land surface to the atmosphere (e.g., Jenkinson et al. 1991; Townsend et al. 1992). Regional precipitation patterns largely determine the vegetation cover and therefore, carbon fluxes over land owing to changes in water availability. In line with previous

model studies of SRM, global precipitation declines in our SRM2100 scenario over the century in contrast to the projected increase in the RCP8.5 (Sonntag et al. submitted). Regionally, precipitation decreases at high latitudes and tropical regions, but it increases over large areas of South America, Africa and Australia. This enhanced local precipitation decreases water stress which boosts the uptake and storage of carbon by the land biosphere in these regions (Figure 3.7c). Moreover, compared to the RCP8.5 scenario, the prevented warming in the SRM2100 simulation weakens the projected boreal forest expansion under the RCP8.5. This temperature-driven effect, together with the reduced precipitation over boreal forests, decrease the carbon stored in land at high latitudes of the Northern hemisphere. Atmospheric CO_2 concentration also impacts vegetation distribution and the strength of the terrestrial carbon sink through the CO_2 fertilization effect, to which the MPI-ESM is especially sensitive (e.g., Bathiany et al. 2014; Sonntag et al. 2016). Thus, in the colder (than RCP8.5) and high CO_2 world of the SRM2100 scenario, the land carbon sink is further boosted by the elevated CO_2 concentrations via CO_2 fertilization. In our SRM2100 simulation, the reduction in atmospheric CO_2 levels by 46 ppm relative to the RCP8.5 scenario in the year 2100, is dominated by the impacts of SRM on the terrestrial carbon sink (Figure 3.2). By the end of the century, whilst the ocean carbon reservoir in the SRM2100 simulation is only 8 GtC higher than in the RCP8.5 scenario, the terrestrial carbon pool in the SRM2100 experiment is 92 GtC higher than in RCP8.5.

Previous studies have addressed the CDR mitigation potential of SRM methods. Keller et al. (2014) also found that the prevented warming in SRM scenarios boosts the uptake of atmospheric CO_2 by land and ocean with a predominant role of the terrestrial carbon sink. Tjiputra et al. (2016) obtained in SRM simulations that the ocean sink was the greater contributor to a small reduction of atmospheric CO_2 levels concomitant to the lowering of surface temperatures. The ESM and experimental setup used by Tjiputra et al. (2016) is more comparable to ours than the one used by Keller et al. (2014). Still, the response of the land sink is weaker than the one obtained in our SRM2100 simulation. Tjiputra et al. (2016) used prescribed CO_2

emissions due to land use changes instead of prognostically calculated as in our modeling approach. Moreover, in contract to the MPI-ESM, the marine carbon sink in their model is more sensitive to changes in climate and atmospheric CO_2 levels than the land sink, which might explain the different responses of the carbon uptake to SRM between our results and those of Tjiputra et al. (2016).

Surface warming after termination of SRM ($\sim$1.6 K global average over 3 decades) induces the decrease in the SRM-driven enhanced terrestrial and oceanic carbon storage. The additional carbon (relative to RCP8.5) stored in land and ocean due to the effects of SRM in the SRM2070 simulation returns to the atmosphere. This rises the atmospheric CO_2 concentration by approximately 46 ppm during the last decades of the SRM2070 simulation. By the year 2100, the RCP8.5 and SRM2070 scenarios reach the same (global average) concentration of atmospheric CO_2 ($\sim$ 960 ppm). Thus, any SRM mitigating effect in terms of atmospheric CO_2 reduction vanishes within the following decades after the implementation of SRM ends.

Once alkalinity is added into the surface ocean, the seawater carbonate system re-equilibrates by taking up CO_2 from the atmosphere (Zeebe and Wolf-Gladrow 2001). The effects of this chemical sequestration overwhelm any changes in the uptake and storage of carbon by seawater driven by the changes in the ocean carbon pumps owing to the colder climate state. The enhanced ocean carbon uptake in the AOA2100 scenario is defined by the target set in this simulation: atmospheric CO_2 concentration is stabilized to RCP4.5 levels under RCP8.5 emissions via AOA until 2100. The homogeneous global addition of 114 Pmol of alkalinity (in total) into the surface seawater until the year 2100 enhances the ocean carbon content by $\sim$ 940 GtC. This large-scale AOA scenario affects the carbon uptake and storage over land because the lowering of atmospheric CO_2 reduces the effect of CO_2 fertilization on the terrestrial biosphere.

Sequestered carbon through AOA remains bound in seawater, but alkalinity needs to be constantly supplied into the surface seawater in order to support the enhancement of the buffering capacity and thereby the ocean carbon sink. When the

large-scale AOA scenario ends in 2070, the seawater buffering capacity returns to RCP8.5 levels within years. Then, the global ocean sink continues tempering the growing atmospheric CO_2 concentrations, yet at the same pace than in the reference RCP8.5 scenario (Figure 3.2c). Global averages of atmospheric CO_2 levels and surface temperatures increase parallel to the RCP8.5 trajectory (Figures 3.2a and 3.2b), leading to a growing land carbon content over time (Figure 3.2d). The higher land carbon content (relative to current land carbon reservoir) in the AOA2070 experiment reaches the same value than the reference RCP8.5 scenario by the end of the simulated period (~ 250 GtC).
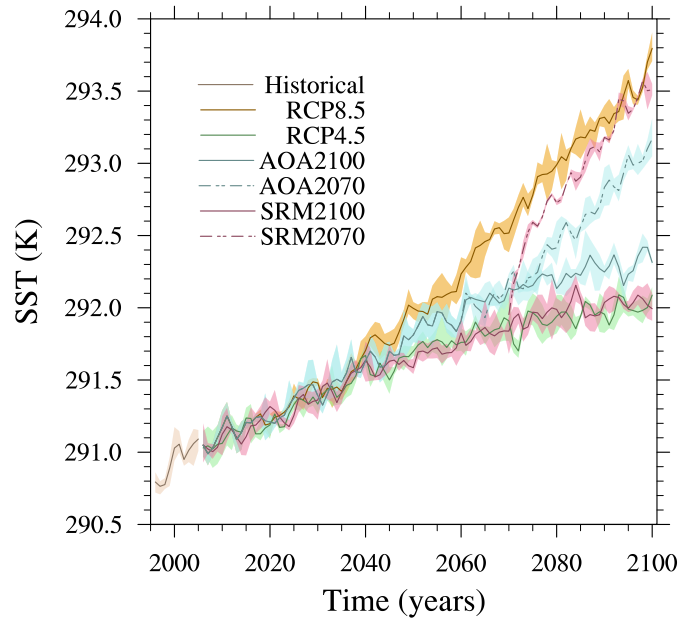

Figure 3.5: Temporal evolution of global annual means of sea surface temperatures (SST) in different scenarios. Lines depict 5 year running means under the scenarios Historical (brown), RCP8.5 (orange), RCP4.5 (green), AOA2100 (solid blue), AOA2070 (dashed blue), SRM2100 (solid violet) and SRM2070 (dashed violet). Colored area is model internal variability including three ensemble members.
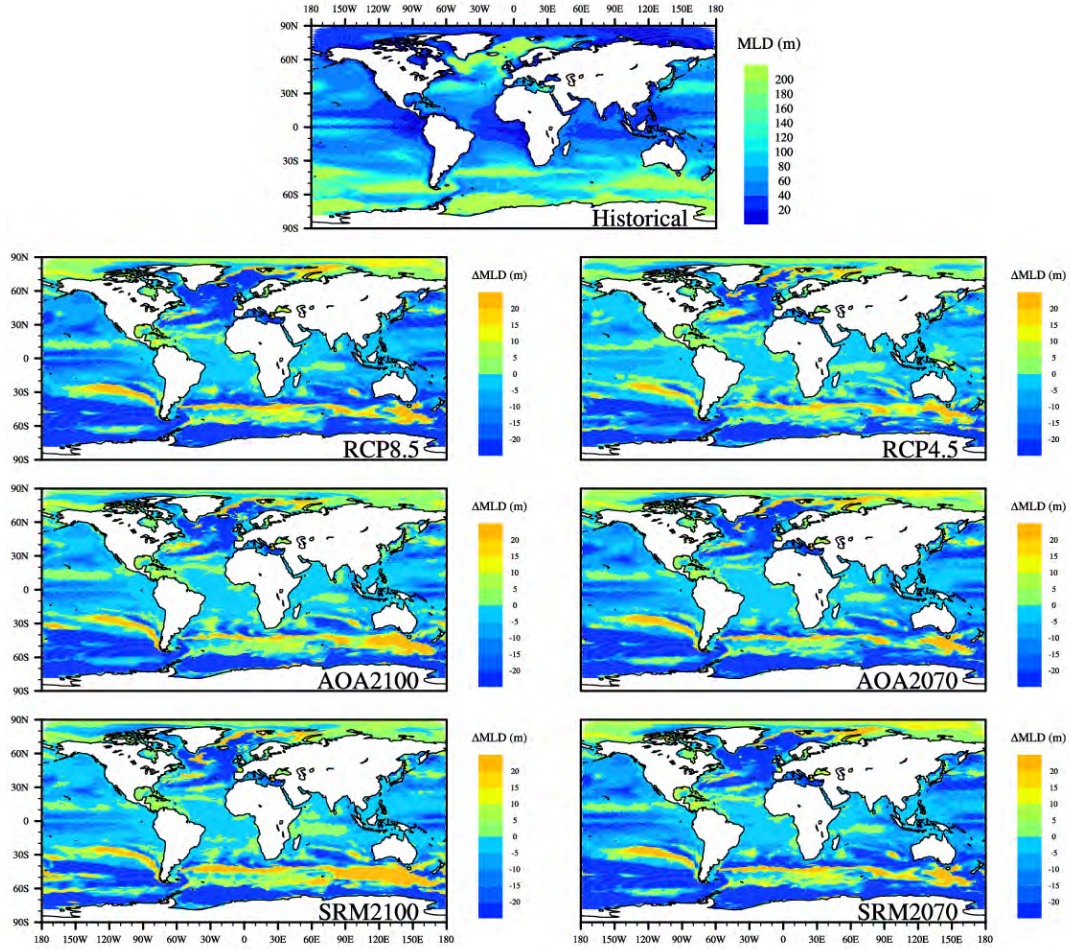
Figure 3.6: Average annual means (from 1985 to 2005) of the mixed layer depth (MLD, meters) in the Historical simulation (upper map) and the anomalies between this simulation and the last two decades of the scenarios (from left to right and top to bottom) RCP8.5, RCP4.5, AOA2100, AOA2070, SRM2100 and SRM2070.

Figure 3.7: Anomalies of the terrestrial and oceanic carbon budgets: differences between the carbon reservoirs of the CE scenarios ((a) AOA2100, (b) AOA2070, (c) SRM2100 and (d) SRM2070) and the reference RCP8.5 in the year 2100. Note the nonlinear color bar.

3.3.3 Seawater Carbonate Chemistry

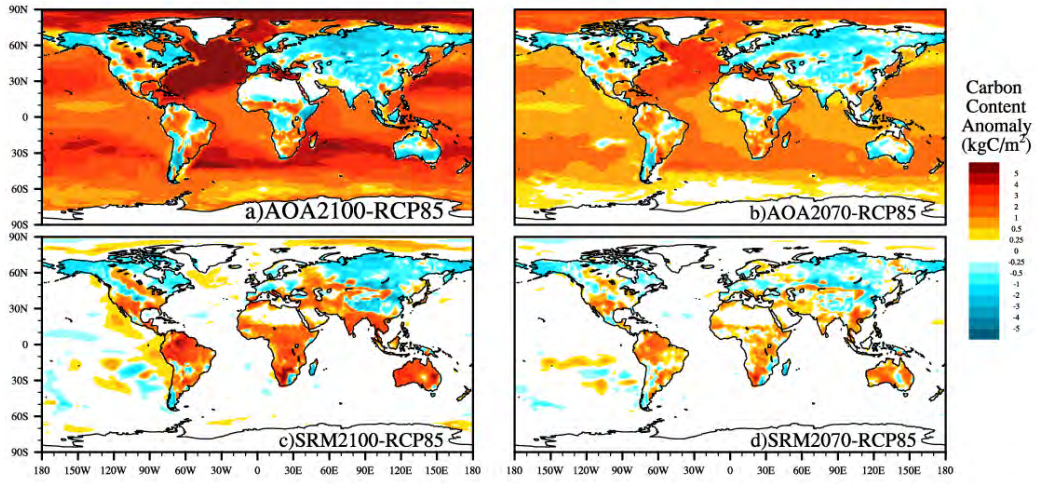The enhanced uptake of carbon by the ocean driven by the increasing atmospheric CO_2 levels, rises the concentration of hydrogen ions ($[H^+]$) in seawater which is usually measured in the pH scale ($= - \log10([H^+])$) (Zeebe and Wolf-Gladrow 2001). In other words, due to CO_2 intrusion, seawater becomes more acidic (i.e. pH decreases) because of the perturbed partitioning of the carbonate species (H_2CO_3,HCO_3^-,CO_3^{2-}). The concentration of carbonates (CO_3^{2-}) decreases, leading to a lowering of the saturation state with respect to carbonate minerals (Ω). Seawater pH and Ω are key environmental properties that influence biological processes. Changes in these seawater properties, might threat global biodiversity and ecosystem functioning (Pörtner et al. 2014). For instance, the calcification rates of abundant species of coccolithophores are inhibited owing to increased acidity and reduced Ω (e.g., Meyer and Riebesell 2015). Coccolithophore calcification is an integral part of the ocean carbon cycle and perturbed calcification rates are expected to affect the global carbon budget (e.g., Riebesell et al. 2000; Williamson and Turley 2012). If CO_2 emissions follow the RCP8.5 scenario, it is projected that the global average pH of the surface ocean decreases by 0.3 units by the year 2100 (Figure 3.8a). Further, surface seawater in the Arctic Ocean, that is supersaturated with respect to carbonate minerals ($\Omega > 1$), becomes undersaturated ($\Omega < 1$) by the end of the century (Figure 3.10). The consequences of these environmental changes in marine biota remain unknown (e.g., Williamson and Turley 2012; Bopp et al. 2013; Pörtner et al. 2014).

The effects of SRM in the seawater carbonate chemistry do not lead to any significant differences between this scenario and the reference simulation without CE. Comparing the global average pH of the surface seawater between the scenarios RCP8.5 and SRM2100, pH in the SRM2100 simulation is only ~ 0.02 less acidic than in the reference RCP8.5 simulation. This slightly higher pH is due to the lowering of SST (Figure 3.5) which opposes the effects of the enhanced ocean carbon uptake (Figure 3.2c). Minor regional differences arise between these two simulations over the Arctic Ocean by the end of this century (Figure 3.9). Surface water over

the Arctic Basin becomes less acidified in the SRM2100 simulation compared to the RCP8.5 due to the blocking effect that sea ice exerts on the air-sea CO_2 exchange. In the SRM2100 simulation, the melting of sea ice over this region is largely prevented which lowers the CO_2 intrusion that drives the acidification of seawater. This small mitigation effect on the acidification of the Arctic Ocean, disappears when sea ice melts following the increase in surface atmospheric temperatures as revealed by our SRM2070 scenario.

Seawater temperature affects the solubility of calcium carbonate: increasing temperature lowers the stoichiometric solubility constants of calcite leading to an increase in Ω (Mucci 1983). This temperature effect is rather small, as revealed by the comparison between our SRM scenarios (both SRM2100 and SRM2070) and the RCP8.5 (Figures 3.8b and 3.10). Over the last decades of integration, in the colder climate state of the SRM2100 scenario, global surface seawater Ω is only lower than the value of the RCP8.5 scenario by less than 0.1 unit. This slight difference in the global surface seawater Ω between these two scenarios arises from differences in tropical and temperate oceans. In the SRM2070 scenario, surface seawater Ω is identical to the RCP8.5 because of their similar temperatures.

AOA is often proposed to mitigate detrimental effects of ocean acidification in small scale ecosystems such as coral reefs (e.g., Feng et al. 2016). In a recent field study, it was demonstrated that AOA actually helps the coral reef to increase the net community calcification after seawater carbonate chemistry is returned to pre-industrial conditions (Albright et al. 2016). The controlled addition of alkalinity is required in aquaculture to maintain a chemically stable environment that ensures high growth and survival rates (e.g., Limsuwan 2005; Wurts and Durborow 1992). However, AOA aiming at enhancing the oceanic CO_2 uptake causes surface seawater pH and Ω to rise substantially above modern levels which consequences in marine biota are unknown. In our AOA2100 scenario, surface pH and Ω exceed the levels associated with the targeted (in terms of atmospheric CO_2) RCP4.5 scenario over the whole period of integration. The global average of surface Ω in this AOA2100 scenario, achieves higher levels than the historical period from the year 2050 onwards. During

the last decades of integration, the global surface pH rises substantially above the value of the historical period. The Arctic Ocean and tropical oceans are the most sensitive regions to AOA, owing to a dissimilar rise of the DIC to TA ratio over these basins caused by their particular physicochemical regimes.

The chemical changes brought about by AOA into the surface ocean rapidly vanish after the addition of alkalinity ends. In the AOA2070 scenario, the large-scale global addition of alkalinity stops in the year 2070. This causes that the increasing (global averages) surface seawater pH and Ω drop sharply in the following 5 years (i.e. by 0.1 and 1 units per year for pH and Ω, respectively). This steep decline in pH has the same magnitude than the observed pH decrease since the industrial revolution but it occurs two orders of magnitude faster. The pH and Ω fall rapidly because the buffering capacity of surface seawater rapidly responds to changes in alkalinity. After these abrupt changes in pH and Ω, the effects of seawater acidification occur at a much slower pace and relatively parallel to the trajectory of the RCP8.5 scenario which is defined by the accumulation of CO_2 in the atmosphere. In the AOA2070 scenario by 2100, the alkalinity added prior the time when AOA terminates (~ 45 Pmol) mitigates the decrease in pH by 0.1 units and the Arctic Ocean does not become undersaturated ($\Omega < 1$) as projected under the RCP8.5 (Figures 3.8 and 3.10). Besides, regional heterogeneities caused by the particular responses of the different ocean basins to AOA dissipate. Rapid variations in the seawater physicochemical environment affect biological processes and ecosystem functioning (e.g., Pörtner et al. 2014). This motivates that we explore in more detail (section 3.4.3) the effects on the seawater carbonate chemistry in our terminated CE scenarios.

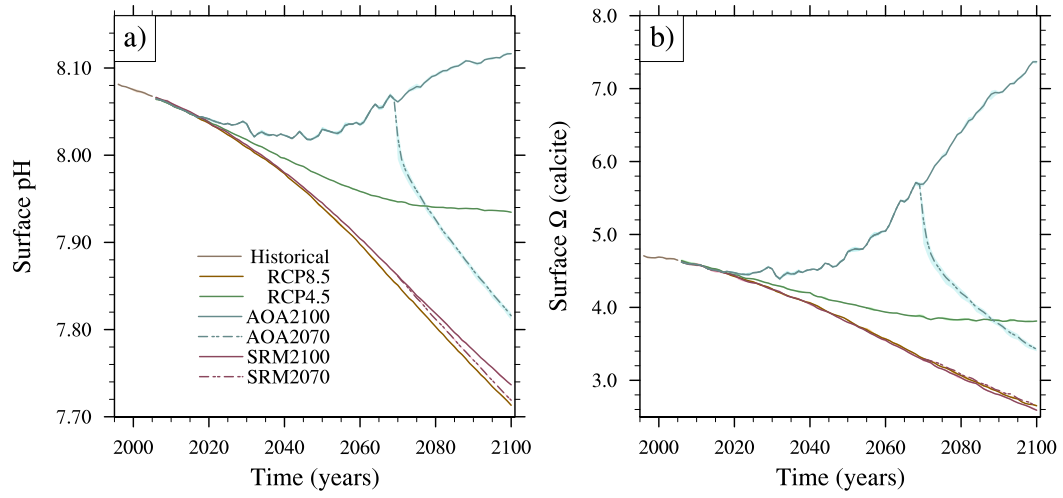Figure 3.8: Temporal evolution of global annual means of surface seawater pH (a) and Ω (b) with respect to calcite in different scenarios. Lines depict 5 year running means under the scenarios Historical (brown), RCP8.5 (orange), RCP4.5 (green), AOA2100 (solid blue), AOA2070 (dashed blue), SRM2100 (solid violet) and SRM2070 (dashed violet). Colored area is model internal variability including three ensemble members.

Figure 3.9: Average annual means (from 1995 to 2005) of surface seawater pH in the Historical simulation (upper map) and the anomalies between this simulation and the last decade of the scenarios (from left to right and top to bottom) RCP8.5, RCP4.5, AOA2100, AOA2070, SRM2100 and SRM2070.

Figure 3.10: Average annual means (from 1995 to 2005) of surface seawater Ω with respect to calcite in the Historical simulation (upper map) and the anomalies between this simulation and the last decade of the scenarios (from left to right and top to bottom) RCP8.5, RCP4.5, AOA2100, AOA2070, SRM2100 and SRM2070.

3.3.4 Marine Net Primary Production

Global warming affects marine biota by changing their physical environment. The mixed layer depth (MLD) shallows with rising surface seawater temperatures (Figure 3.6). This enhanced stratification of the water column due to warming, reduces the vertical entrainment of limiting nutrients into the euphotic zone which leads to the decline in marine net primary production (NPP) (Behrenfeld et al. 2006; Bopp et al. 2013). Under the high emissions scenario RCP8.5, the MPI-ESM projects that the global NPP decreases over the course of the 21st century to $\sim$80% of its current value (i.e. from 60 to 50 PgC/yr) (Figure 3.11). The mitigated warming in the AOA and SRM scenarios with CE until 2100, reduces the enhanced stratification of the water column, thereby the decline in global NPP. In both the AOA2100 and SRM2100 scenarios, the temporal evolution of global NPP paralelly follows the targeted (only in terms of atmospheric CO_2) RCP4.5 scenario. However, trends are difficult to distinguish because of the large internal model variability in this parameter. Regional changes in NPP (Figure 3.12) reveal that spatial patterns are largely conserved and that the magnitude of change increases with warming. NPP increases over the Arctic Ocean because the retreat of sea ice exposes nutrient-rich waters to light which enhances carbon fixation by phytoplankton. Primary production is also boosted in large regions of the Southern Ocean due to a reduction in light limitation. The shallowing of the MLD induced by the increasing temperatures after termination of CE in 2070 (in both AOA and SRM), leads to spatial patterns and global averages of NPP that are similar to those of the reference RCP8.5 scenario by 2100.
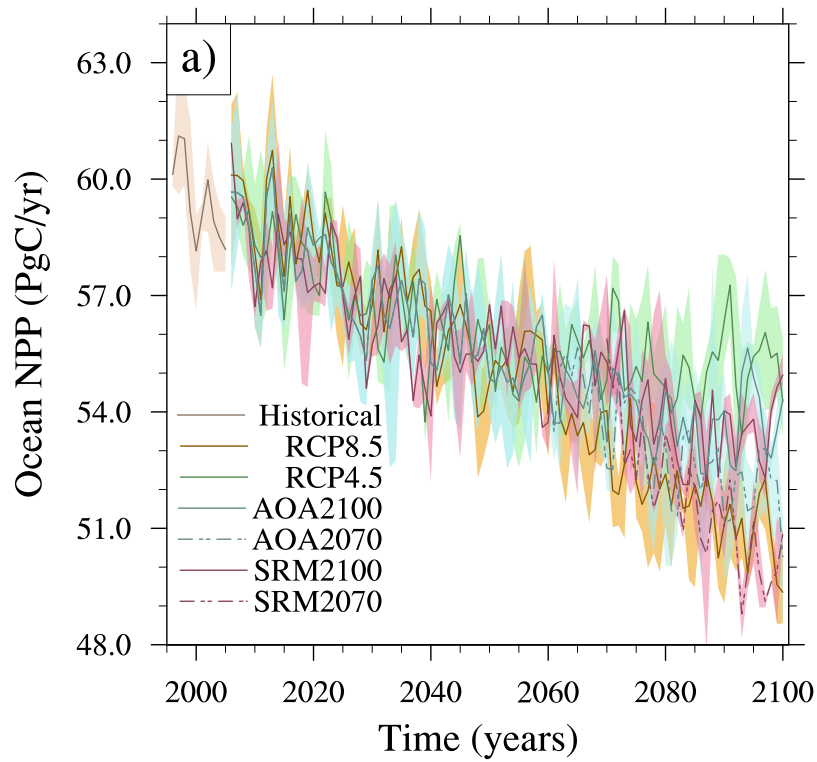
Figure 3.11: Temporal evolution of global annual means of ocean net primary production (NPP) vertically integrated (PgC/yr) in different scenarios. Lines depict 5 year running means under the scenarios Historical (brown), RCP8.5 (orange), RCP4.5 (green), AOA2100 (solid blue), AOA2070 (dashed blue), SRM2100 (solid violet) and SRM2070 (dashed violet). Colored area is model internal variability including three ensemble members.
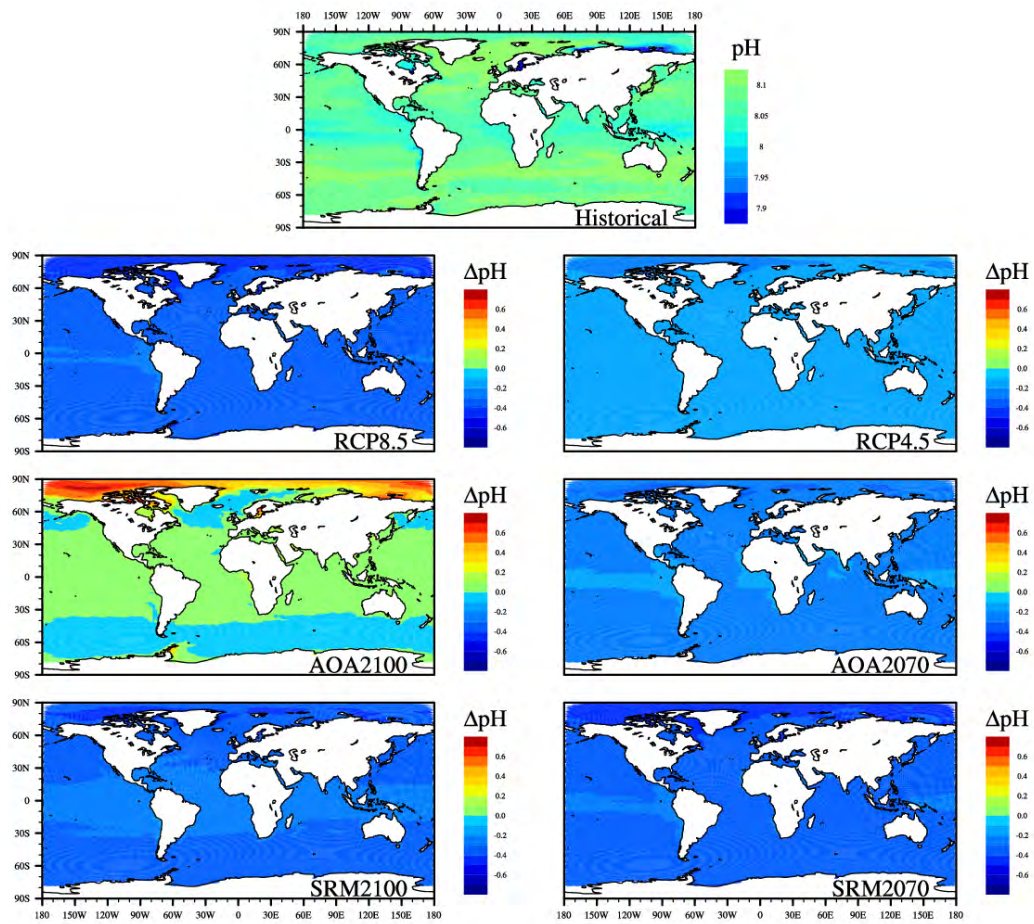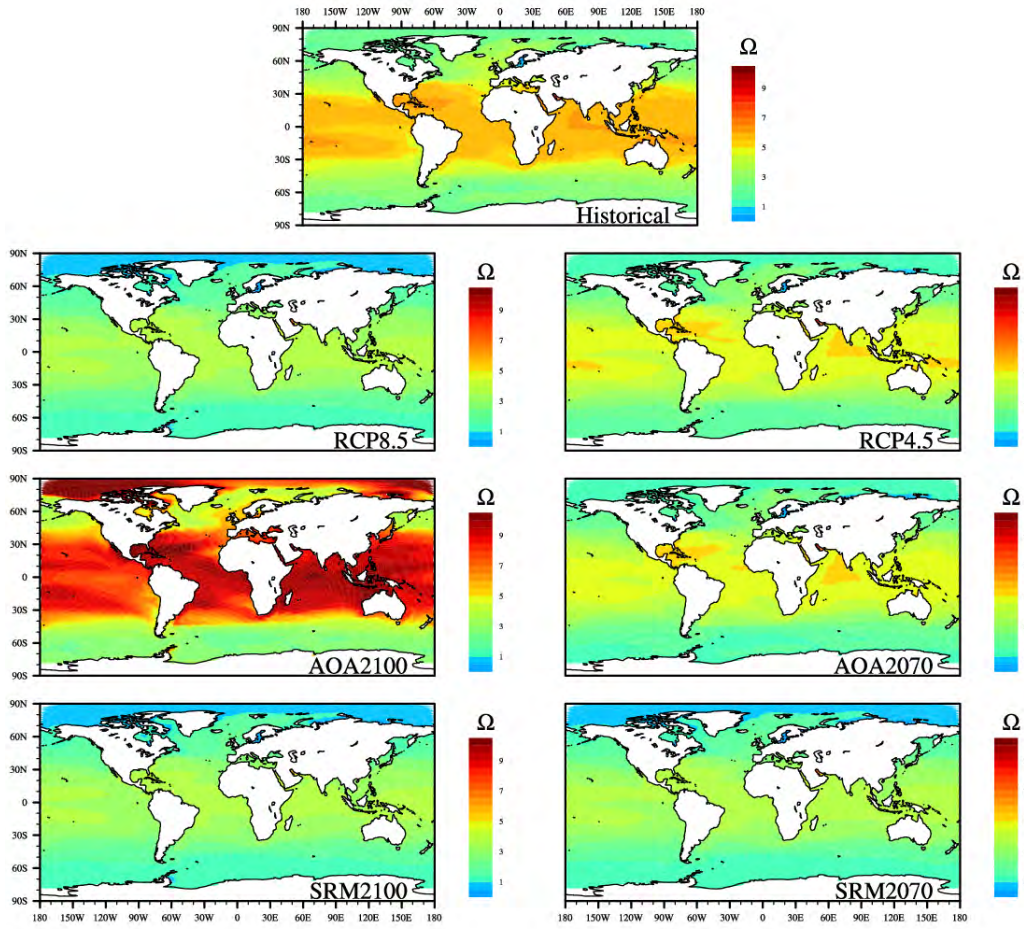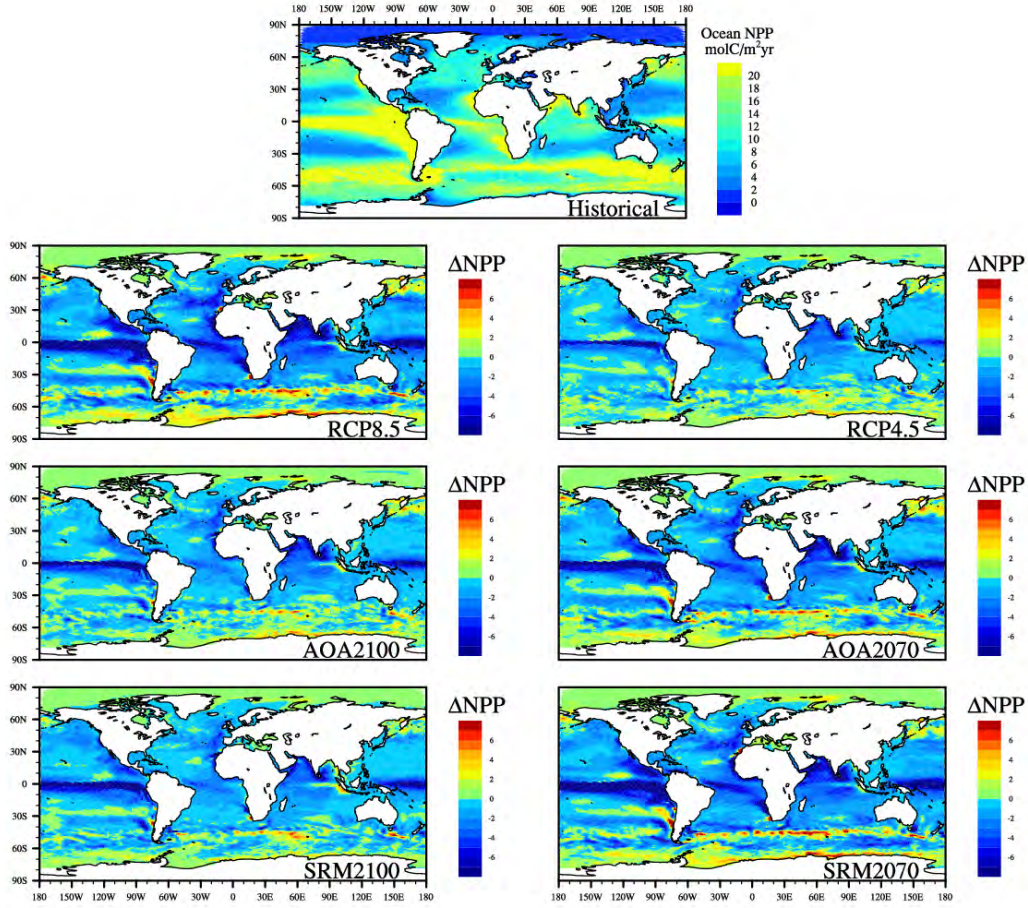
Figure 3.12: Average annual means (from 1995 to 2005) of ocean net primary production (NPP) vertically integrated (molC/m^{2}yr) in the Historical simulation (upper map) and the anomalies between this simulation and the last decade of the scenarios (from left to right and top to bottom) RCP8.5, RCP4.5, AOA2100, AOA2070, SRM2100 and SRM2070.

3.4 Effects on the Rates of Change

3.4.1 Surface Temperature

Rapid warming and its concomitant effects on the natural environment (e.g. in precipitation and sea ice cover), reduce the adaptive capacity of ecological and human systems to climate change (Pörtner et al. 2014). That is why, there are many concerns about the consequences for the Earth's climate in case of failure or abrupt termination of SRM (e.g., National Research Council 2015a,b; IPCC 2012). Previous studies have found that the sudden termination of SRM leads to faster rates of global warming than those of the climate change scenario intended to alleviate (e.g., Brovkin et al. 2009; Jones et al. 2013). Rapid changes in radiative forcing upon abrupt cessation of large-scale CDR scenarios or, equivalently, an intense leakage of CO_2 in carbon capture and storage facilities, might also induce an accelerated warming (e.g., Stone et al. 2009; Lenzen 2011).

In our terminated SRM simulation, in agreement with previous estimates (e.g., Jones et al. 2013), local warming rates are largely enhanced during the following years after cessation of SRM in 2070 (Figures 3.13 and 3.14). Jones et al. (2013) found that the absolute rates of regional warming are mainly determined by the compensated radiative forcing of GHGs by the time of SRM termination: the higher the prevented warming by the time of termination, the faster the warming trend. Comparing the SRM2070 scenario with the reference RCP8.5, regional warming patterns are in general similar. However, small regional differences between the SRM2070 and RCP8.5 scenarios arise due their different background states of the regional climate at the time of termination. Besides, some areas at high latitudes of the Northern hemisphere in the SRM2070 scenario, reach values even one order of magnitude higher than those projected under the RCP8.5 (up to 0.14 K/yr in atmospheric temperatures) owing to polar amplification.

Figure 3.13: The left column shows the linear trends of the annual mean near-surface atmospheric temperature during the period between the years 2070 and 2100 under the scenarios (from top to bottom) RCP8.5, RCP4.5, AOA2100, AOA2070, SRM2100 and SRM2070. The right column shows the model internal variability (expressed as one standard deviation among the three ensemble members) of the map located on its left side.

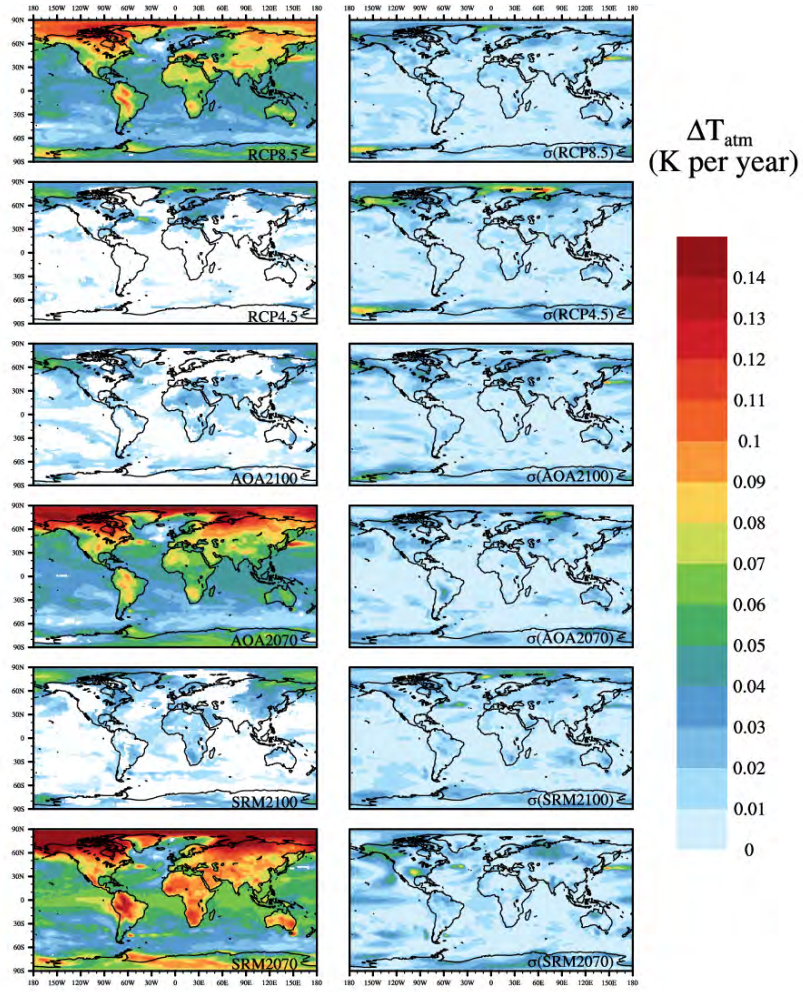Figure 3.14: The left column shows the linear trends of the annual mean sea surface temperature (SST) during the period between the years 2070 and 2100 under the scenarios (from top to bottom) RCP8.5, RCP4.5, AOA2100, AOA2070, SRM2100 and SRM2070. The right column shows the model internal variability (expressed as one standard deviation among the three ensemble members) of the map located on its left side.
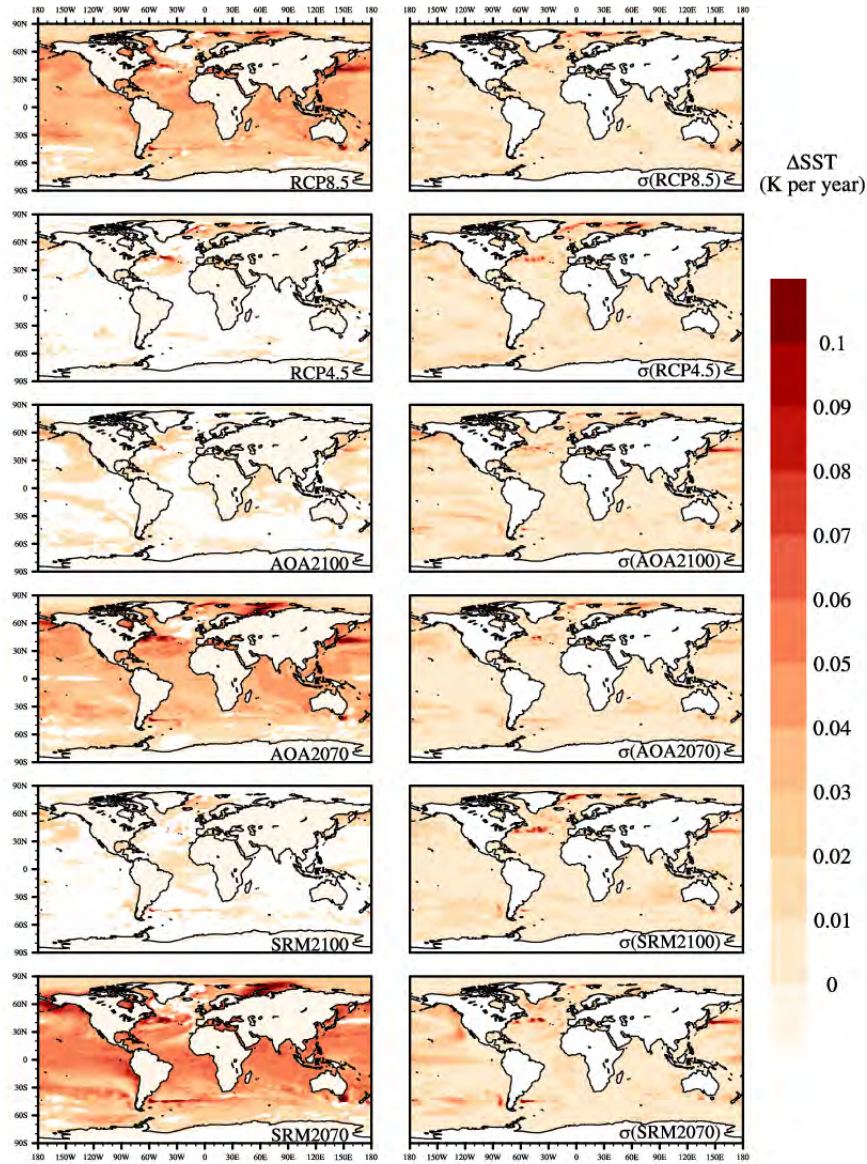
Unlike the termination effects of SRM, the impact of rapid changes in forcing due to CDR methods receives less attention. This is mainly because the warming following rapid changes in radiative forcing caused by CDR methods is expected to be less severe than the one associated with SRM and somehow similar to the scenario without CDR. Overall, this is what we obtain in our AOA2070 scenario. The changes in atmospheric forcing after termination of large-scale AOA in 2070, lead to a global warming rate that evolves parallel to the trajectory of the RCP8.5 scenario ($\sim$0.05K/yr between the period from 2070 to 2100), which is mainly defined by the rate at which CO_2 accumulates in the atmosphere (Figure 3.2a and b). However, differences in regional rates of warming appear when comparing the spatial patterns of rising surface temperatures between the AOA2070 and RCP8.5 scenarios. Namely, regional rates of surface atmospheric warming in the AOA2070 scenario exceed those of the RCP8.5, reaching up to 0.1 K per year at high latitudes over northern Europe, the North Atlantic Ocean and the Kara and Barents Seas. These small regions at high latitudes of the Northern hemisphere in the AOA2070 simulation, present similar warming rates than those of the terminated SRM scenario despite of the different atmospheric forcings that are modified by these methods. The local internal variability of surface warming in the atmosphere and surface seawater changes with forcing and due to differences in the regional background states (Figures 3.13 and 3.14). The ensemble spread (here considered with one standard deviation among three ensemble members), achieves values as large as the warming trend. High latitudes of the Northern hemisphere present, in general, larger local internal variability of warming compared with other regions.

It is unknown how ecological and human systems might respond to environmental changes of this pace and magnitude. Many uncertainties arise because of the high complexity involved, their resilience to perturbations and their adaptation capacity (e.g., Williamson and Turley 2012; Pörtner et al. 2014). Quintero and Wiens (2013) have estimated that major groups of vertebrates will need rates of niche evolution 4 orders of magnitude higher than those generally surveyed in order to adapt to the projected rates of change by 2100 in a high CO_2 emissions scenario. Thus, the

accelerating effects of CE termination - in both CDR and SRM approaches - might further limit their adaptation capacity.

3.4.2 Ocean Carbon Uptake

Increasing atmospheric CO_2 levels, enhance the air-sea CO_2 gradient which affects spatial patterns of carbon exchange. Under the RCP8.5 scenario, the MPI-ESM projects the strengthening over time of the local CO_2 uptake (i.e. positive local trend of the flux) during the last decades of this century in large regions of the Southern Ocean (Figure 3.15). At latitudes higher than 60° South, the uptake of carbon over time increases at an average rate of 1.2 gC/m^2y^2 over large regions. In contrast, during the same period and scenario, the MPI-ESM projects the weakening over time (i.e. negative trend) of the local carbon uptake at high latitudes of the North Atlantic. Specifically, the uptake of carbon decreases over time at an average rate of approx. -0.7 gC/m^2y^2 over large regions of the North Atlantic subpolar gyre. Comparing the regional trends of CO_2 flux between the RCP8.5 and SRM2100 scenarios during the last decades of the simulated period, the projected weakening with time of the CO_2 uptake over the North Atlantic subpolar gyre vanishes. This is due to effect of the colder (than RCP8.5) temperatures in the SRM2100 scenario on the local carbon fluxes over this region. Comparing the trends of CO_2 flux between the RCP8.5 and SRM2070 scenarios during the last decades of this century, the differences between these scenarios are negligible due to their similar climate states.
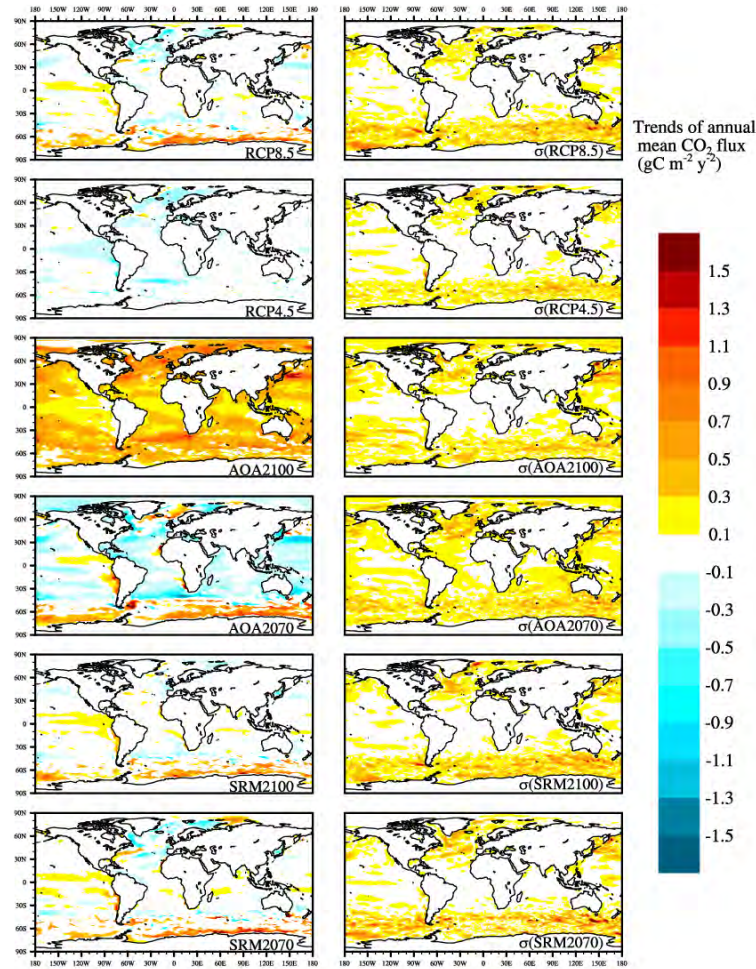
Figure 3.15: The left column shows linear trends of CO_2 flux (i.e. variation over time of the magnitude of the flux) during the period between the years 2070 and 2100 under the scenarios (from top to bottom) RCP8.5, RCP4.5, AOA2100, AOA2070, SRM2100 and SRM2070. A positive trend means that the magnitude of the carbon flux increases over time, whilst a negative trend indicates a carbon flux that weakens over time. Please note that these trends do not represent the sign of the flux, i.e. whether there is local carbon uptake or release. The right column shows the model internal variability (expressed as one standard deviation among the three ensemble members) of the map located on its left side.

In our large-scale AOA2100 scenario, the global ocean turns into a carbon sink and large positive trends of CO_2 flux emerge everywhere during the last decades of this century. In other words, the uptake of carbon with time increases over the entire ocean. These positive trends are higher at high latitudes of the Northern hemisphere, they reach up to 1.5 gC/m^2y^2 along the latitudinal band at 70° North. Regarding the regional trends of CO_2 flux in the AOA2070 scenario, they overall follow a similar spatial pattern to the one associated with the reference RCP8.5. However, the magnitudes of the trends largely intensify owing to the changes in the surface seawater DIC content brought about by the addition of TA in the AOA2070 scenario. This is especially pronounced over tropical and temperate oceans, where local negative trends become as low as -1.5 gC/m^2y^2. The internal variability in the local trends of CO_2 flux is inhomogeneous over the ocean but conserved between the different simulations. In general, high latitude regions in both hemispheres show larger values of internal variability than tropical oceans.

3.4.3 Seawater Carbonate Chemistry

AOA causes rapid variations in the seawater chemical environment which effects on the marine biology are unknown. Rapid variations in surface CO_3^{2-} occur in the alkalinized water, when the rate of increase in TA exceeds the rate of increase in DIC (Figure 3.16). Surface seawater Ω also rises because it is proportional to the concentration of CO_3^{2-} (Figure 3.19). The added bases during AOA consume protons that unbalance the partitioning of the carbonate species increasing the concentration of CO_3^{2-}. The seawater carbonate system re-equilibrates through the enhanced uptake of CO_2, namely adding a strong acid that increases the concentration of protons and the DIC content. However, this is limited by the available volume of water. In the open ocean, differences in the rates of change between TA and DIC are mainly driven by the pace at which the strong bases are added into the surface seawater during AOA and the rate at which the carbonate system returns to equilibrium. In shallow oceans where vertical mixing is constrained by thermal stratification, the

enhanced uptake of CO_2 following AOA, may not compensate the disequilibrium in the partitioning of the carbonate species leading to rapid variations in CO_3^{2-} and Ω. This effect causes large regional differences in the pace at which seawater CO_3^{2-} and Ω vary in our AOA2100 scenario despite the globally homogeneous distribution of TA. The tropical oceans and the Arctic Ocean present much larger rates of change than those of the rest of the oceans (up to ~ 0.07 units per year), and these decreasing regional trends are one order of magnitude larger than those projected in the RCP8.5 scenario. This is because both the Arctic Ocean and the tropical oceans, are highly stratified (Figure 3.6).

Regional trends in pH in the AOA2100 scenario (Figure 3.17) show that the surface seawater pH increases over time at an average rate of 0.002 units per year between the period from 2070 to 2100. Regarding surface seawater pCO2 in this scenario (Figure 3.18), local levels of pCO2 slightly decrease at an average rate of -1 ppm per year between the same period. Over the Arctic Ocean, the effect of sea ice on the DIC to TA ratio of seawater alters the variation of surface pH and pCO2 over time. This is mainly an effect of our scenario design in which TA is also added over areas covered by sea ice and the ice cover blocks the air-sea CO_2 exchange such that the seawater carbonate system cannot equilibrate. In the AOA2070 scenario during the last three decades of the simulated century, most of the ocean acidifies much faster than in the RCP8.5. Right after termination of AOA, regional rates of change in surface pH, pCO2 and Ω become regionally up to one order of magnitude higher than those in RCP8.5 over large regions in the Arctic Ocean and tropical oceans. In contrast, differences in the regional trends of surface seawater pH, pCO2 and Ω between the SRM2100, SRM2070 and RCP8.5 scenarios are negligible.
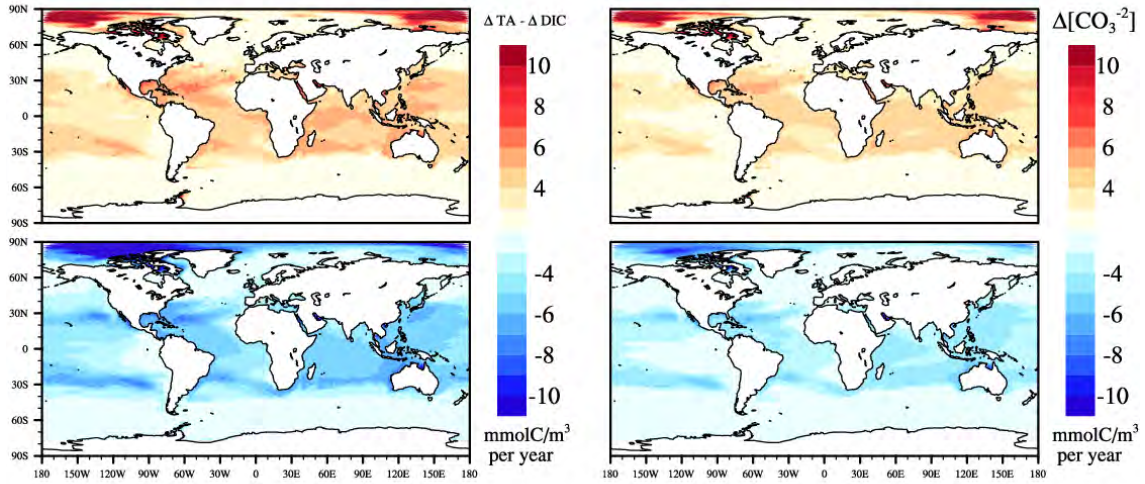
Figure 3.16: The first column shows the differences between the rates of change in total alkalinity (TA) and dissolved inorganic carbon (DIC) in surface seawater (mmolC/m^{3}yr). The second column shows the rates of change in the concentration of surface seawater CO_3^{2-} (mmolC/m^{3}yr). First row are the results of the AOA2100 scenario and second row are the results of the AOA2070.

Organisms are sensitive to the rate of environmental change (e.g., Pörtner et al. 2014). Actually, some organisms are more sensitive to the rate of change rather than its magnitude. For instance, the coralline algae *Lithothamnion glaciale* exposed to a fast drop in pH suffers structural damages (Kamenos et al. 2013). However, the same decrease in pH occurring at a slower pace, does not cause any harm. AOA has been proposed to reduce the detrimental effects of ocean acidification in coral reefs (e.g., Feng et al. 2016), and a recent field study suggests that this method might actually alleviate the observed decrease in the net community calcification of coral reefs when seawater acidifies (Albright et al. 2016). Whilst it is already known that individual keystone species within the coral reefs will be negatively affected by rapid changes in the seawater chemical environment, the response of the

whole ecosystem to fast-paced changes in their environment caused by termination of AOA remains unexplored. Rapid variations in the chemical environment might be detrimental for marine biology. This has been already observed in aquaculture practices in which the environmental conditions need to be maintained stable in order to ensure high growth and survival rates (e.g., Limsuwan 2005; Wurts and Durborow 1992). Moreover, rapid changes in the seawater carbonate chemistry due to termination of AOA might interfere with biological processes. The rate of change in the environmental conditions has been identified as cue for key transitions in reproductive cycles in marine species (e.g., Fiorillo et al. 2013; Cornish and Smit 1995). For example, the onset of the reproductive cycle of the fish *Mozambique tilapia* has been found to be triggered by the combination of decreasing pH with increasing rainfall, photoperiod and water temperature (Cornish and Smit 1995).

Figure 3.17: Linear trends of surface seawater pH during the period between the years 2070 and 2100 under the scenarios (from left to right and top to bottom) RCP8.5, RCP4.5, SRM2100, SRM2070, AOA2100 and AOA2070.

Figure 3.18: Linear trends of surface seawater pCO2 during the period between the years 2070 and 2100 under the scenarios (from left to right and top to bottom) RCP8.5, RCP4.5, SRM2100, SRM2070, AOA2100 and AOA2070.
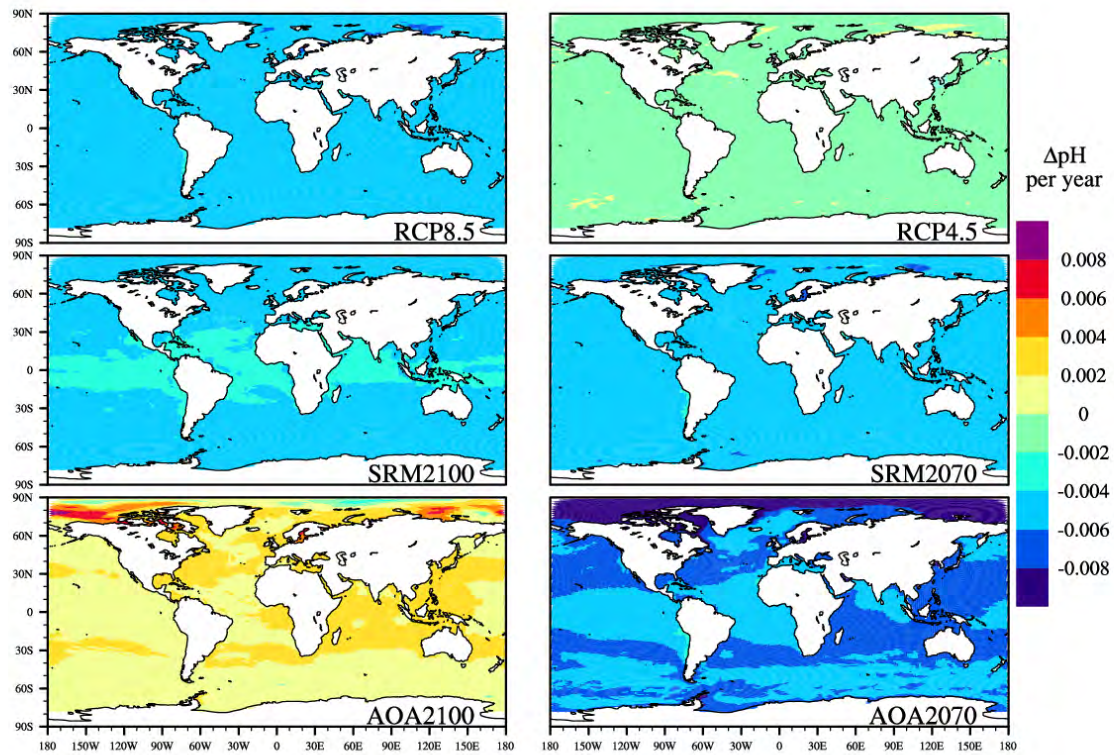
Figure 3.19: Linear trends of surface seawater Ω (calcite) during the period between the years 2070 and 2100 under the scenarios (from left to right and top to bottom) RCP8.5, RCP4.5, SRM2100, SRM2070, AOA2100 and AOA2070.
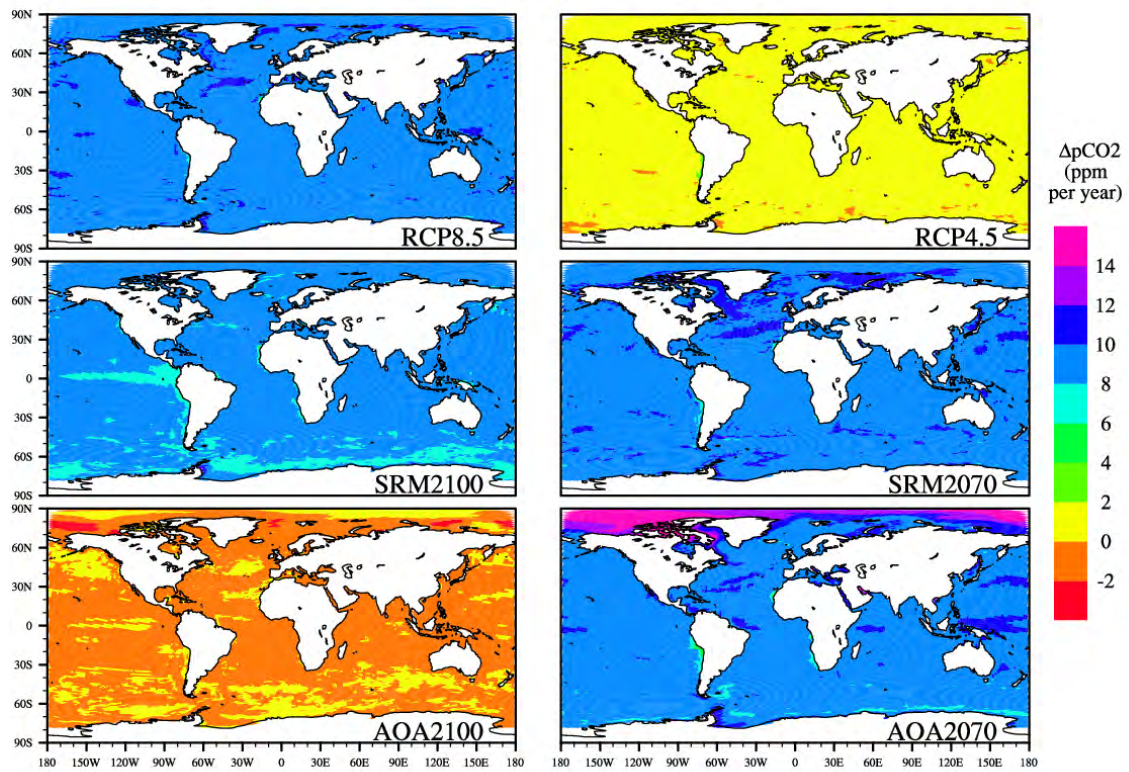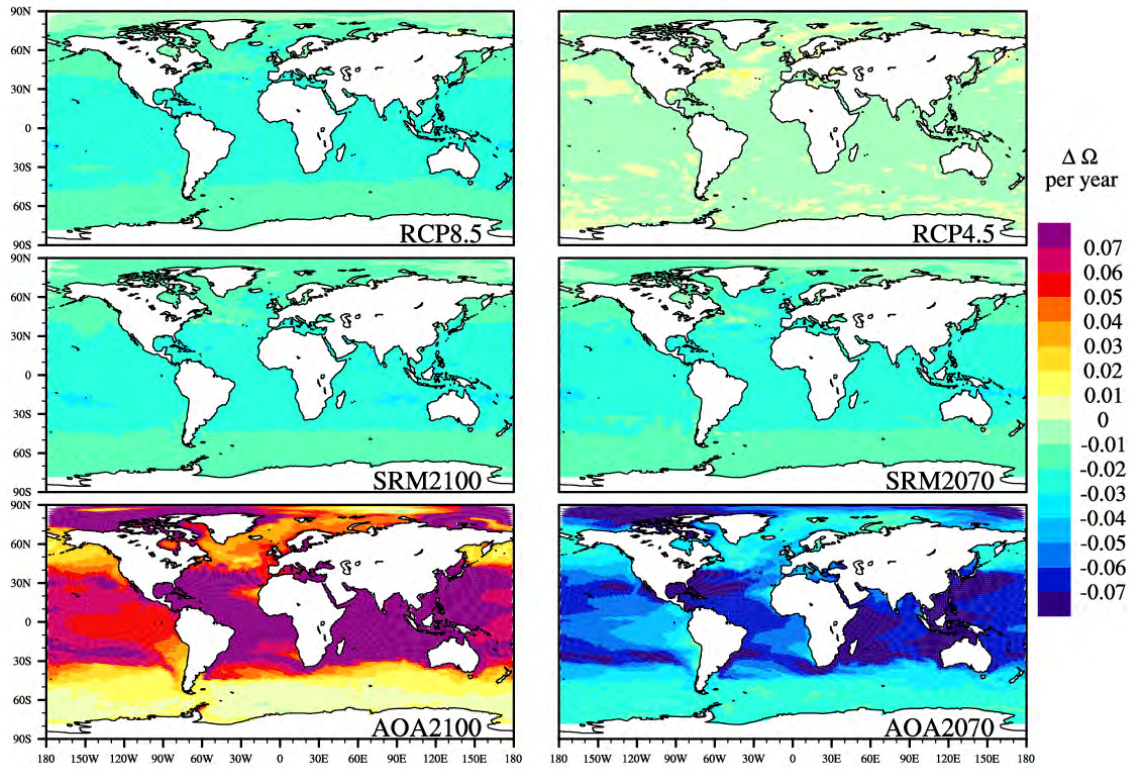
94

3.4.4 Marine Net Primary Production

Global warming changes the seawater physical environment which impacts the nutrients regime and marine NPP. The increasing temperatures enhance the stratification of the water column (Figure 3.6). For instance, the MPI-ESM projects that the average annual mean of the MLD is reduced by 20 meters over large regions of the Southern Ocean by 2100 in the reference RCP8.5 relative to values at the beginning of this century as simulated in the Historical experiment. The shallowing of the MLD reduces the vertical entrainment of nutrients into the euphotic zone which leads to an overall decline in NPP. Under the RCP8.5 scenario, the MPI-ESM projects that global ocean net primary production is reduced by 10 PgC/yr relative to the estimated levels of the modern ocean (Figure 3.11). In contrast to the overall shallowing of the MLD, in the Arctic Ocean the MLD deepens (by $\sim$5 meters in most of our simulations), which enhances vertical mixing and thereby nutrient availability. Moreover, over these regions the retreat of sea ice due to warming, exposes surface seawater to light which is also expected to enhance NPP. Negative local trends of NPP emerge in the RCP8.5 over most of the tropical and subtropical oceans (as low as -0.05 molC/m^{2}yr^2) during the last decades of the simulated period due to the shallowing of the MLD (Figure 3.20). These local changes are largely reduced in our AOA2100 and SRM2100 scenarios due to the prevented warming, which leads to values of the MLD similar to those of the targeted RCP4.5 scenario and thereby similar local trends of NPP. Regarding the terminated CE scenarios, the local rates of variation in NPP under the AOA2070 scenario during the last decades of this century, are similar to those associated with the reference RCP8.5 due to their similar regional warming rates over most of the ocean (Figure 3.14). In contrast, comparing the terminated SRM scenario and the RCP8.5, the total area of the tropical and subtropical oceans where local trends of decreasing NPP reach values as low as -0.05 molC/m^{2}yr^2 during the last decades of this century doubles. Besides, the decreasing trends in NPP in the SRM2070 experiment during the last decades of this century become one order of magnitude higher (than RCP8.5) over most of the tropical oceans due to the rapid response of the MLD to surface warm-

ing. However, these projected trends in the scenarios occur in a background of large model internal variability of NPP (here considered as one standard deviation among the ensemble members), which varies locally with forcing and achieves levels as large as the NPP trends. The tropical Pacific and the Southern Ocean show the largest values of model internal variability of NPP compared with other regions. Thus, the surface seawater environment changes rapidly due to the termination of large-scale AOA and SRM scenarios. How biological systems might cope with rapid variations in their environmental conditions is currently unknown. Previous studies suggest that rapid perturbations are generally unfavorable, specially due to the additional pressure caused the simultaneous exposure to multiple stressors (e.g., Bopp et al. 2013).

96
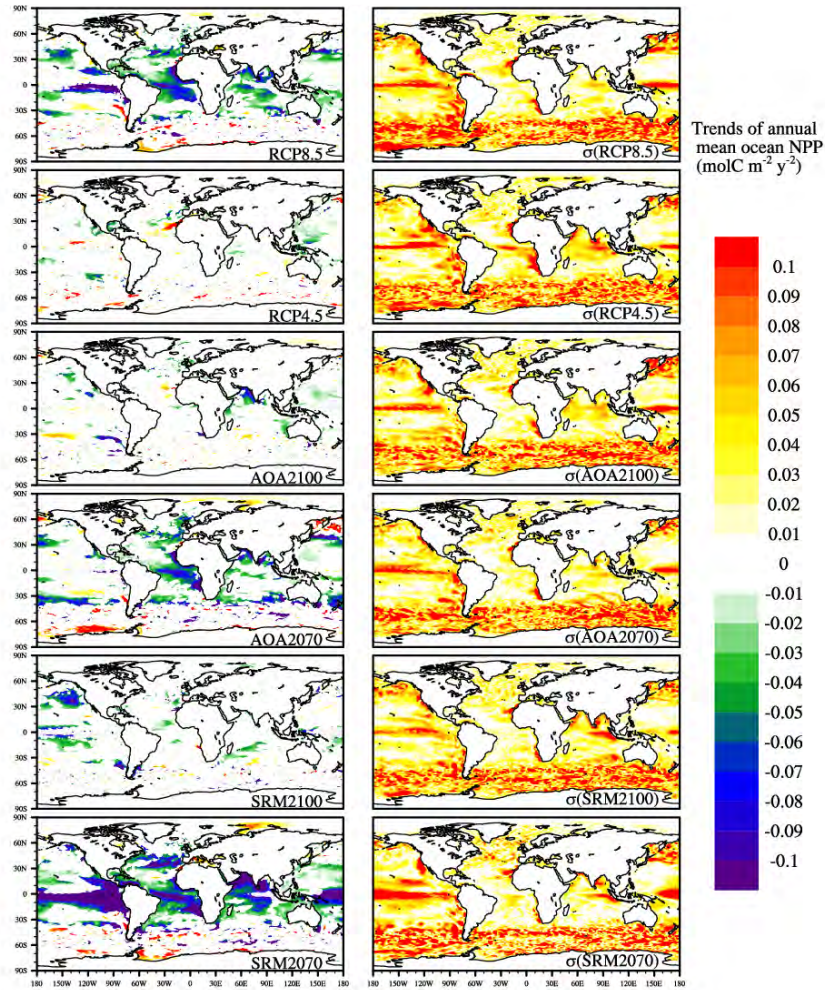
Figure 3.20: The left column shows the linear trends of ocean net primary production (NPP) vertically integrated (molC/m^{2}y^2) during the period between the years 2070 and 2100 under the scenarios (from top to bottom) RCP8.5, RCP4.5, AOA2100, AOA2070, SRM2100 and SRM2070. The right column shows the model internal variability (expressed as one standard deviation among the three ensemble members) of the map located on its left side.

3.5 Effects on the Seasonal Cycle

3.5.1 Surface Temperature

The range and timing of the annual fluctuation of surface atmospheric temperature under global warming projections, differ from those of the current climate state (e.g., Mann and Park 1996; Stine and Huybers 2012). This perturbed seasonal cycle of the surface temperature shows a specific latitudinal pattern (Dwyer et al. 2012). Over high latitudes, the range of values between the maximum and minimum temperatures throughout the year (seasonal amplitude) decreases. This damping of the seasonal amplitude is more pronounced over oceanic regions at high latitudes of the Northern hemisphere. Over large regions at low latitudes, the seasonal amplitude increases and the magnitude of this perturbation varies zonally. Besides, a phase delay in this annual temperature fluctuation over the whole globe co-occurs with these changes in the amplitude. This disturbance of the seasonal cycle under climate change projections appears as a robust feature of climate models (e.g., Dwyer 2014), and early signals of this perturbation have been already documented in field studies over the Arctic Ocean (e.g., Bintanja and van der Linden 2013).

In line with previous modeling studies, our climate change scenarios (RCP4.5 and RCP8.5) show changes in the seasonal amplitude of surface atmospheric temperature. We quantify the local changes in the seasonal amplitude by the ratio of the average seasonal amplitude at the end of the 21st century in our experiments, to the average seasonal amplitude as simulated during the historical period (Figure 3.21). We refer to this ratio as *amplification factor* (AF, equation 3.1). The RCP4.5 scenario shows the smallest seasonal perturbation in surface atmospheric temperatures of all the experiments (Figure 3.22), with local AF values ranging from 0.8 to 1.2 (i.e. damping/broadening of the seasonal amplitude up to values around 20% lower/higher than the average value during the historical period). The RCP8.5 scenario presents the strongest damping over high latitudes of the Northern hemisphere and the highest amplification over regions at lower latitudes (than 60° in both hemi-

spheres) compared to all the scenarios. Besides, the RCP8.5 shows the greater AF declining gradient from 35° to 65° South and between 45° North and northwards, achieving a reduction in the projected seasonal amplitude up to half of its current value (i.e. AF = 0.5) in some regions between 80° and 90° North. Regions covered by the Antarctic continent (>75° South), do not show variations in the seasonal amplitude of surface atmospheric temperature.
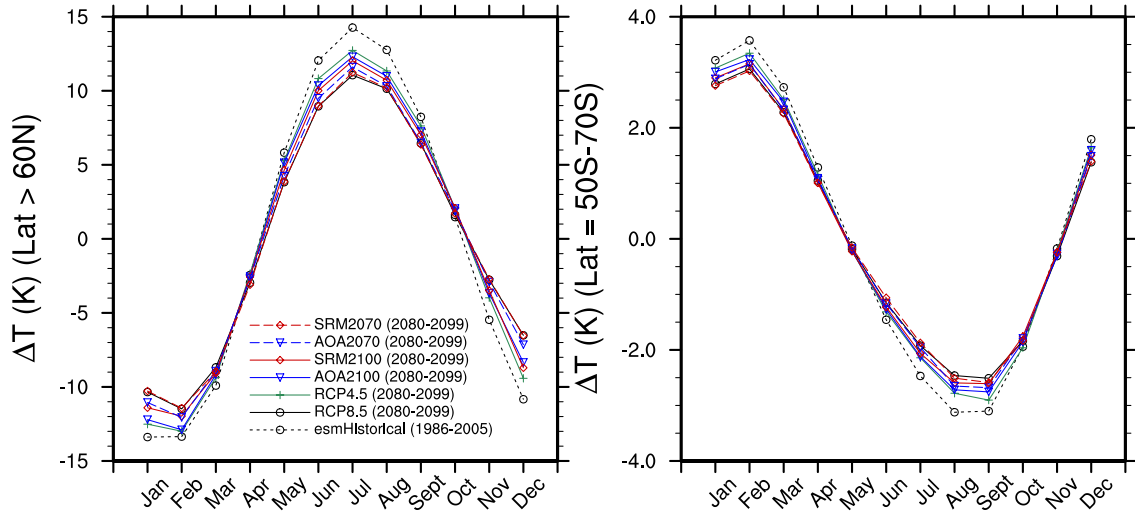
Figure 3.21: Averaged monthly deviation from the annual mean of near-surface atmospheric temperature during the last two decades of the 21st century in the scenarios: RCP8.5 (solid line black), RCP4.5 (solid green), and the CE scenarios AOA and SRM until 2100 (blue and red solid lines, respectively) and until 2070 (blue and red dashed lines, respectively). The dashed black line shows the monthly deviation from the annual mean of the near-surface atmospheric temperature as simulated in the historical period and averaged over the years from 1986 to 2005.

The perturbed seasonal cycle characterized by surface atmospheric temperatures in the reference scenario RCP8.5, is changed by our CE experiments. The CE experiments AOA2100 and SRM2100, show similar results when compared with each other. Both simulations bring the perturbed seasonal amplitude to values close to those of the RCP4.5, but still slightly lower (i.e. stronger damping) than in the RCP4.5 at high latitude regions. Differences between the AOA2100 and SRM2100 scenarios and the targeted RCP4.5, are due to higher global annual temperatures of the AOA2100 and SRM2100 scenarios compared to the RCP4.5 (Figure 3.2b). This is because, the magnitude of the perturbation in the seasonal amplitude of surface atmospheric temperature scales linearly with the degree of global warming and so that the higher the warming the stronger the regional damping/amplification of the amplitude. The terminated CE simulations AOA2070 and SRM2070, have average seasonal amplitudes by 2100 that are similar to those associated with the RCP8.5 scenario.

At high latitudes, the decreasing sea ice area is the dominant driver of the damped seasonal amplitude (Dwyer et al. 2012). The retreating sea ice exposes a greater surface of ocean to the atmosphere, increasing the effective heat capacity of the surface layer which leads to a weakened atmospheric temperature cycle. Thus, scenarios with similar sea ice cover (Figure 3.3) present perturbed seasonal cycles of surface atmospheric temperature that are alike. Furthermore, the decrease in sea ice cover causes that the seasonal amplitude of SST over polar regions is enhanced due the increasing surface of seawater that is exposed to the atmosphere (Figure 3.23). At low and mid latitudes, the dominant driver of the perturbed seasonality is still unclear, but it has been associated with an amplified seasonal amplitude of surface wind speed via changes in surface latent heat fluxes. The changes in seasonality of wind speed has been related to changes in the tropical circulation, particularly due to the poleward expansion and weakening in the strength of the Hadley Cell (Sobel and Camargo 2011). Changes in the annual amplitude of surface wind speed affect the annual amplitude of surface temperature through variations in surface latent heat fluxes. However, the relation between wind speed and temperature affecting

the surface latent heat flux is complicated because multiple parameters of this flux change in parallel (Dwyer 2014). In addition, the total surface heat flux is also defined by different terms than the latent heat flux within seasonal timescales.
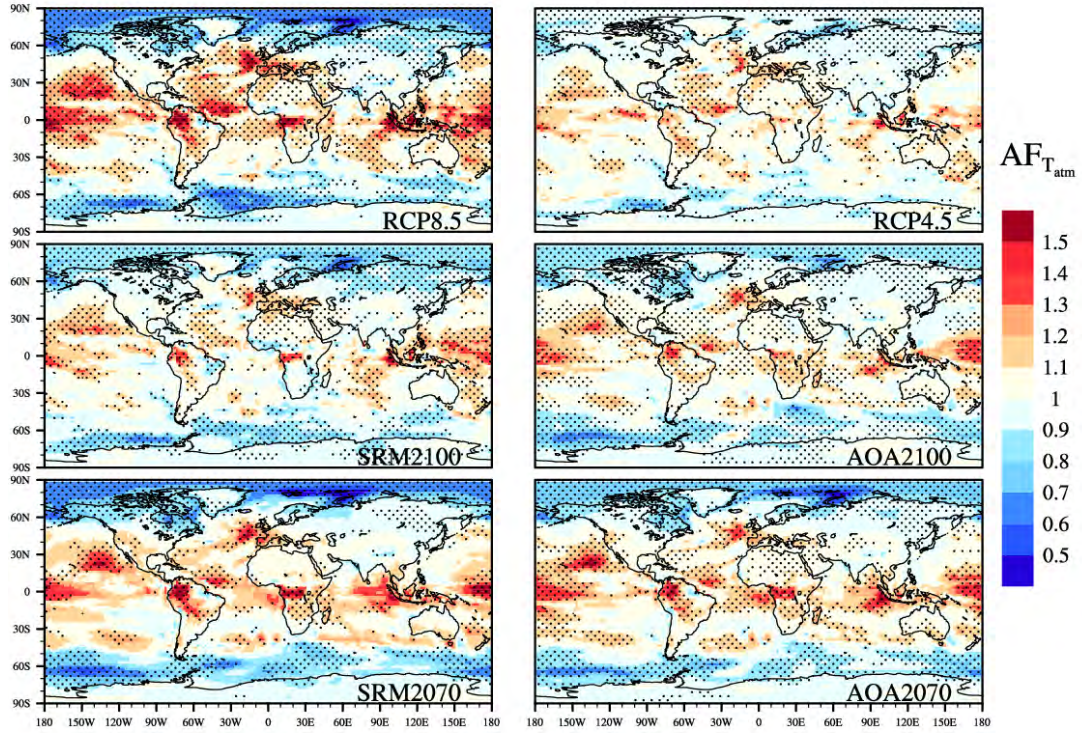
Figure 3.22: Maps of the amplification factors (AF) of near-surface atmospheric temperature under the RCP8.5 and RCP4.5 climate change scenarios (top left and right), and the CE scenarios continuously implemented until 2100 (SRM2100 and AOA2100, middle left and right) and terminated in 2070 (SRM2070 and AOA2070, bottom left and right). The stippled regions indicate statistically significant differences in the seasonal amplitudes at the 95% confidence level.
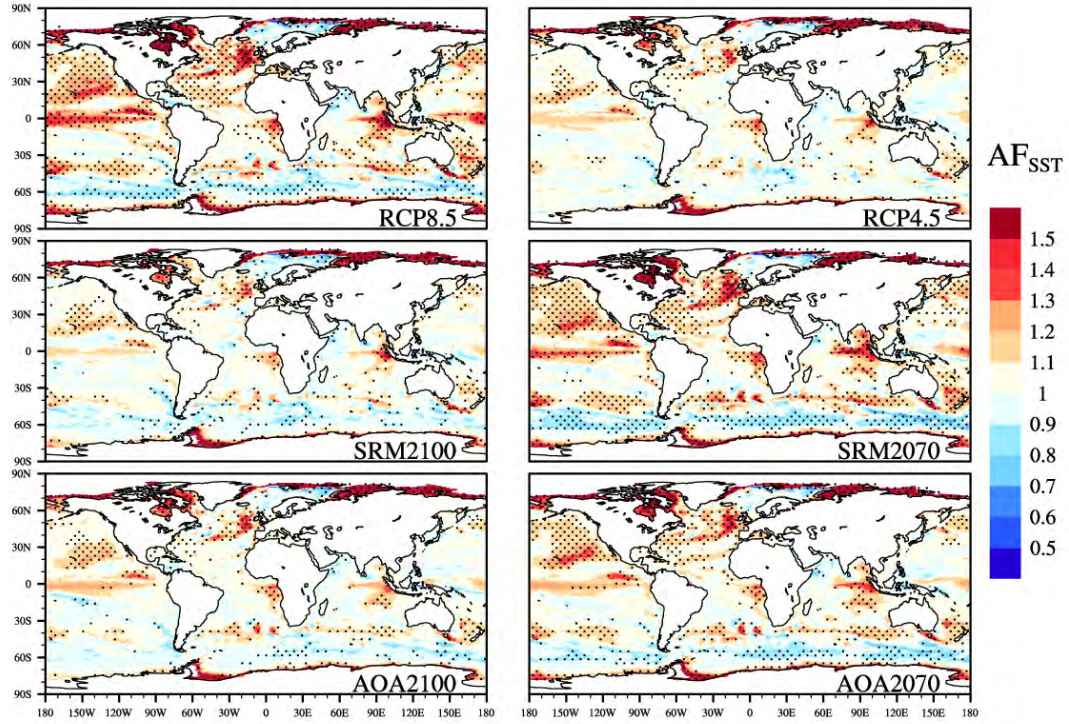
Figure 3.23: Maps of the amplification factors (AF) of surface seawater temperature (SST) under the RCP8.5 and RCP4.5 climate change scenarios (top left and right), and the CE scenarios continuously implemented until 2100 (SRM2100 and AOA2100, middle left and right) and terminated in 2070 (SRM2070 and AOA2070, bottom left and right). The stippled regions indicate statistically significant differences in the seasonal amplitudes at the 95% confidence level. Values in which the sea ice cover maintains a constant range of SST throughout the year in the Historical simulation have been excluded.

3.5.2 Ocean Carbon Uptake

The seasonal cycle of air-sea CO_2 exchange is expected to vary due to the changes in the seawater buffering capacity, surface temperatures, sea ice cover and biological pCO2 drawdown. The enhanced ocean CO_2 sink lowers the seawater buffering capacity (Zeebe and Wolf-Gladrow 2001) what will eventually limit the carbon uptake by the ocean (W.R.Wallace 2001). This reduction in the buffering capacity also causes that CO_2 in seawater becomes more sensitive to changes in DIC, which is expected to intensify seasonal CO_2 fluxes (e.g., Hauck and Völker 2015). Higher surface temperatures reduce the sea ice cover which will intensify the air-sea CO_2 exchange. Changes in the seasonality of biological production, will alter the air-sea CO_2 gradient through changes in seawater pCO2 and thereby the carbon exchange.
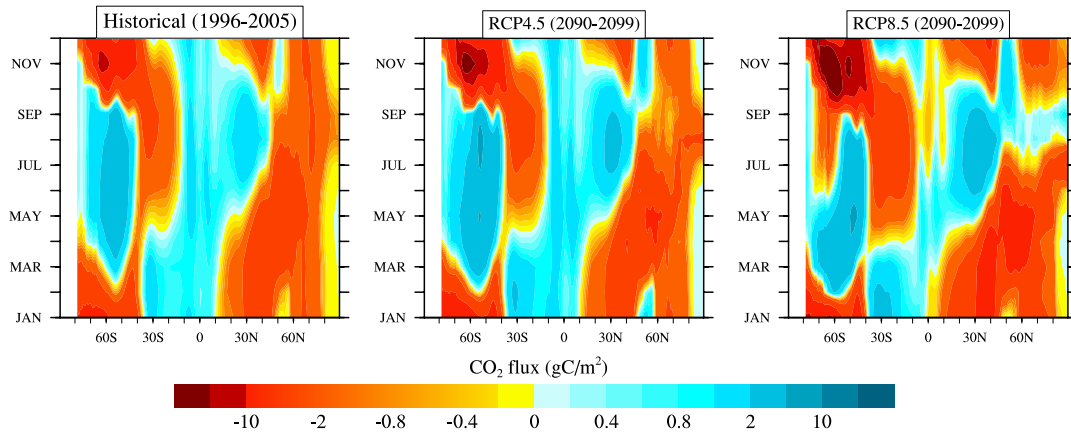

Figure 3.24: Zonal averages of ocean net carbon uptake in gC/m^2 for the historical experiment (left, multiannual mean over the period 1996 to 2005), RCP4.5 (middle) and RCP8.5 (right) scenarios (multi-annual mean over the period 2090 to 2099). Note the nonlinear scale in which the resolution increases when approaching zero.

Under the RCP8.5 scenario seasonal fluxes greatly intensify by the end of the century and the net CO_2 flux shifts direction over some latitudinal bands and periods (Figure 3.24). Latitudes of the Southern Ocean from 60° to 75° South remain as a net carbon sink under the RCP8.5 from March to June instead of from March to September as simulated during the historical period. From 60° to 15° South, the magnitude of the carbon exchange intensifies (i.e. stronger uptake/release of carbon). There are changes in the direction of the net flux over equatorial regions under the RCP8.5, with these regions becoming a weak sink of carbon over the second half of the year. This is due to the combined effects of the lower buffering capacity of seawater and the reduced seasonality of biological production over equatorial latitudes. Over latitudes of the North Atlantic subpolar gyre (between approx. 40° to 60° North), the RCP8.5 scenario not only shows an intensification in the magnitude of the fluxes but also a later seasonal transition: these latitudes become predominantly a source of carbon from August to December instead of from September to February. The warmer SST and the reduced sea ice cover by 2100 in the RCP8.5 scenario compared to the historical period, cause that regions over higher latitudes than 60° North become a weak source of atmospheric CO_2 at the end of the boreal summer.

Differences in the seasonal CO_2 fluxes between the SRM2100 and the RCP8.5 scenario are negligible over most of the latitudes (Figure 3.25). However, over latitudes higher than 60° North, the carbon exchange of the SRM2100 is similar to the one of the RCP4.5 scenario owing to their similar SST and sea ice cover. In other words, the colder (than RCP8.5) waters in the RCP4.5 and SRM2100 scenarios over these latitudes, absorb and store more carbon mainly due to the hampered CO_2 exchange in regions still covered by sea ice. Surface temperatures rapidly increase after termination of SRM which drastically reduces the sea ice area over the Arctic Ocean. Because of this, the seasonal air-sea CO_2 fluxes in the SRM2070 scenario are identical to those of the unmitigated RCP8.5. Ocean alkalinization directly increases the buffering capacity of seawater and enhances the air-sea CO_2 exchange. In our AOA2100 scenario, the uptake of carbon occurs throughout the whole year. But

this large impact on the seasonal carbon fluxes ceases once the addition of alkalinity ends. In the AOA2070 scenario, the buffering capacity of seawater returns to the same values than those of the reference RCP8.5 scenario, and thereby similar patterns of CO_2 exchange.
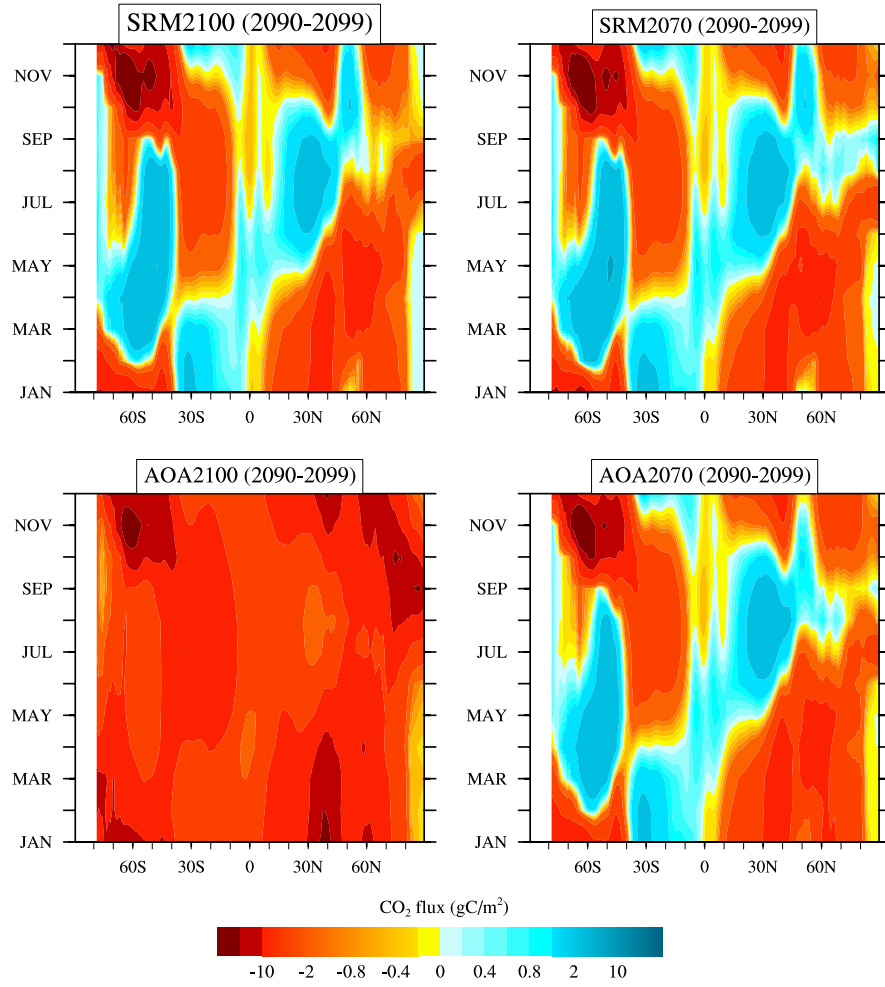
Figure 3.25: Zonal averages of ocean net carbon uptake in gC/m^2 for the climate engineering experiments (multi-annual mean over the period 2090 to 2099). Upper figures show results of the solar radiation management (SRM) scenario via stratospheric sulfur injection which implementation lasts until 2100 (left) and the experiment in which SRM terminates in 2070 (right). Bottom figures show the results of the artificial ocean alkalinization (AOA) scenario which implementation lasts until 2100 (left) and the experiment in which AOA terminates in 2070 (right). Note the nonlinear scale in which the resolution increases when approaching zero.

3.5.3 Seawater Carbonate Chemistry

The enhanced ocean CO_2 sink, increases the DIC content of surface seawater which reduces the buffer factors of pCO2, $[H^+]$ and Ω to changes in DIC and TA. Namely, surface seawater pCO2, $[H^+]$ and Ω become more sensitive to variations in DIC and TA (e.g., Egleston et al. 2010). These enhanced sensitivities are particularly relevant within seasonal timescales because the changes in the DIC owing to primary production and remineralization will modify the seasonality of pCO2, $[H^+]$ and Ω. In turn, biological processes depend on these parameters, and perturbations in their seasonality might induce changes in the marine biology. For instance, previous modeling studies have projected an amplified annual cycle of pCO2 under climate change scenarios (e.g., McNeil and Sasse 2016). These projections estimate that by 2100, if CO_2 emissions follow the RCP8.5 scenario, harmful high levels of pCO2 (i.e. ocean hypercapnia), would be achieved over major fishing areas several decades before expected if only the increase in the mean annual state of pCO2 is considered.

In line with previous projections (e.g., McNeil and Sasse 2016), the changes in the buffer factors of pCO2, $[H^+]$ and Ω modify their seasonal amplitudes under the RCP8.5 scenario. However, these effects on seasonality are fairly small compared to the projected changes in their associated mean annual states (Figures 3.26, 3.27, 3.29, 3.31). For example, over equatorial regions the average annual mean of surface seawater pCO2 during the historical period is ca. 380 ppm, and the seasonal deviations increase the monthly mean value by 7 ppm (around April/May) and decrease the monthly mean by 5 ppm (around September). In the RCP8.5, it is projected that the average annual mean of pCO2 over these regions by 2100 reaches ca. 920 ppm, and the seasonal amplitude amplifies so that the seasonal deviations increase the monthly mean up to 16 ppm and decrease the monthly mean by 13 ppm. Thus, the seasonal amplitude of pCO2 projected by the end of the century doubles compared to the historical period, but relative to the associated increase in the annual mean state, the enhanced seasonal amplitude is rather small.

The timing of the minimum pCO2 level within the year, shifts towards the end

of spring in the RCP8.5 scenario by the end of the century over high latitudes of the Northern hemisphere. This is because the temporal variations in the surface DIC content over the year in the RCP8.5 scenario by 2100, differ from those of the historical period primarily due to the altered patterns of primary production and remineralization induced by the changes in sea ice cover. Considering the spatial patterns of the changes in the seasonal amplitude of pCO2 projected in the RCP8.5 (Figure 3.30), most regions of the ocean double the seasonal amplitude of pCO2 relative to the historical period by 2100 (AF~2). However, there are some areas (e.g. equatorial regions in the Indian and Pacific Oceans) that reach an amplified seasonal amplitude of pCO2 three times higher than the one simulated during the historical period (AF~3). This is due to regional differences in the buffer factors of pCO2 and dissimilar variations in the DIC and TA changes over these regions during the year.

The projected variations in surface seawater acidity ($[H^+]$) in the RCP8.5 scenario by the end of the century, show magnitudes of change, temporal and spatial patterns similar to those associated with surface seawater pCO2 (Figure 3.28). This is caused by the similar buffering factors of these two parameters within the projected ranges of DIC and TA in the RCP8.5 scenario (Egleston et al. 2010). We use variations in $[H^+]$ to quantify the changes in acidity, instead of the most commonly used logarithmic scale (pH), because by using a logarithmic scale we remove the small differences between the values that we try to quantify. The average annual mean values and monthly deviations of $[H^+]$ (Figure 3.26) in pH scale can be found in the figure 3.27.

Differences in the perturbed seasonal amplitudes of pCO2 and acidity between the scenarios SRM2100 and RCP8.5 are negligible except for those over seawater in the Arctic Ocean. These differences over the Arctic Ocean, are due to the effect that sea ice has in the buffer factors of these parameters, and the different annual variation in surface DIC content between the SRM2100 and RCP8.5 scenarios. The SRM2070 and RCP8.5 scenarios show the same perturbation in the seasonal amplitudes of pCO2 and acidity. This is because the area covered by sea ice in the SRM2070

scenario is similar to the one projected under the RCP8.5 by 2100 which leads to similar buffer factors of pCO2 and [H$^+$].

Comparing the AOA2100 experiment with the RCP8.5 and SRM scenarios, pronounced differences arise between them. In the AOA2100 scenario, the increase in the annual mean state of surface seawater pCO2 and [H$^+$] projected by 2100 under the RCP8.5 and SRM scenarios is strongly mitigated. Moreover, the changes in the seasonal amplitudes of these parameters in the AOA2100 scenario by 2100, are even smaller than those associated with the RCP8.5 and SRM scenarios. These differences between the scenarios occur because the addition of TA into the seawater and the concomitant increase in the DIC content (due to the enhanced carbon uptake), directly change the buffer factors what affects the seasonality of pCO2 and [H$^+$]. Regarding regional differences in the AOA2100 scenario, the changes in the seasonal amplitudes of pCO2 and [H$^+$] are spatially inhomogeneous and large differences emerge between the different ocean basins. Some regions show an enhanced seasonal amplitude of pCO2 and [H$^+$] (e.g. Southern Ocean), while others present a damped seasonal amplitude of these parameters (e.g. equatorial west coast of South America). These inhomogeneous responses to AOA are determined by the particular biogeochemical states of the different ocean basins.

Considering the changes in Ω, the variations in the seasonal amplitude of Ω in the RCP8.5 and SRM scenarios are negligible (Figures 3.31 and 3.32). In contrast, in our AOA2100 scenario by the year 2100, Ω is brought to a regime where its seasonal amplitude is considerably enhanced in most of the ocean basins. Most of the oceans show an amplified seasonal amplitude of Ω in the large-scale AOA2100 scenario relative to the historical period by the end of the century. However, in the Southern Ocean the seasonal amplitude of Ω is similar to the one of the historical period because AOA compensates the projected reduction in the seasonal amplitude of Ω under the RCP8.5 scenario. The buffer factors of surface seawater return to the values of the unmitigated RCP8.5 scenario after termination of AOA, what vanishes any effect of AOA on the seasonality of seawater chemistry.

Figure 3.26: Monthly means (left column) and deviations from the annual means (right column) of surface seawater [H⁺] averaged over the years from 2090 to 2099 and within different latitudinal bands for the RCP8.5 scenario (solid line black), RCP4.5 (solid green), and the CE scenarios AOA and SRM until 2100 (blue and red solid lines, respectively) and until 2070 (blue and red dashed lines, respectively). The dashed black line shows surface seawater [H⁺] values as simulated in the historical period and averaged over the years from 1996 to 2005.

Figure 3.27: Monthly means (left column) and deviations from the annual means (right column) of surface seawater pH averaged over the years from 2090 to 2099 and within different latitudinal bands for the RCP8.5 scenario (solid line black), RCP4.5 (solid green), and the CE scenarios AOA and SRM until 2100 (blue and red solid lines, respectively) and until 2070 (blue and red dashed lines, respectively). The dashed black line shows surface seawater pH values as simulated in the historical period and averaged over the years from 1996 to 2005.

Figure 3.28: Regional values of the amplification factors (AF) of surface seawater [H$^+$] under the RCP scenarios 8.5 and 4.5 (top left and right), and the CE scenarios SRM (middle) and AOA (bottom) until 2100 (left) and until 2070 (right). The stippled regions indicate statistically significant differences in the seasonal amplitudes at the 95% confidence level.
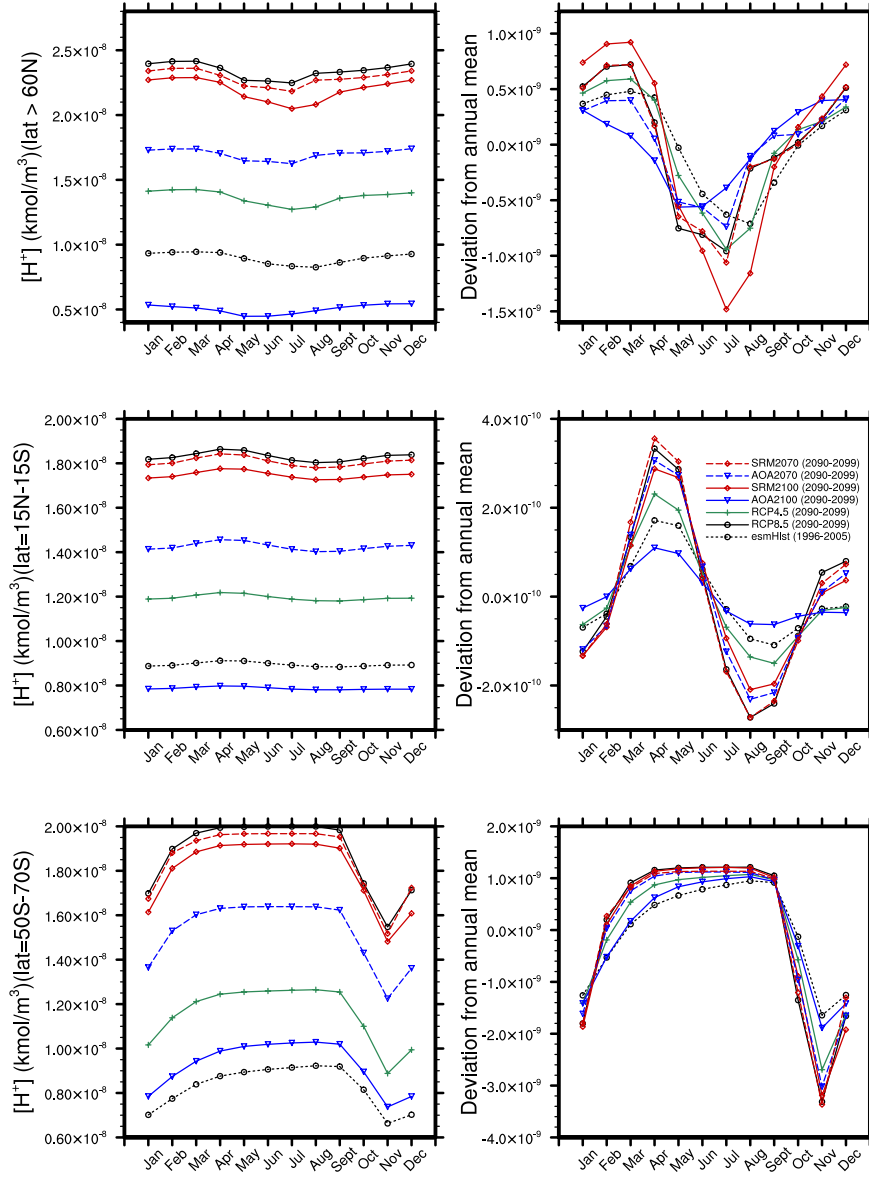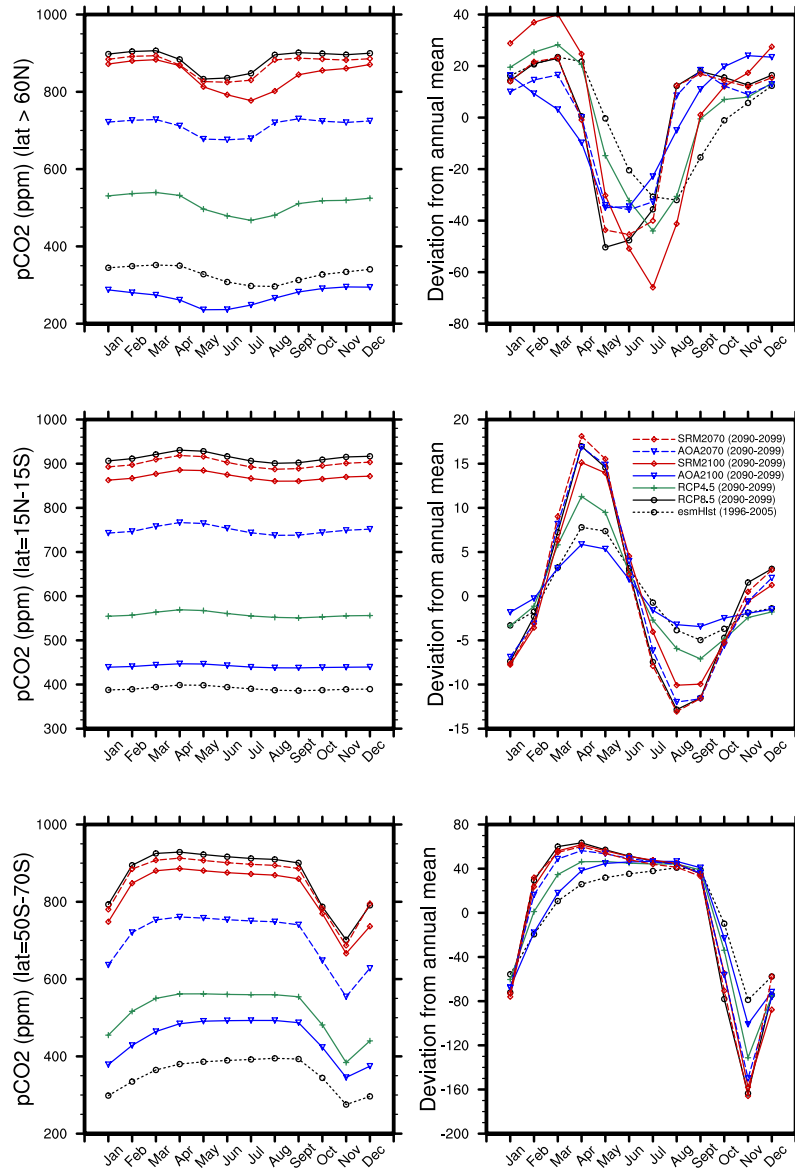
Figure 3.29: Monthly means (left column) and deviations from the annual means (right column) of the pCO2 in surface seawater averaged over the years from 2090 to 2099 and within different latitudinal bands for the RCP8.5 scenario (solid line black), RCP4.5 (solid green), and the CE scenarios AOA and SRM until 2100 (blue and red solid lines, respectively) and until 2070 (blue and red dashed lines, respectively). The dashed black line shows pCO2 in surface seawater values as simulated in the historical period and averaged over the years from 1996 to 2005.
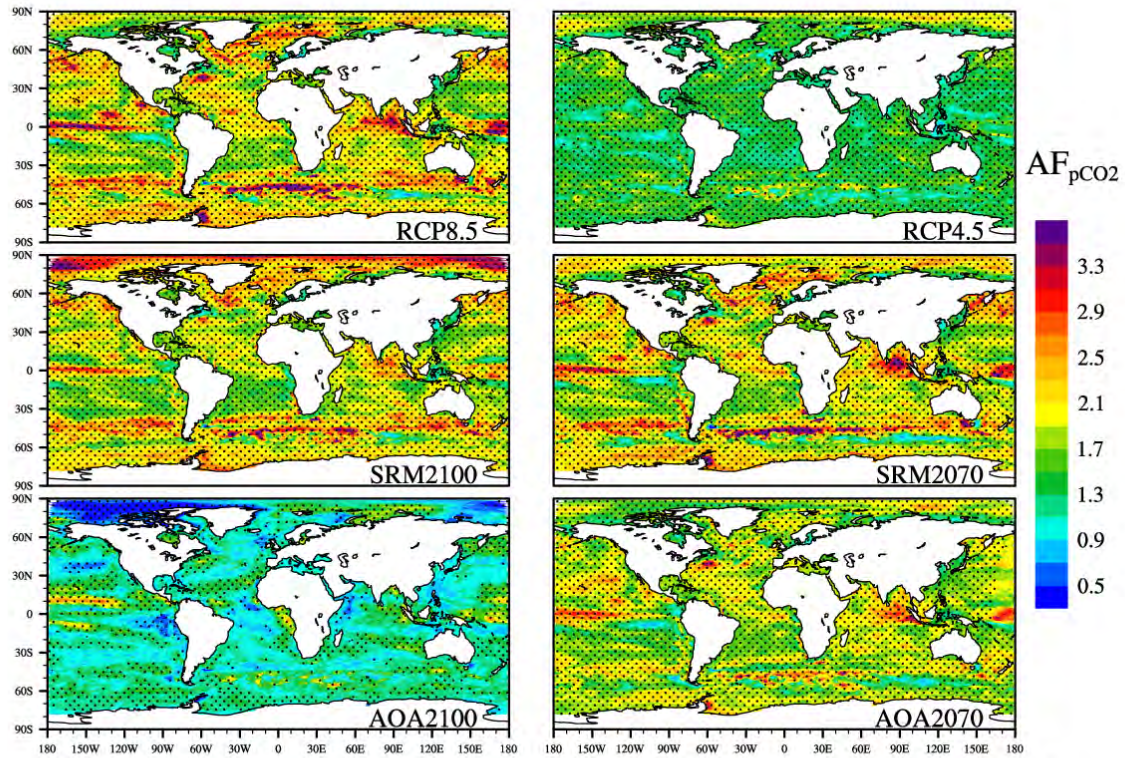
Figure 3.30: Regional values of the amplification factors (AF) of pCO2 in surface seawater under the RCP scenarios 8.5 and 4.5 (top left and right), and the CE scenarios SRM (middle) and AOA (bottom) until 2100 (left) and until 2070 (right). The stippled regions indicate statistically significant differences in the seasonal amplitudes at the 95% confidence level.
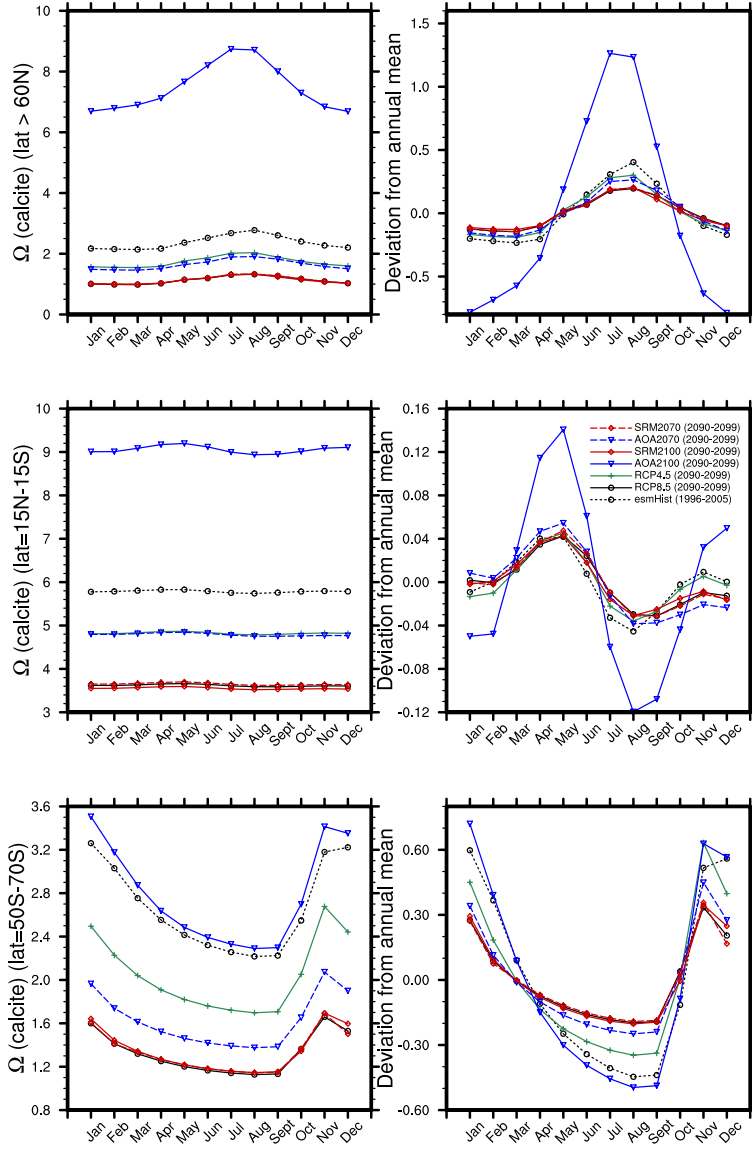
Figure 3.31: Monthly means (left column) and deviations from the annual means (right column) of surface seawater Ω averaged over the years from 2090 to 2099 and within different latitudinal bands for the RCP8.5 scenario (solid line black), RCP4.5 (solid green), and the CE scenarios AOA and SRM until 2100 (blue and red solid lines, respectively) and until 2070 (blue and red dashed lines, respectively). The dashed black line shows surface seawater Ω values as simulated in the historical period and averaged over the years from 1996 to 2005.
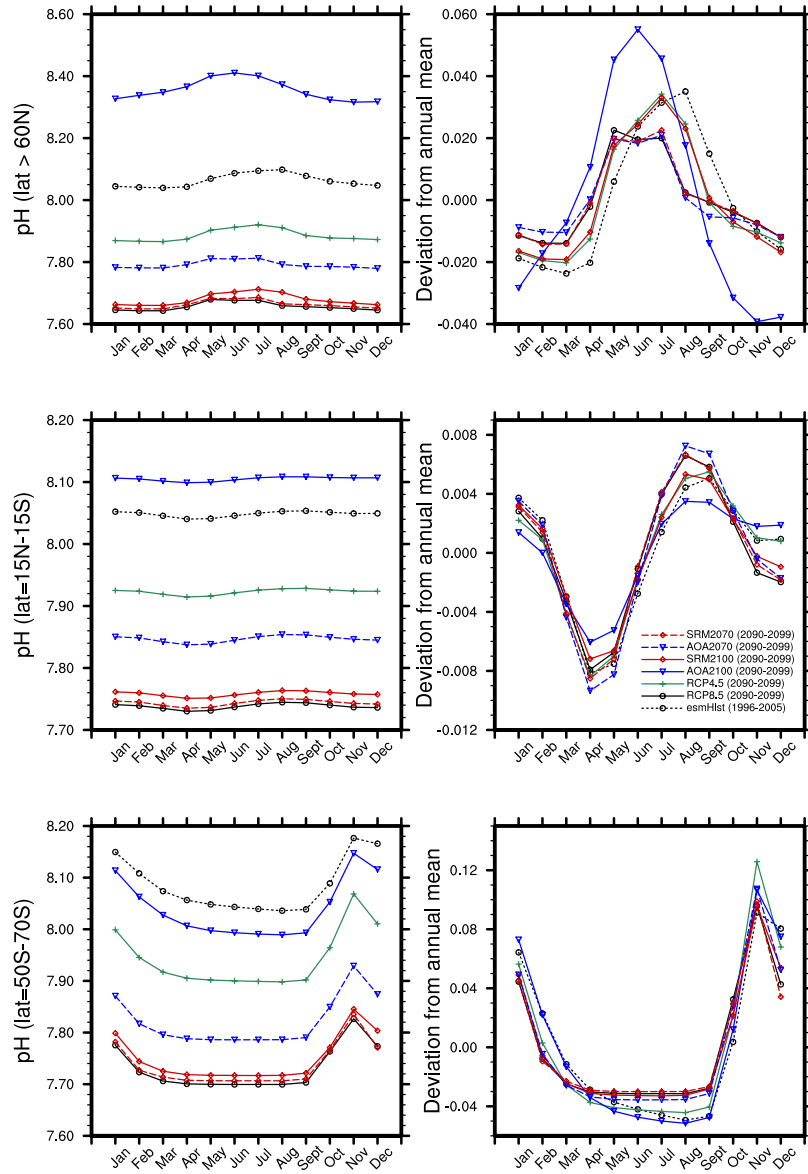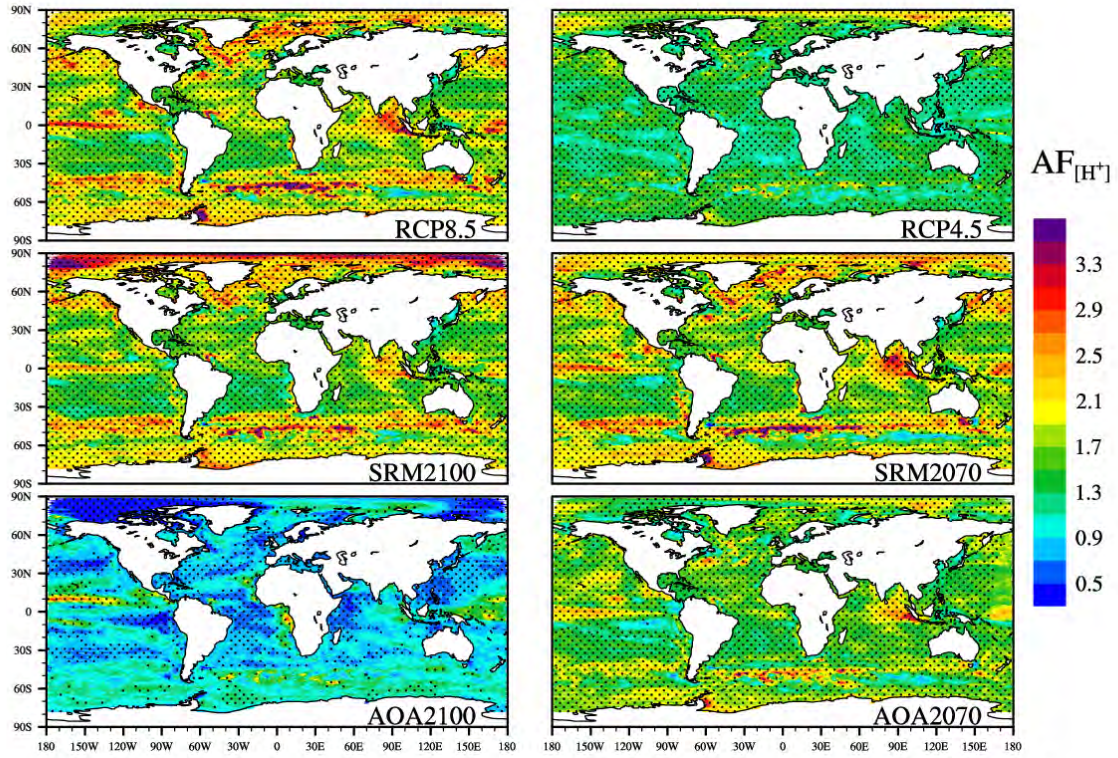
Figure 3.32: Regional values of the amplification factors (AF) of surface seawater Ω under the RCP scenarios 8.5 and 4.5 (top left and right), and the CE scenarios SRM (middle) and AOA (bottom) until 2100 (left) and until 2070 (right). The stippled regions indicate statistically significant differences in the seasonal amplitudes at the 95% confidence level.
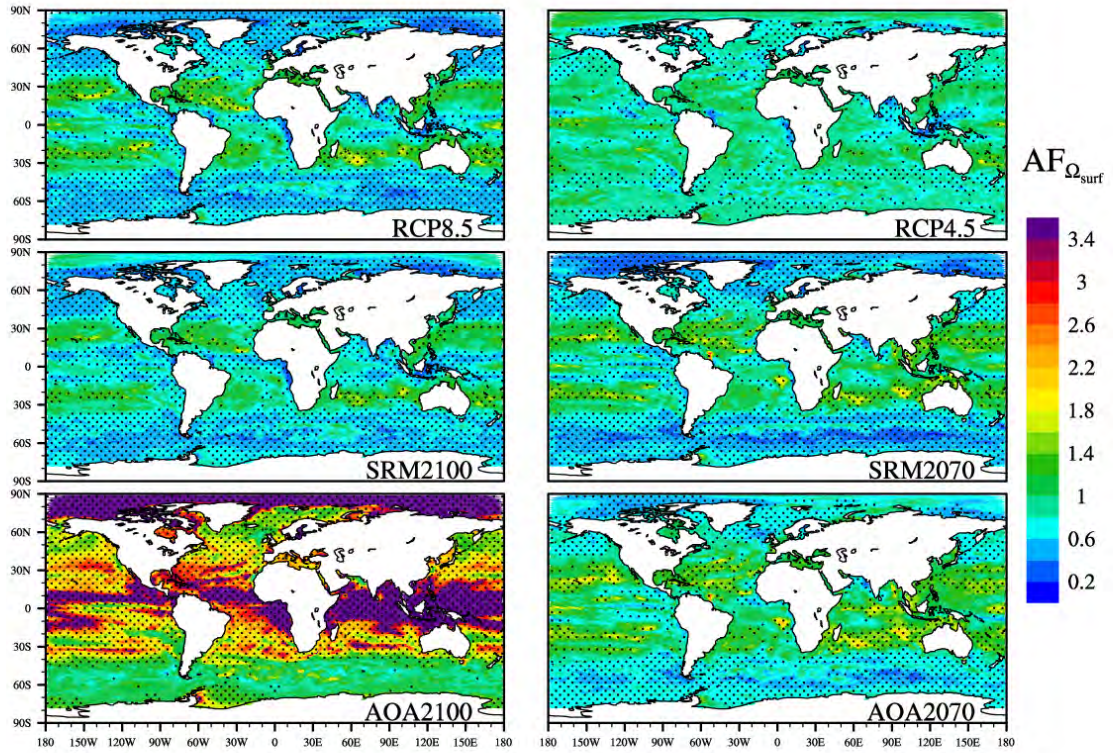
3.5.4 Marine Net Primary Production

The annual cycle of marine NPP is expected to change under climate change mainly due to an altered annual cycle of nutrient supply. Changes in the seasonal patterns of nutrients in the euphotic zone are primarily driven by variations in the seasonal amplitude of the MLD, which are caused by a changing seasonal amplitude of SST (Figure 3.23). By the end of this century, a general shrink of around 10% (relative the historical period) in the seasonal amplitude of the MLD is projected under the RCP8.5 scenario. This is because the annual maxima of SST increases faster than the annual minima in the RCP8.5 scenario (Henson et al. 2013). The changes in SST driven by our CE scenarios affect the seasonal amplitude of the MLD (Figure 3.33), thereby the annual cycle of marine NPP (Figure 3.34). The perturbed seasonal amplitude of NPP in our experiments, presents spatial heterogeneities that are common to all the scenarios and so that the local magnitude of the damping/amplification varies between simulations. Overall, most of the tropical and temperate regions show a strong damping in the seasonal amplitude of NPP (AF<1). However, the boundaries of the Pacific upwelling region show an enhanced amplitude up to 50% relative to the historical period (AF~1.5). In the North Atlantic, water masses of the west coast of North America present a weak amplification (AF>1), while over the west coast of Europe all the scenarios present a strong damping (AF<1). Over the Eurasian Basin of the Arctic Ocean the NPP seasonal amplitude increases but it decreases over the Canada Basin. The Southern Ocean shows an uneven pattern of changes in the seasonal amplitude of NPP. The enhanced stratification of the water column and the retreat of sea ice in polar regions, reduce the light limitation of photosynthesis over some areas which present an enhanced seasonal amplitude of NPP (e.g. Eurasian Basin of the Arctic Ocean). Regarding the different local magnitudes of change between the simulations, the RCP8.5 scenario shows local variations in the seasonal amplitude of NPP up to 50% different than the historical period. The AOA2100 and SRM2100 scenarios have similar local variations to those associated with the RCP4.5 scenario because these experiments have similar changes in the seasonal amplitude of the MLD. The perturbed NPP seasonal amplitudes in the

AOA2070 and SRM2070 scenarios, resemble those of the RCP8.5 due to the rapid response of the MLD to the SST warming after termination of CE.
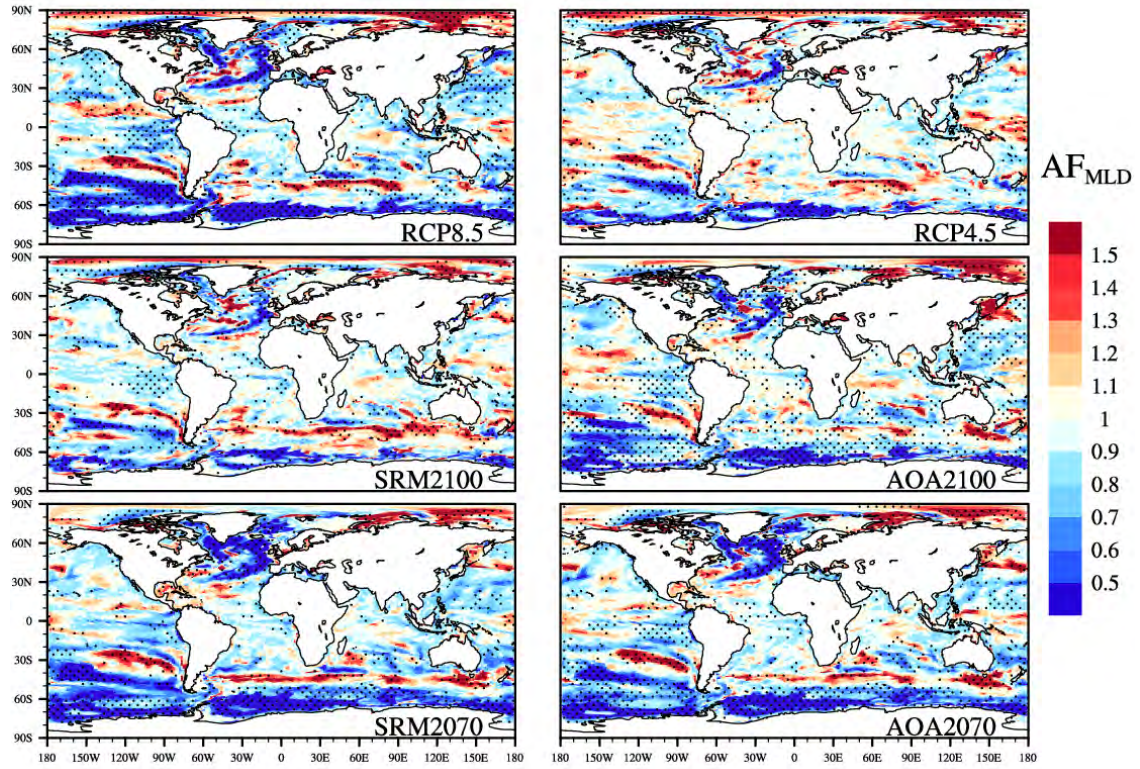
Figure 3.33: Regional values of the amplification factors (AF) of the annual average mixed layer depth (MLD) under the RCP scenarios 8.5 and 4.5 (top left and right), and the CE scenarios SRM (middle) and AOA (bottom) until 2100 (left) and until 2070 (right). The stippled regions indicate statistically significant differences in the seasonal amplitudes at the 95% confidence level.
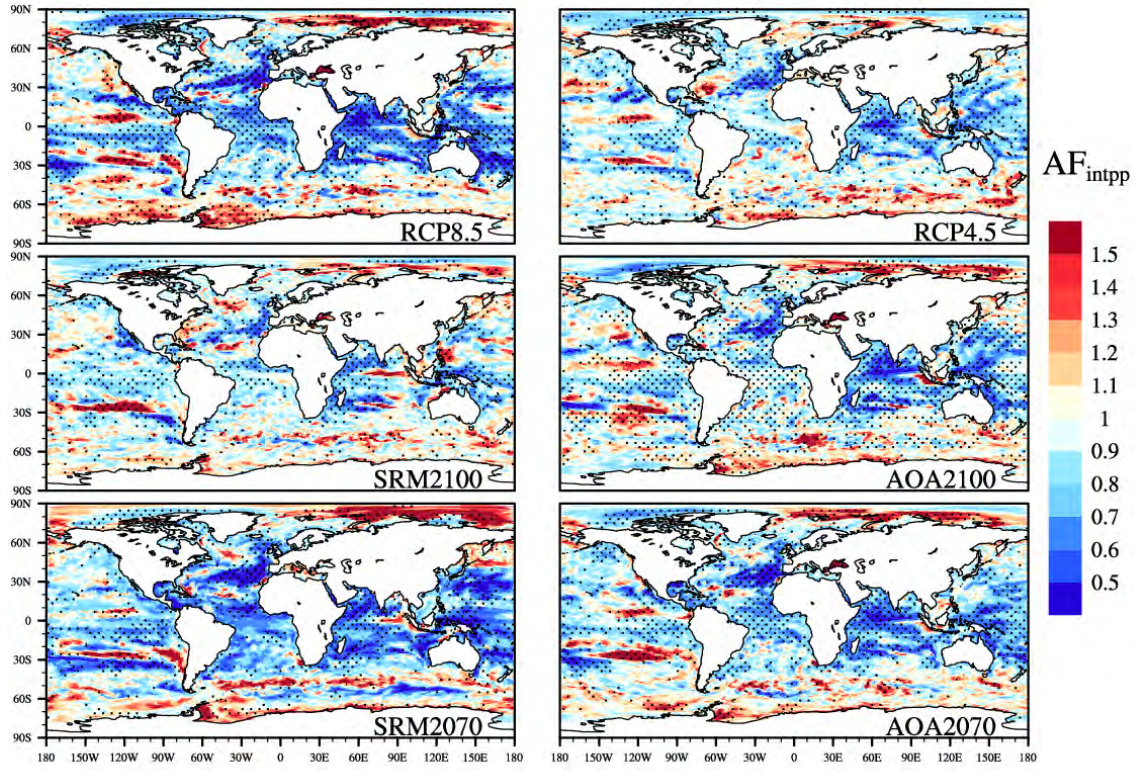
Figure 3.34: Regional values of the amplification factors (AF) of the annual average integrated ocean primary production (intpp) under the RCP scenarios 8.5 and 4.5 (top left and right), and the CE scenarios SRM (middle) and AOA (bottom) until 2100 (left) and until 2070 (right). The stippled regions indicate statistically significant differences in the seasonal amplitudes at the 95% confidence level.

3.6 Summary and Conclusions

We explore the response of the Earth system to large-scale AOA and SRM scenarios and carry out a comparative assessment of these two different CE approaches. We perform idealized AOA and SRM scenarios using the MPI-ESM with interactive carbon cycle. Both CE methods are simulated using the same model, which allows a consistent comparison of their effects and excludes differences due to model parameterizations. Due to our modeling approach including three ensemble members, we also discuss the CE-driven response of the system in the context of internal model variability. The main focus of our analysis is on the effects of CE on the global carbon cycle and the ocean biogeochemistry. We compare the impacts of AOA and SRM from two different perspectives: their effects on seasonal variability and their influence on the rates of environmental change upon termination of CE.

In our SRM simulations, surface atmospheric temperatures are stabilized to similar levels than those of the RCP4.5 scenario under RCP8.5 emissions by reducing the net TOA radiation of the RCP8.5 scenario to RCP4.5 values via SRM. In this colder (than RCP8.5) climate state with high atmospheric CO_2 levels, the land and ocean carbon sinks are enhanced. By the end of the century, the lower surface temperatures and high CO_2 levels of this SRM scenario, boost the uptake and storage of carbon by the land biosphere what enhances the terrestrial carbon pool by 92 GtC relative to the RCP8.5 (3650 GtC). The enhanced carbon storage in the ocean owing to the effects of this SRM scenario is much lower than the enhanced storage over land. By the year 2100, the ocean carbon reservoir is only 8 GtC higher than in the RCP8.5 scenario (43086 GtC). Termination of SRM leads to a rapid surface warming, which returns to the atmosphere the additionally (relative to the unmitigated RCP8.5) stored carbon in land and ocean. Thus, potential mitigating effects of SRM in terms of atmospheric CO_2 reduction, vanish after the implementation of the SRM ends.

Global addition of ca. 114 Pmol of alkalinity (in total) into the surface ocean

until the year 2100, stabilizes atmospheric CO_2 concentrations to RCP4.5 levels under RCP8.5 emissions. This mitigates global warming by 1.5 K compared to the RCP8.5 scenario. However, the average surface atmospheric temperature is still 0.5 K higher than the targeted RCP4.5 scenario by 2100 due to the radiative forcing effect of other GHGs that remain unmitigated. From the 1849 Gt of carbon emitted into the atmosphere until 2100 in the RCP8.5 scenario, the ocean removes 940 GtC and this lowering of atmospheric CO_2 reduces the effect of CO_2 fertilization on the terrestrial biosphere. This response of land biota to the effects of AOA reduces the terrestrial carbon pool by 30 GtC relative to the RCP8.5 by 2100. The sequestered carbon in seawater via AOA remains bound in the ocean reservoir after termination of AOA. However, the constant supply of alkalinity into the surface seawater is required to enhance the ocean carbon sink. After termination of AOA, the pace at which atmospheric CO_2 accumulates in the atmosphere is set by the emissions of the reference RCP8.5 scenario. This leads to a temporal evolution of global mean surface atmospheric temperature that paralelly follows the trajectory of the RCP8.5 projection, albeit at lower values. The addition of ca. 45 Pmol of alkalinity (in total) into the global surface ocean until 2070, prevents around 0.5 K of global warming compared to the RCP8.5 scenario.

The comparison of terminated CE scenarios with the reference RCP8.5, reveals differences in the regional rates of ocean and atmospheric warming. In line with previous studies (e.g., Brovkin et al. 2009; Jones et al. 2013), local rates of warming largely exceed those associated with the RCP8.5 scenario after sudden termination of SRM. In our terminated SRM scenario, some regions at high latitudes of the Northern hemisphere reach rates of warming one order of magnitude higher than those projected in the RCP8.5 (up to 0.14 K/yr) due to polar amplification. Regional patterns of warming are in general conserved (i.e. higher warming over the Arctic and the continents), but there are pronounced regional differences mainly due to differences in their regional background states, as, for instance, over Antarctica and tropical oceans.

After termination of our large-scale AOA scenario, local rates of warming present

similar values to those associated with the RCP8.5 scenario. Yet, the spatial patterns of warming between these scenarios differ. Particularly, over the North Atlantic Ocean, Northern Europe and the European shores of the Arctic, the local rates of surface warming after termination of AOA exceed the rates of the RCP8.5 scenario. Moreover, they even reach values as high as in our terminated SRM scenario which might lead to negative ecological consequences for local ecosystems. However, these differences in trends occur in a background of internal model variability of surface warming which changes locally with forcing, and that achieve values as large as the warming trend. In general, high latitudes of the Northern hemisphere present larger internal variability of surface warming compared with other regions.

AOA and SRM methods do not only affect multi-decadal trends of surface temperatures, they also modify surface temperatures within annual timescales. Our CE scenarios with AOA or SRM continuously applied until 2100, mitigate the perturbed seasonal cycle of surface atmospheric temperatures projected under the RCP8.5 (Dwyer 2014), by reducing the changes in the seasonal amplitudes to those associated with the targeted RCP4.5. These AOA and SRM scenarios present similar spatial patterns on their effects on the seasonal amplitudes of surface temperatures, despite of the different atmospheric forcings that are modified by these methods (i.e. net TOA radiation in SRM and radiative forcing by atmospheric CO_2 in AOA). The effects on the seasonal cycle of surface temperatures due to the AOA or SRM scenarios, vanish in a few decades after termination of CE and the perturbed seasonality returns to the regional patterns projected under the unmitigated scenario.

The mitigated ocean warming by our large-scale AOA and SRM scenarios, reduces the enhanced stratification of the water column and the concomitant reduction in nutrient supply. Ocean NPP behaves in accordance to these changes in the physicochemical properties of seawater, and the overall decrease in NPP projected in the RCP8.5 is reduced to the levels of the targeted RCP4.5 scenario in intra-annual and multi-decadal timescales. However, model internal variability is large for this parameter what complicates the identification of trends between scenarios. The physicochemical state of seawater adjusts rapidly to the changes in the climate

state. Therefore, the changes in NPP brought about by AOA or SRM return to the projected changes in the unmitigated scenario after termination of CE faster than in the RCP8.5 within decades and following the pace of seawater warming. These fast-paced environmental changes might add additional pressure on biological systems coping with climate change and ocean acidification, which ecological consequences are unknown (e.g., Bopp et al. 2013).

Seawater biogeochemistry is not only affected by changes in stratification, the enhanced ocean carbon sink owing to the increasing atmospheric CO_2 levels, induces changes in the ocean carbonate chemistry and the acidification of seawater. The effects of SRM on seawater carbonate chemistry in multi-decadal and intra-annual timescales are negligible over the global ocean, with the perturbed carbonate chemistry being defined by the emission scenario. However, small differences arise between the unmitigated RCP8.5 and the SRM scenarios over polar regions where the retreat of sea ice has been reduced by SRM. Over the decades, the presence of sea ice blocks the CO_2 exchange in the polar oceans, which slightly reduces the gradual acidification of surface seawater. Within annual timescales, these scenarios differ in their seasonal cycle of seawater carbonate chemistry over polar regions due to the effects of sea ice on the buffer factors and in the annual DIC variation through changes in primary production and remineralization.

While the effects of SRM on the ocean carbonate chemistry are minor, AOA leads to pronounced changes in the carbonate chemistry that are directly caused by the addition of alkalinity. AOA largely mitigates the effects of ocean acidification but a dissimilar increase in DIC and TA in the alkalinized seawater due to our scenario design, leads to pH and Ω values that exceed those of the historical period in several regions. Over some areas in the Arctic Ocean, surface seawater pH values that are 0.6 higher than those of the historical period are reached by 2100 in our AOA scenario with addition of TA until 2100. Further, Ω has a fivefold increase in some regions of the Arctic Ocean and over tropical oceans (where most corals grow) Ω doubles its value relative to the historical period.

Implementation of AOA causes rapid variations in the seawater chemical environment and the consequences for the marine biota are unknown. In shallow basins or tropical oceans where vertical mixing is limited by thermal stratification, the enhanced uptake of CO_2 following AOA, may not compensate the disequilibrium in the carbonate system what leads to a rapid increase in Ω. Termination of AOA also causes rapid variations in the marine biogeochemical environment (e.g. SST, pH, pCO2, Ω and ocean NPP). For instance, right after termination of AOA in 2070, local trends in ocean acidification exceed regionally those in the RCP8.5 scenario and become up to one order of magnitude higher than in the RCP8.5 (e.g. over the Arctic Ocean and tropical oceans).

AOA affects the seasonal cycle of seawater carbonate chemistry through its effect on the buffer factors. However, these effects on seasonality are rather small compared to the associated changes in the mean annual states induced by AOA. The response of the seasonal amplitude of surface seawater pCO2 and acidity to AOA is spatially inhomogeneous and it depends on the different regional sensitivities to addition of TA. The seasonal amplitude of Ω is in general enhanced by AOA, with the exception of the Southern Ocean where AOA compensates the projected reduction in the seasonal amplitude of Ω under the RCP8.5. With termination of AOA, the buffer factors of surface seawater return to the values of the unmitigated scenario within years, which vanishes any effect of AOA on the seasonality of seawater chemistry. To conclude, these results show that AOA-driven changes in the marine biogeochemical environment expose biological systems to rapid variations which consequences for the ecosystems are unknown. Moreover, this research reveals that large-scale AOA and SRM scenarios impact the seasonal cycle of ocean properties that are biologically relevant, adding additional pressure on biological systems.

Chapter 4

Conclusions and Outlook

4.1 Conclusions

I explore the Earth system response to large-scale AOA and SRM scenarios and
compare the effects of these different CE schemes. My analysis focuses on the im-
pacts of CE on the regional patterns of surface temperatures, carbon uptake and
ocean biogeochemistry. I analyze idealized scenarios of AOA and SRM, using the
state-of-the-art MPI-ESM forced by fossil-fuel CO_2 emissions. I use forcing accord-
ing to the RCP8.5 in the AOA and SRM scenarios, where CE is either continuously
applied during the 21st century until 2100 or terminated in 2070. Both methods are
simulated using the same model framework, which excludes discrepancies caused by
differences in parameterizations allowing a consistent comparison between these CE
schemes. Unlike previous studies, my modeling approach includes internal model
variability, whereby the response of the system to CE is discussed within the context
of internal variability. I explore the CE-driven response of the system on two differ-
ent time scales: multi-decadal rates of environmental change and effects on seasonal
variability. My thesis concludes by answering the research questions posed in the
introduction and developed throughout the previous chapters.

How much does the buffering capacity of the ocean need to be enhanced in order to stabilize the atmospheric CO_2 to RCP4.5 levels in a high CO_2 emissions scenario RCP8.5?

My study shows that atmospheric CO_2 is held at RCP4.5 levels under RCP8.5 emissions via the addition (in total) of approx. $114 \cdot 10^{15}$ mol (Pmol) of alkalinity into the surface ocean until the end of the 21st century. The increasing levels of atmospheric CO_2 in the RCP8.5 scenario (up to 950 ppm by 2100) entails a global, steadily growing supply of total alkalinity (TA) into the surface seawater. Overall, this large-scale AOA scenario leads to 30% higher (relative to current levels) surface TA concentration by 2100. Despite homogeneous addition of TA into the surface ocean (including ice-covered areas) the added TA spreads differently over the water column in each ocean basin owing to the particular current dynamics of each basin. The volume of water that dissolves the added alkalinity determines the increment of TA per unit volume in each ocean basin. That is why the characteristically well-mixed Southern Ocean presents a temporal and spatial evolution of TA concentration that remains at current levels despite of an intense addition of alkalinity. In contrast, the Arctic Ocean, that is relatively shallow and isolated from the other ocean basins, shows a greater impact on the concentration of TA per unit volume compared to other ocean basins. This large-scale AOA scenario demands a vast amount of processed alkaline minerals. The production of 114 Pmol of TA requires a minimum amount of $4.22 \cdot 10^{12}$ metric tons (Tt) of lime. This implies an increase by 2 orders of magnitude of the total production of lime within this century. When using olivine to obtain the same amount of TA, approx. 4.01 Tt of olivine (at least) are needed, which involves an enhancement by 3 order of magnitude of the total production of olivine by 2100.

What would be the consequences of a large-scale alkalinization scenario in the Earth system?

The addition of ca. 114 Pmol of alkalinity (in total) in the global ocean surface, stabilizes atmospheric CO_2 levels to the trajectory of the RCP4.5 scenario under RCP8.5 emissions over this century. The whole ocean turns into a carbon sink including the tropical ocean which otherwise outgases CO_2 to the atmosphere. My results suggest that because of the effects of this vast amount of added alkalinity in the seawater carbonate system, the ocean removes half of the CO_2 emitted into the atmosphere (940 GtC), which ultimately determines the response of the climate system. By the end of this century, the global warming projected under the high emissions RCP8.5 scenario is reduced by 1.5 K. Yet, the global surface atmospheric temperature remains 0.5 K higher than the targeted RCP4.5 owing to the radiative forcing effect of non-CO_2 GHGs. The state of the climate adjusts to the slightly higher (than RCP4.5) atmospheric temperatures, and the reduced warming avoids the extreme sea level rise and ice decline. Earth system variables such as, for instance, atmospheric precipitation, AMOC, oxygen levels overlying intermediate waters and ocean net primary production, act in accordance with the different climate state. My analysis reveals that, although the internal model variability of these parameters is large, the AOA signal becomes evident and multi-decadal trends are consistent among the ensemble members.

The increase in the dissolved inorganic carbon (DIC) content in seawater nearly doubles the one projected under the RCP8.5 scenario by the end of this century due to the AOA-driven enhancement of the carbon sink. The alkalinization fully compensates the acute ocean acidification that would accompany this larger CO_2 invasion into the ocean. And yet, it causes the side effect of surface seawater pH and Ω largely exceeding regionally contemporary levels with unknown consequences for marine ecosystems. For the first time I demonstrate that pronounced regional

differences arise on the pH and Ω response to AOA despite the spatially homogeneous addition of alkalinity. The particular biophysicochemical regimes of the different ocean basins engender differences in the regional sensitivities to rising seawater alkalinity. The Arctic Ocean and tropical oceans emerge as *hot spots* for the unintentional changes in seawater carbonate chemistry induced by large-scale AOA. The dissimilar increase in the DIC to TA ratio in this large-scale AOA scenario boosts surface seawater pH (up to 0.6 higher units) and Ω (fivefold increase) to higher values than present-day levels in the Arctic Ocean. In the tropical oceans, surface seawater Ω doubles contemporary values following the increasing carbonate ions concentrations. Therefore, the large CO_2 removal potential of AOA comes at a price of an unprecedented perturbation in seawater carbonate chemistry whose ecological consequences are entirely unknown.

> What is the potential of large-scale AOA and SRM scenarios to exceed the rates of environmental change that they were intended to mitigate?

My results suggest that, compared to the reference RCP8.5, large-scale AOA and SRM scenarios have a large potential to significantly exceed the pace at which biologically relevant environmental properties change. In line with previous studies (e.g., Jones et al. 2013), the local rates of surface atmospheric warming after termination of SRM greatly exceed those projected under the unmitigated RCP8.5 scenario. Some regions at high latitudes of the Northern hemisphere achieve rates of surface warming even one order of magnitude larger (up to 0.14 K/yr) than in the RCP8.5. Regional patterns of warming are overall conserved, with higher trends over the Arctic and the continents in the RCP8.5 and terminated SRM scenarios. Still, notable regional differences arise between these scenarios as, for instance, over Antarctica and tropical oceans. I show that local trends in surface warming are broadly similar to those of the RCP8.5 scenario after termination of AOA, yet the spatial patterns differ. At high latitudes over the North Atlantic Ocean, Northern

Europe and the European shores in the Arctic, rates of increasing temperatures locally exceed those of the RCP8.5 after termination of AOA. Further, some regions reach warming trends as large as in the terminated SRM scenario and up to one order of magnitude larger than in the unmitigated RCP8.5. Hence, my study reveals that the termination of large-scale AOA and SRM scenarios, induces faster local changes of surface temperates than those intended to alleviate. These trends occur, however, on a background of large model internal variability, which differs between the simulations and complicates the identification of local trends. In general, high latitudes of the Northern hemisphere show larger model internal variability of surface warming compared with other regions.

The SRM-driven effect on multi-decadal trends in seawater carbonate chemistry is minor over the global ocean, but when compared to the unmitigated RCP8.5 scenario, small differences emerge due to the direct effect of SST on the carbonate system and over polar regions with sea ice. The presence of sea ice impedes CO_2 exchange, leading to a slightly lower acidification of surface seawater over time. Whilst SRM-driven effects on the ocean carbonate chemistry are minor, AOA directly impacts seawater chemistry. For the first time I show that large-scale AOA leads to rapid variations in the seawater chemical environment where vertical mixing is limited. In shallow basins such as the Arctic Ocean, or tropical oceans where vertical mixing is constrained by thermal stratification, the enhanced carbon uptake after the alkalinity addition does not fully compensate the disequilibrium induced by AOA leading to a rapid Ω rise. Further, my results suggest that ocean biogeochemistry undergoes rapid perturbations after termination of AOA, with areas of limited vertical mixing showing higher sensitivity. Upon termination of AOA in 2070, local trends in ocean acidification exceed those projected under the RCP8.5 scenario. For instance, the rates of change in surface pH and Ω become regionally up to one order of magnitude higher than those in RCP8.5 over the Arctic Ocean and tropical oceans. The ecological consequences of these rapid perturbations remain largely unknown, but they may be unfavorable, owing to the additional pressure on biological systems caused by fast-paced environmental changes and the simultaneous

exposure to multiple stressors (Bopp et al. 2013).

How large-scale AOA and SRM scenarios affect the seasonal variability of biologically relevant ocean biogeochemical properties?

My study shows that large-scale AOA and SRM scenarios aiming at achieving a climate state similar to the one associated with the RCP4.5 scenario under RCP8.5 emissions reduce the altered seasonal cycle of surface temperature projected under the RCP8.5. These large-scale CE scenarios decrease the perturbed seasonal amplitudes of surface temperature under RCP8.5 forcing down to similar spatial patterns projected in the targeted RCP4.5 scenario. Despite the different atmospheric forcings that are modified by these methods (i.e. net TOA radiation by SRM and radiative forcing effect of CO_2 by AOA), these AOA and SRM scenarios do not present regional differences in their effects on seasonal variability of surface temperatures. Within a few decades, any effect on the seasonal cycle of surface temperature due to large-scale AOA and SRM scenarios vanishes, and the regional patterns of perturbed seasonality return to those associated with the unmitigated RCP8.5 scenario.

The reduced surface ocean warming in the large-scale AOA and SRM scenarios decreases the projected decline in the seasonal amplitude of the MLD under RCP8.5 forcing, thereby the collateral decline in nutrient availability within annual time scales. Seasonal variability of ocean NPP behaves in accordance to these changes in the physicochemical properties of seawater. My study reveals that the regional patterns of perturbed seasonality of NPP in the RCP8.5 are brought to those of the targeted RCP4.5 scenario, albeit showing large internal model variability. The effects of AOA and SRM on the seasonal variability of NPP cease rapidly with termination of CE, because of the fast response of the physicochemical state of surface seawater to the changes in atmospheric forcing and the increasing surface temperatures.

The impact of SRM on surface seawater carbonate chemistry within annual time scales is minor over the global ocean. Only small differences arise between the SRM scenarios and the unmitigated RCP8.5 over polar regions, where SRM affects the spatio-temporal evolution of sea ice. The presence/absence of sea ice influences the seasonal variability of surface seawater carbonate chemistry mainly through its effect on the air-sea CO_2 exchange, its impact on the seawater buffering capacity and its associated changes in marine primary production and remineralization. Whereas the SRM-driven effects on the seasonal variability of seawater carbonate chemistry are negligible, addition of alkalinity directly modifies the buffer factors, leading to a greater (than SRM) impact on carbonate chemistry seasonality. Such AOA-driven effects on seawater carbonate chemistry within annual time scales are significantly smaller than the changes in the mean states conjointly induced by AOA. However, the seasonal amplitude of Ω is largely amplified (threefold increase) by AOA everywhere, except for the Southern Ocean, where AOA counteracts the damped seasonal amplitude of Ω projected in the RCP8.5. The surface seawater carbonate system of the global ocean returns rapidly (within years) to the regime associated with the RCP8.5 scenario after termination of large-scale AOA. Accordingly, any effect of AOA on seasonal variability of seawater carbonate chemistry dissipates.

To conclude, my study shows that the large CO_2 removal potential of AOA comes at a price of an unprecedented perturbation in the marine chemical environment whose impacts on biological systems are currently unknown. For the first time, I demonstrate that the unintended consequences brought about by alkalinity enhancement in the ocean arise not only due to the AOA-driven variations in the magnitude of change, but also due to its pace. Finally, my research reveals that large-scale AOA and SRM scenarios impact seawater properties that determine biological processes within annual time scales, adding additional pressure on marine biology exposed to fast-paced changes in their environment.

4.2 Outlook

My research brings new insights into the scientific debate on CE, but also breeds new stimulating questions:

- My experimental approach has revealed that each ocean basin presents a particular sensitivity to AOA. In light of these results, regional AOA model scenarios may be studied so that the CO_2 removal potential is maximized whilst minimizing side effect. For instance, the Southern Ocean emerges as perfect candidate for a new set of CE scenarios of regional AOA.

- The physicochemical background state of the Earth system largely determines the mitigation potential and side effect of CE methods. Feedbacks, synergistic and/or antagonistic effects might arise when several CE methods are applied in parallel. A comprehensive assessment of these aspects requires a set of CE scenarios where the AOA and SRM methods are combined. Not only that, but also the termination effects when several CE methods are applied together may vary. Thus, a new set of terminated CE experiments would be needed so that the combined effects of different CE schemes can be properly addressed.

- An exciting and timely topic that needs to be studied is the detection and attribution of CE-driven effects. This could be assessed, for instance, by using optimal fingerprinting methods. This new analysis follows naturally the research conducted in this thesis and it requires no additional experiments. The results of the AOA and SRM simulations might be further analyzed in order to detect when the induced changes in the climate system become detectable (e.g. induced changes in surface temperatures). Within this context, different types of comparisons can be done, e.g. the detection of the perturbations in the current state of the system driven by the CE methods. In other words, a comparison between the state of the Earth system after CE and the state of the system prior to the application of such CE methods. Another interesting comparison might be the detection of the mitigation effects of the CE

approaches by exploring the state of the system under the RCP8.5 scenario and the changes driven by CE. Namely, the comparison between the state of the system after CE and the state of the system in the unmitigated RCP8.5 scenario.

Bibliography

Albright, R., et al., 2016: Reversal of ocean acidification enhances net coral reef calcification. *Nature*, **531 (7594)**, 362–365, doi:10.1038/nature17155, URL `http://dx.doi.org/10.1038/nature17155`.

Andrews, O. D., N. L. Bindoff, P. R. Halloran, T. Ilyina, and C. Le Quéré, 2013: Detecting an external influence on recent changes in oceanic oxygen using an optimal fingerprinting method. *Biogeosciences*, **10 (3)**, 1799–1813, doi:10.5194/bg-10-1799-2013.

Arrigo, K. R., 2013: The changing Arctic Ocean. *Elementa Science of the Anthropocene*, doi:10.12952/journal.elementa.000010.

Arrigo, K. R., et al., 2012: Massive phytoplankton blooms under Arctic sea ice. *Science*, doi:10.1126/science.1215065, URL `http://science.sciencemag.org/content/early/2012/06/06/science.1215065`.

Bathiany, S., M. Claussen, and V. Brovkin, 2014: CO_2-induced Sahel Greening in Three CMIP5 Earth System Models. *Journal of Climate*, **27 (18)**, 7163–7184, doi:10.1175/JCLI-D-13-00528.1, URL `http://dx.doi.org/10.1175/JCLI-D-13-00528.1`.

Behrenfeld, M. J., et al., 2006: Climate-driven trends in contemporary ocean productivity. *Nature*, **444 (7120)**, 752–755, doi:10.1038/nature05317.

Bintanja, R. and E. C. van der Linden, 2013: The changing seasonal climate in the Arctic. *Nature*, **3**, doi:10.1038/srep01556, URL `http://dx.doi.org/10.1038/srep01556`.

Bopp, L., et al., 2013: Multiple stressors of ocean ecosystems in the 21st century: projections with CMIP5 models. *Biogeosciences Discussions*, **10 (2)**, 3627–3676, doi:10.5194/bgd-10-3627-2013, URL `http://www.biogeosciences-discuss.net/10/3627/2013/`.

Brovkin, V., L. Boysen, T. Raddatz, V. Gayler, A. Loew, and M. Claussen, 2013: Evaluation of vegetation cover and land-surface albedo in MPI-ESM CMIP5 simulations. *Journal of Advances in Modeling Earth Systems*, **5 (1)**, 48–57, doi: 10.1029/2012MS000169, URL `http://dx.doi.org/10.1029/2012MS000169`.

Brovkin, V., V. Petoukhov, M. Claussen, E. Bauer, D. Archer, and C. Jaeger, 2009: Geoengineering climate by stratospheric sulfur injections: Earth system vulnerability to technological failure. *Climatic Change*, **92 (3)**, 243–259, doi:10.1007/s10584-008-9490-1, URL `http://dx.doi.org/10.1007/s10584-008-9490-1`.

Cornish, D. A. and G. L. Smit, 1995: The correlation between environmental factors and the reproduction of Oreochromis mossambicus. *Water SA*, **21**, 259–263.

Cripps, G., S. Widdicombe, J. I. Spicer, and H. S. Findlay, 2013: Biological impacts of enhanced alkalinity in Carcinus maenas. *Marine Pollution Bulletin*, **71 (1 - 2)**, 190 – 198, doi:10.1594/PANGAEA.829880, URL `http://doi.pangaea.de/10.1594/PANGAEA.829880`.

Crutzen, P. J., 2006: Albedo enhancement by stratospheric sulfur injections: A contribution to resolve a policy dilemma? *Climatic Change*, **77 (3)**, 211, doi:10.1007/s10584-006-9101-y, URL `http://dx.doi.org/10.1007/s10584-006-9101-y`.

Dwyer, J., 2014: *Projected Changes in the Annual Cycle of Surface Temperature and Precipitation Due to Greenhouse Gas Increases.* Columbia University Academic Commons, doi:10.7916/D8CN7248, URL `https://books.google.de/books?id=DQhb66oz0wEC`.

Dwyer, J. G., M. Biasutti, and A. H. Sobel, 2012: Projected changes in the seasonal cycle of surface temperature. *Journal of Climate*, **25 (18)**, 6359–6374, doi: 10.1175/JCLI-D-11-00741.1.

Egleston, E. S., C. L. Sabine, and F. M. M. Morel, 2010: Revelle revisited: Buffer factors that quantify the response of ocean chemistry to changes in DIC and alkalinity. *Global Biogeochemical Cycles*, **24 (1)**, doi:10.1029/2008GB003407, URL `http://dx.doi.org/10.1029/2008GB003407`.

Feng, E. Y., D. P. Keller, W. Koeve, and A. Oschlies, 2016: Could artificial ocean alkalinization protect tropical coral ecosystems from ocean acidification? *Environmental Research Letters*, **11 (7)**, URL `http://stacks.iop.org/1748-9326/11/i=7/a=074008`.

Fiorillo, I., S. Rossi, V. Alva, J. M. Gili, and P. J. López-González, 2013: Seasonal cycle of sexual reproduction of the Mediterranean soft coral Alcyonium acaule (Anthozoa, Octocorallia). *Marine Biology*, **160 (3)**, 719–728, doi:10.1007/s00227-012-2126-z, URL `http://dx.doi.org/10.1007/s00227-012-2126-z`.

Gehlen, M., et al., 2014: Projected pH reductions by 2100 might put deep North Atlantic biodiversity at risk. *Biogeosciences*, **11 (23)**, 6955–6967, doi:10.5194/bg-11-6955-2014.

Gilbert, R. O., 1987: 6.5 Sens̀ nonparametric estimator of slope. Statistical Methods for Environmental Pollution Monitoring, 217–219 pp.

Giorgetta, M. A., E. Manzini, E. Roeckner, M. Esch, and L. Bengtsson, 2006: Climatology and forcing of the quasi-biennial oscillation in the MAECHAM5

model. *Journal of Climate*, **19 (16)**, 3882–3901, doi:10.1175/JCLI3830.1, URL `http://dx.doi.org/10.1175/JCLI3830.1`.

Giorgetta, M. A., et al., 2013: Climate and carbon cycle changes from 1850 to 2100 in MPI-ESM simulations for the coupled model intercomparison project phase 5. *Journal of Advances in Modeling Earth Systems*, **5 (3)**, 572–597, doi: 10.1002/jame.20038, URL `http://dx.doi.org/10.1002/jame.20038`.

González, M. F. and T. Ilyina, 2016: Impacts of artificial ocean alkalinization on the carbon cycle and climate in earth system simulations. *Geophysical Research Letters*, **43 (12)**, 6493–6502, doi:10.1002/2016GL068576, URL `http://dx.doi.org/10.1002/2016GL068576`, 2016GL068576.

Govindasamy, B. and K. Caldeira, 2000: Geoengineering Earth's radiation balance to mitigate CO_2-induced climate change. *Geophysical Research Letters*, **27 (14)**, 2141–2144, doi:10.1029/1999GL006086, URL `http://dx.doi.org/10.1029/1999GL006086`.

Goyet, C. and A. Poisson, 1989: New determination of carbonic acid dissociation constants in seawater as a function of temperature and salinity. *Deep Sea Research Part A. Oceanographic Research Papers*, **36 (11)**, 1635 – 1654, doi:http://dx.doi.org/10.1016/0198-0149(89)90064-2, URL `http://www.sciencedirect.com/science/article/pii/0198014989900642`.

Gröger, M. and U. Mikolajewicz, 2011: Note on the CO_2 air-sea gas exchange at high temperatures. *Ocean Modelling*, **39 (3 - 4)**, 284 – 290, doi:http://dx.doi.org/10.1016/j.ocemod.2011.05.003, URL `http://www.sciencedirect.com/science/article/pii/S1463500311000886`.

Haigh, R., D. Ianson, C. A. Holt, H. E. Neate, and A. M. Edwards, 2015: Effects of Ocean Acidification on Temperate Coastal Marine Ecosystems and Fisheries in the Northeast Pacific. *PLOS ONE*, **10 (2)**, e0117533, doi:10.1371/journal.pone.0117533, URL `http://www.ncbi.nlm.nih.gov/pmc/articles/PMC4324998/`.

Hartmann, J., A. J. West, P. Renforth, P. Köhler, C. L. De La Rocha, D. A. Wolf-Gladrow, H. H. Dürr, and J. Scheffran, 2013: Enhanced chemical weathering as a geoengineering strategy to reduce atmospheric carbon dioxide, supply nutrients, and mitigate ocean acidification. *Reviews of Geophysics*, **51 (2)**, 113–149.

Hauck, J., P. Köhler, D. Wolf-Gladrow, and C. Völker, 2016: Iron fertilisation and century-scale effects of open ocean dissolution of olivine in a simulated CO_2 removal experiment. *Environmental Research Letters*, **11 (2)**, 024 007, URL `http://stacks.iop.org/1748-9326/11/i=2/a=024007`.

Hauck, J. and C. Völker, 2015: Rising atmospheric CO_2 leads to large impact of biology on Southern Ocean CO_2 uptake via changes of the Revelle factor. *Geophysical Research Letters*, **42 (5)**, 1459–1464, doi:10.1002/2015GL063070, URL `http://dx.doi.org/10.1002/2015GL063070`, 2015GL063070.

Heinze, C., E. Maier-Reimer, A. M. E. Winguth, and D. Archer, 1999: A global oceanic sediment model for long-term climate studies. *Global Biogeochemical Cycles*, **13 (1)**, 221–250, doi:10.1029/98GB02812, URL `http://dx.doi.org/10.1029/98GB02812`.

Heinze, C., E. Maier-Reimer, and K. Winn, 1991: Glacial pCO2 Reduction by the World Ocean: Experiments With the Hamburg Carbon Cycle Model. *Paleoceanography*, **6 (4)**, 395–430, doi:10.1029/91PA00489, URL `http://dx.doi.org/10.1029/91PA00489`.

Henson, S., H. Cole, C. Beaulieu, and A. Yool, 2013: The impact of global warming on seasonality of ocean primary production. *Biogeosciences*, **10 (6)**, 4357–4369, doi:10.5194/bg-10-4357-2013, URL `http://www.biogeosciences.net/10/4357/2013/`.

Hurtt, G. C., S. Frolking, M. G. Fearon, B. Moore, E. Shevliakova, S. Malyshev, S. W. Pacala, and R. A. Houghton, 2006: The underpinnings of land-use history: three centuries of global gridded land-use

transitions, wood-harvest activity, and resulting secondary lands. *Global Change Biology*, **12 (7)**, 1208–1229, doi:10.1111/j.1365-2486.2006.01150.x, URL http://dx.doi.org/10.1111/j.1365-2486.2006.01150.x.

Hurtt, G. C., et al., 2011: Harmonization of land-use scenarios for the period 1500-2100: 600 years of global gridded annual land-use transitions, wood harvest, and resulting secondary lands. *Climatic Change*, **109 (1)**, 117–161, doi:10.1007/s10584-011-0153-2, URL http://dx.doi.org/10.1007/s10584-011-0153-2.

Ilyina, T. and P. Friedlingstein, 2017: *World Climate Research Programme*. WCRP Grand Challenge: Carbon feedbacks in the climate system.

Ilyina, T., K. D. Six, J. Segschneider, E. Maier-Reimer, H. Li, and I. Núñez Riboni, 2013a: Global ocean biogeochemistry model HAMOCC: Model architecture and performance as component of the MPI-Earth system model in different CMIP5 experimental realizations. *Journal of Advances in Modeling Earth Systems*, **5 (2)**, 287–315, doi:10.1029/2012MS000178, URL http://dx.doi.org/10.1029/2012MS000178.

Ilyina, T., D. Wolf-Gladrow, G. Munhoven, and C. Heinze, 2013b: Assessing the potential of calcium-based artificial ocean alkalinization to mitigate rising atmospheric CO_2 and ocean acidification. *Geophysical Research Letters*, **40**, 1–6, doi: 10.1002/2013GL057981, URL http://doi.wiley.com/10.1002/2013GL057981.

Ilyina, T. and R. E. Zeebe, 2012: Detection and projection of carbonate dissolution in the water column and deep-sea sediments due to ocean acidification. *Geophysical Research Letters*, **39 (6)**, doi:10.1029/2012GL051272, URL http://dx.doi.org/10.1029/2012GL051272, l06606.

IPCC, 2012: Meeting Report of the Intergovernmental Panel on Climate Change Expert Meeting on Geoengineering. Potsdam Institute for Climate Impact Research, Potsdam, Germany, 99 pp.

140

IPCC, 2013: Climate Change 2013: The Physical Science Basis. Contribution of Working Group I to the Fifth Assessment Report of the Intergovernmental Panel on Climate Change. *Cambridge University Press*, doi: 10.1017/CBO9781107415324.

Jenkinson, D. S., D. E. Adams, and A. Wild, 1991: Model estimates of CO_2 emissions from soil in response to global warming. *Nature*, **351**, 304–306, doi: 10.1038/351304a0.

Ji, R., M. Edwards, D. L. Mackas, J. A. Runge, and A. C. Thomas, 2010: Marine plankton phenology and life history in a changing climate: current research and future directions. *Journal of Plankton Research*, **32 (10)**, 1355–1368, doi:10.1093/plankt/fbq062, URL http://plankt.oxfordjournals.org/content/32/10/1355.abstract.

Jones, A., et al., 2013: The impact of abrupt suspension of solar radiation management (termination effect) in experiment G2 of the geoengineering model intercomparison project (GeoMIP). *Journal of Geophysical Research: Atmospheres*, **118 (17)**, 9743–9752, doi:10.1002/jgrd.50762, URL http://dx.doi.org/10.1002/jgrd.50762.

Joos, F. and R. Spahni, 2008: Rates of change in natural and anthropogenic radiative forcing over the past 20,000 years. *Proceedings of the National Academy of Sciences*, **105 (5)**, 1425–1430, doi:10.1073/pnas.0707386105, URL http://www.pnas.org/content/105/5/1425.abstract.

Jungclaus, J. H., et al., 2013: Characteristics of the ocean simulations in the Max Planck Institute Ocean Model (MPIOM) the ocean component of the MPI-Earth system model. *Journal of Advances in Modeling Earth Systems*, **5 (2)**, 422–446, doi:10.1002/jame.20023, URL http://dx.doi.org/10.1002/jame.20023.

Kamenos, N. A., et al., 2013: Coralline algal structure is more sensitive to rate, rather than the magnitude, of ocean acidification. *Global*

Change Biology, **19 (12)**, 3621–3628, doi:10.1111/gcb.12351, URL
http://dx.doi.org/10.1111/gcb.12351.

Keller, D. P., E. Y. Feng, and A. Oschlies, 2014: Potential climate engineering effectiveness and side effects during a high carbon dioxide-emission scenario. *Nature Communications*, **5**, doi:10.1038/ncomms4304, URL http://dx.doi.org/10.1038/ncomms4304.

Kendall, M., 1975: Rank correlation methods. *Charles Griffin*.

Kheshgi, H. S., 1995: Sequestering atmospheric carbon dioxide by increasing ocean alkalinity. *Energy*, **20 (9)**, 915–922.

King, A. W., W. M. Post, and S. D. Wullschleger, 1997: The potential response of terrestrial carbon storage to changes in climate and atmospheric CO_2. *Climatic Change*, **35 (2)**, 199–227, doi:10.1023/A:1005317530770, URL http://dx.doi.org/10.1023/A:1005317530770.

Knorr, W., 2000: Annual and interannual CO_2 exchanges of the terrestrial biosphere: process-based simulations and uncertainties. *Global Ecology and Biogeography*, **9 (3)**, 225–252, doi:10.1046/j.1365-2699.2000.00159.x, URL http://dx.doi.org/10.1046/j.1365-2699.2000.00159.x.

Köhler, P., J. F. Abrams, C. Völker, J. Hauck, and D. Wolf-Gladrow, 2013: Geoengineering impact of open ocean dissolution of olivine on atmospheric CO_2, surface ocean pH and marine biology. *Environmental Research Letters*, **8 (1)**, 014 009, doi:10.1088/1748-9326/8/1/014009.

Le Quéré, C., et al., 2015: Global carbon budget 2015. *Earth System Science Data*, **7 (2)**, 349–396, doi:10.5194/essd-7-349-2015, URL http://www.earth-syst-sci-data.net/7/349/2015/.

Lenzen, M., 2011: Global warming effect of leakage from CO_2 storage. *Critical Reviews in Environmental Science and Technol-*

ogy, **41 (24)**, 2169–2185, doi:10.1080/10643389.2010.497442, URL `http://dx.doi.org/10.1080/10643389.2010.497442`.

Limsuwan, C., 2005: Cultivo intensivo de camaron blanco. *Boletin Nicovita, Edicion Octubre-Diciembre.*

Lochte, K., H. Ducklow, M. Fasham, and C. Stienen, 1993: Plankton succession and carbon cycling at 47°N 20°W during the JGOFS North Atlantic Bloom Experiment. *Deep Sea Research Part II: Topical Studies in Oceanography*, **40 (1)**, 91 – 114, doi:http://dx.doi.org/10.1016/0967-0645(93)90008-B, URL `http://www.sciencedirect.com/science/article/pii/096706459390008B`.

Maier-Reimer, E., 1993: Geochemical cycles in an ocean general circulation model. Preindustrial tracer distributions. *Global Biogeochemical Cycles*, **7 (3)**, 645–677, doi:10.1029/93GB01355, URL `http://dx.doi.org/10.1029/93GB01355`.

Maier-Reimer, E. and K. Hasselmann, 1987: Transport and storage of CO_2 in the ocean - an inorganic ocean-circulation carbon cycle model. *Climate Dynamics*, **2 (2)**, 63–90, doi:10.1007/BF01054491, URL `http://dx.doi.org/10.1007/BF01054491`.

Maier-Reimer, E., I. Kriest, J. Segschneider, and P. Wetzel, 2005: The Hamburg oceanic carbon cycle circulation model HAMOCC5.1-Technical Description Release 1.1, Tech. Rep. 14. *Reports on Earth System Science, Max Planck Institute for Meteorology, Hamburg, Germany.*

Mann, H. B., 1945: Nonparametric tests against trend. *Econometrica*, **13 (3)**, 245–259, URL `http://www.jstor.org/stable/1907187`.

Mann, M. E. and J. Park, 1996: Greenhouse warming and changes in the seasonal cycle of temperature: Model versus observations. *Geophysical Research Letters*, **23 (10)**, 1111–1114, doi:10.1029/96GL01066, URL `http://dx.doi.org/10.1029/96GL01066`.

Marsland, S., H. Haak, J. Jungclaus, M. Latif, and F. Roeske, 2003: The Max-Planck-Institute global ocean/sea ice model with orthogonal curvilinear coordinates. *Ocean Modelling*, **5 (2)**, 91 – 127, doi:http://dx.doi.org/10.1016/S1463-5003(02)00015-X, URL `http://www.sciencedirect.com/science/article/pii/S146350030200015X`.

McNeil, B. I. and T. P. Sasse, 2016: Future ocean hypercapnia driven by anthropogenic amplification of the natural CO_2 cycle. *Nature*, **529 (7586)**, 383–386, doi:10.1038/nature16156, URL `http://dx.doi.org/10.1038/nature16156`.

Meyer, J. and U. Riebesell, 2015: Reviews and syntheses: Responses of coccolithophores to ocean acidification: a meta-analysis. *Biogeosciences*, **12 (6)**, 1671–1682, doi:10.5194/bg-12-1671-2015, URL `http://www.biogeosciences.net/12/1671/2015/`.

Morse, J. W. and S. He, 1993: Influences of T, S and pCO2 on the pseudo-homogeneous precipitation of $CaCO_3$ from seawater: Implications for whiting formation. *Marine Chemistry*, **41 (4)**, 291 – 297, doi:http://dx.doi.org/10.1016/0304-4203(93)90261-L, URL `http://www.sciencedirect.com/science/article/pii/030442039390261L`.

Mucci, A., 1983: The solubility of calcite and aragonite in seawater at various salinities, temperatures, and one atmosphere total pressure. *American Journal of Science*, **283 (7)**, 780–799, doi:doi:10.2475/ajs.283.7.780.

National Research Council, 2015a: Climate Intervention: Carbon Dioxide Removal and Reliable Sequestration. Washington, DC.

National Research Council, 2015b: Climate Intervention: Reflecting Sunlight to Cool Earth. Washington, DC.

Niemeier, U., H. Schmidt, K. Alterskjær, and J. E. Kristjansson, 2013: Solar irradiance reduction via climate engineering: Impact of different techniques

on the energy balance and the hydrological cycle. *Journal of Geophysical Research: Atmospheres*, **118 (21)**, 11,905–11,917, doi:10.1002/2013JD020445, URL `http://dx.doi.org/10.1002/2013JD020445`.

Notz, D., F. A. Haumann, H. Haak, J. H. Jungclaus, and J. Marotzke, 2013: Arctic sea-ice evolution as modeled by Max Planck Institute for Meteorology's Earth system model. *Journal of Advances in Modeling Earth Systems*, **5 (2)**, 173–194, doi:10.1002/jame.20016, URL `http://dx.doi.org/10.1002/jame.20016`.

Partanen, A.-I., D. P. Keller, H. Korhonen, and H. D. Matthews, 2016: Impacts of sea spray geoengineering on ocean biogeochemistry. *Geophysical Research Letters*, **43 (14)**, 7600–7608, doi:10.1002/2016GL070111, URL `http://dx.doi.org/10.1002/2016GL070111`, 2016GL070111.

Platt, T., C. Fuentes-Yaco, and K. T. Frank, 2003: Marine ecology: Spring algal bloom and larval fish survival. *Nature*, **423 (6938)**, 398–399, URL `http://dx.doi.org/10.1038/423398b`.

Pörtner, H.-O., et al., 2014: Ocean systems. Cambridge University Press, Cambridge, United Kingdom and New York, NY, USA, 411–484 pp.

Quintero, I. and J. J. Wiens, 2013: Rates of projected climate change dramatically exceed past rates of climatic niche evolution among vertebrate species. *Ecology Letters*, **16 (8)**, 1095–1103, doi:10.1111/ele.12144, URL `http://dx.doi.org/10.1111/ele.12144`.

Redi, M. H., 1982: Oceanic isopycnal mixing by coordinate rotation. *Journal of Physical Oceanography*, **12 (10)**, 1154–1158.

Reick, C. H., T. Raddatz, V. Brovkin, and V. Gayler, 2013: Representation of natural and anthropogenic land cover change in MPI-ESM. *Journal of Advances in Modeling Earth Systems*, **5 (3)**, 459–482, doi:10.1002/jame.20022, URL `http://dx.doi.org/10.1002/jame.20022`.

Riebesell, U., I. Zondervan, B. Rost, P. D. Tortell, R. E. Zeebe, and F. M. M. Morel, 2000: Reduced calcification of marine plankton in response to increased atmospheric CO_2. *Nature*, **407 (6802)**, 364–367, doi:10.1038/35030078, URL `http://dx.doi.org/10.1038/35030078`.

Sarmiento, J. L., T. M. C. Hughes, R. J. Stouffer, and S. Manabe, 1998: Simulated response of the ocean carbon cycle to anthropogenic climate warming. *Nature*, **393 (6682)**, 245–249, doi:10.1038/30455, URL `http://dx.doi.org/10.1038/30455`.

Schmidt, G. A., C. M. Bitz, U. Mikolajewicz, and L.-B. Tremblay, 2004: Ice-ocean boundary conditions for coupled models. *Ocean Modelling*, **7 (1-2)**, 59 – 74, doi:http://dx.doi.org/10.1016/S1463-5003(03)00030-1, URL `http://www.sciencedirect.com/science/article/pii/S1463500303000301`.

Schmidt, H., et al., 2012: Solar irradiance reduction to counteract radiative forcing from a quadrupling of CO_2: climate responses simulated by four Earth system models. *Earth System Dynamics*, **3 (1)**, 63–78, doi:10.5194/esd-3-63-2012, URL `http://www.earth-syst-dynam.net/3/63/2012/`.

Schneck, R., C. H. Reick, and T. Raddatz, 2013: Land contribution to natural CO_2 variability on time scales of centuries. *Journal of Advances in Modeling Earth Systems*, **5 (2)**, 354–365, doi:10.1002/jame.20029, URL `http://dx.doi.org/10.1002/jame.20029`.

Schneider, B., et al., 2008: Climate-induced interannual variability of marine primary and export production in three global coupled climate carbon cycle models. *Biogeosciences*, **5 (2)**, 597–614, doi:10.5194/bg-5-597-2008, URL `http://www.biogeosciences.net/5/597/2008/`.

Simmons, A. J. and D. M. Burridge, 1981: An energy and angular-momentum conserving vertical finite-difference scheme and hybrid vertical coordinates. *Monthly Weather Review*, **109 (4)**, 758–766.

Simmons, A. J., D. M. Burridge, M. Jarraud, C. Girard, and W. Wergen, 1989: The ECMWF medium-range prediction models development of the numerical formulations and the impact of increased resolution. *Meteorology and Atmospheric Physics*, **40 (1)**, 28–60, doi:10.1007/BF01027467, URL http://dx.doi.org/10.1007/BF01027467.

Simmons, A. J. and C. Jiabin, 1991: The calculation of geopotential and the pressure gradient in the ECMWF atmospheric model: Influence on the simulation of the polar atmosphere and on temperature analyses. *Quarterly Journal of the Royal Meteorological Society*, **117 (497)**, 29–58, doi:10.1002/qj.49711749703, URL http://dx.doi.org/10.1002/qj.49711749703.

Six, K. D. and E. Maier-Reimer, 1996: Effects of plankton dynamics on seasonal carbon fluxes in an ocean general circulation model. *Global Biogeochemical Cycles*, **10 (4)**, 559–583, doi:10.1029/96GB02561, URL http://dx.doi.org/10.1029/96GB02561.

Sobel, A. H. and S. J. Camargo, 2011: Projected future seasonal changes in tropical summer climate. *Journal of Climate*, **24 (2)**, 473–487, doi: 10.1175/2010JCLI3748.1, URL http://dx.doi.org/10.1175/2010JCLI3748.1.

Sonntag, S., M. F. González, T. Ilyina, D. Kracher, J. E. M. S. Nabel, J. Pongratz, C. H. Reick, and H. Schmidt, submitted: Quantifying and comparing effects of climate engineering methods on the Earth system, submitted to *Earth's Future*.

Sonntag, S., J. Pongratz, C. H. Reick, and H. Schmidt, 2016: Reforestation in a high-CO_2 world - Higher mitigation potential than expected, lower adaptation potential than hoped for. *Geophysical Research Letters*, **43 (12)**, 6546–6553, doi:10.1002/2016GL068824, URL http://dx.doi.org/10.1002/2016GL068824, 2016GL068824.

Steiner, N. S., J. R. Christian, K. D. Six, A. Yamamoto, and M. Yamamoto-Kawai, 2014: Future ocean acidification in the Canada Basin and surround-

ing Arctic Ocean from CMIP5 Earth system models. *Journal of Geophysical Research: Oceans*, **119 (1)**, 332–347, doi:10.1002/2013JC009069, URL `http://dx.doi.org/10.1002/2013JC009069`.

Stevens, B., et al., 2013: Atmospheric component of the MPI-M Earth system model: ECHAM6. *Journal of Advances in Modeling Earth Systems*, **5 (2)**, 146–172, doi:10.1002/jame.20015, URL `http://dx.doi.org/10.1002/jame.20015`.

Stier, P., et al., 2005: The aerosol-climate model ECHAM5-HAM. *Atmospheric Chemistry and Physics*, **5 (4)**, 1125–1156, doi:10.5194/acp-5-1125-2005, URL `http://www.atmos-chem-phys.net/5/1125/2005/`.

Stine, A. R. and P. Huybers, 2012: Changes in the seasonal cycle of temperature and atmospheric circulation. *Journal of Climate*, **25 (21)**, 7362–7380, doi:10.1175/JCLI-D-11-00470.1, URL `http://dx.doi.org/10.1175/JCLI-D-11-00470.1`.

Stone, E. J., J. A. Lowe, and K. P. Shine, 2009: The impact of carbon capture and storage on climate. *Energy Environ. Sci.*, **2**, 81–91, doi:10.1039/B807747A, URL `http://dx.doi.org/10.1039/B807747A`.

Sundby, S., K. F. Drinkwater, and O. S. Kjesbu, 2016: The North Atlantic Spring-Bloom System - Where the Changing Climate Meets the Winter Dark. *Frontiers in Marine Science*, **3**, 28, doi:10.3389/fmars.2016.00028, URL `http://journal.frontiersin.org/article/10.3389/fmars.2016.00028`.

Takahashi, T., W. S. Broecker, and S. Langer, 1985: Redfield ratio based on chemical data from isopycnal surfaces. *Journal of Geophysical Research: Oceans*, **90 (C4)**, 6907–6924, doi:10.1029/JC090iC04p06907, URL `http://dx.doi.org/10.1029/JC090iC04p06907`.

Takahashi, T., et al., 2009: Climatological mean and decadal change in surface ocean pCO2, and net sea-air CO_2 flux over the global oceans.

Deep-Sea Research II 56(8-10), 554–577, doi:10.1016/j.dsr2.2008.12.009, URL `http://dx.doi.org/10.1016/j.dsr2.2008.12.009`.

Taylor, K. E., R. J. Stouffer, and G. A. Meehl, 2012: An overview of CMIP5 and the experiment design. *Bulletin of the American Meteorological Society*, **93 (4)**, 485–498, doi:10.1175/BAMS-D-11-00094.1, URL `http://dx.doi.org/10.1175/BAMS-D-11-00094.1`.

The Royal Society, 2009: Geoengineering the climate: science, governance and uncertainty. London.

The United States Geological Survey, 2016: *Mineral commodity summaries 2016*. U.S. Geological Survey, 202 pp., URL `http://dx.doi.org/10.3133/70140094`.

Tjiputra, J. F., A. Grini, and H. Lee, 2016: Impact of idealized future stratospheric aerosol injection on the large-scale ocean and land carbon cycles. *Journal of Geophysical Research: Biogeosciences*, **121 (1)**, 2–27, doi:10.1002/2015JG003045, URL `http://dx.doi.org/10.1002/2015JG003045`, 2015JG003045.

Townsend, A. R., P. M. Vitousek, and E. A. Holland, 1992: Tropical soils could dominate the short-term carbon cycle feedbacks to increased global temperatures. *Climatic Change*, **22 (4)**, 293–303, doi:10.1007/BF00142430, URL `http://dx.doi.org/10.1007/BF00142430`.

Valcke, S., 2013: The OASIS3 coupler: a European climate modelling community software. *Geoscientific Model Development*, **6 (2)**, 373–388, doi:10.5194/gmd-6-373-2013, URL `http://www.geosci-model-dev.net/6/373/2013/`.

van Vuuren, D., et al., 2011: The representative concentration pathways: an overview. *Climatic Change*, **109 (1-2)**, 5–31, doi:10.1007/s10584-011-0148-z, URL `http://dx.doi.org/10.1007/s10584-011-0148-z`.

Vancoppenolle, M., L. Bopp, G. Madec, J. Dunne, T. Ilyina, P. R. Halloran, and N. Steiner, 2013: Future Arctic Ocean primary productivity

from CMIP5 simulations: Uncertain outcome, but consistent mechanisms. *Global Biogeochemical Cycles*, **27 (3)**, 605–619, doi:10.1002/gbc.20055, URL `http://dx.doi.org/10.1002/gbc.20055`.

Wanninkhof, R., 1992: Relationship between wind speed and gas exchange over the ocean. *Journal of Geophysical Research: Oceans*, **97 (C5)**, 7373–7382, doi: 10.1029/92JC00188, URL `http://dx.doi.org/10.1029/92JC00188`.

Weiss, R., 1974: Carbon dioxide in water and seawater: the solubility of a non-ideal gas. *Marine Chemistry*, **2 (3)**, 203 – 215, doi:http://dx.doi.org/10.1016/0304-4203(74)90015-2, URL `http://www.sciencedirect.com/science/article/pii/0304420374900152`.

Williamson, P. and C. Turley, 2012: Ocean acidification in a geo-engineering context. *Philosophical Transactions of the Royal Society of London A: Mathematical, Physical and Engineering Sciences*, **370 (1974)**, 4317–4342, doi:10.1098/rsta.2012.0167, URL `http://rsta.royalsocietypublishing.org/content/370/1974/4317`.

Wolf-Gladrow, D. A., R. E. Zeebe, C. Klaas, A. Körtzinger, and A. G. Dickson, 2007: Total alkalinity: the explicit conservative expression and its application to biogeochemical processes . *Marine Chemistry*, **106 (1-2)**, 287 – 300.

Wolff, J. O., E. Maier-Reimer, and S. Legutke, 1997: The Hamburg Ocean Primitive Equation Model HOPE Tech. Rep. *German Climate Computer Center (DKRZ), Hamburg, Germany*, **13**, 98.

W.R.Wallace, D., 2001: Storage and transport of excess CO_2 in the oceans:The JGOFS/WOCE global CO_2 survey . *Ocean Circulation and Climate: Observing and Modelling the Global Ocean*, J. C. Gerold Siedler and J. Gould, Eds., Academic Press, International Geophysics, Vol. 77, 489 – 521, doi:http://dx.doi.org/10.1016/S0074-6142(01)80136-4, URL `http://www.sciencedirect.com/science/article/pii/S0074614201801364`.

Wurts, W. A. and R. M. Durborow, 1992: *Interactions of pH, carbon dioxide, alkalinity in fish ponds*. 464, Southern Regional Aquaculture Center Publication.

Zeebe, R. and D. Wolf-Gladrow, 2001: *CO_2 in Seawater: Equilibrium, Kinetics, Isotopes*, Vol. 65. Elsevier.

Acknowledgments

I wish to thank my advisor Tatiana Ilyina for her patience, support and guidance. This research would not have been possible without her help. I have gained invaluable experience and knowledge working with her during these years. I am grateful to my co-advisor Johanna Baehr for her insightful comments, encouragement and support when most needed. I thank Prof. Graßl for being part of my advisory panel, I could not have imagined having a better panel chair for my PhD project. I also want to express my gratitude to all members of the MPI and my working group, especially to Irene Stemmler, Katharina Six, Sebastian Sonntag and Helmuth Haak. Without their help and support, I would not be writing these last few words today. I wish to express my most sincere gratitude and appreciation to Antje Weitz, she became an indispensable friend in my life during the last years. I thank my IMPRS fellows for the stimulating discussions and for all the fun we have had. Special thanks goes to my friend Irina, who brought me great joy during these last six years and supported me in tough times. No words can express how lucky I feel I am to have shared office with my friend Chris. Four years ago, I wanted to go to Australia but instead, the best of Australia came to my life. On my way to my first day of university, I met an amazing unique person who throughout the years became my soulmate. Noe, thanks for all these many years of true friendship. I have been blessed with a loving family, awesome friends and a wonderful beautiful mother. This dissertation is dedicated to them.

Appendix A

The Max Planck Institute Earth System Model

Our tool is the Max Planck Institute Earth System Model in its low resolution version (MPI-ESM-LR, Fig 2.1) with the configuration used in the Coupled Model Intercomparison Project phase 5 (CMIP5) (Giorgetta et al. 2013). The coupled system MPI-ESM includes two general circulation models: ECHAM6 (Stevens et al. 2013) which simulates the atmosphere and MPIOM (Jungclaus et al. 2013) for the ocean. This version of ECHAM6 has a horizontal grid resolution of approximately 1.9°on a Gaussian grid and 47 pressure levels. MPIOM has a nominal resolution of 1.5° (viz. around 15 km grid spacing in Greenland and 185 km in the tropical Pacific. In the vertical, MPIOM uses a z-grid with 40 unevenly spaced levels which increasing depths which range from 12 meters (near the surface) to several hundred meters (in the deep ocean). JSBACH (Reick et al. 2013) is an integral component of ECHAM6 (running with the same horizontal resolution) and it constitutes the land submodel of MPI-ESM. JSBACH simulates biogeophysical and biogeochemical processes and produces the boundary conditions over land at the lower atmosphere. Biogeochemical tracers in the water column of the ocean and sediment layers are simulated with the submodule HAMOCC (Ilyina et al. 2013a) which resolution is the same than the ocean circulation field defined by MPIOM. The MPI-ESM uses
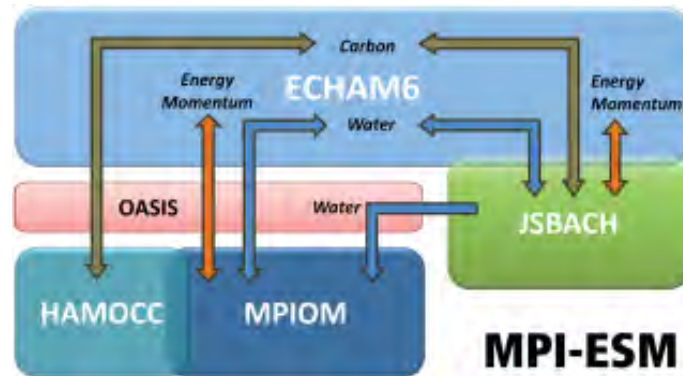
Figure A.1: Schematic diagram of the Max Planck Institute Earth System Model (after Giorgetta et al., 2013). Each box represents a model component: The atmospheric general circulation model ECHAM6 is coupled to the land and vegetation model JSBACH. The ocean general circulation model MPIOM contains the marine biogeochemistry model HAMOCC. The coupler program OASIS deals with the aggregation, interpolation and the daily exchange of state variables and fluxes for energy, momentum, H_2O and CO_2.

a coupler program (OASIS) that solves the aggregation, interpolation and the exchange of several variables such as energy momentum, H_2O and CO_2 between the different subcomponents of the coupled system (Valcke 2013). The model configuration used in this research operates with fully coupled interactive carbon cycle. A detailed description of the main components of the MPI-ESM is given in the following subsections and references therein.

A.1 Atmospheric Module ECHAM6

The atmospheric component ECHAM6 couples diabatic processes and large-scale circulations (Stevens et al. 2013). This atmospheric module includes a dry spectral-transform dynamical core and physical parameterizations representing (between other processes) diabatic processes, distribution of aerosols and trace gases, optical

properties of gases, land-surface properties and dynamical spectral solar irradiance. The spatial distribution of scalar variables (different than temperature and surface pressure) is defined by its transport model. Temperature and surface pressure are the thermodynamic coordinates used in the primitive equations which are discretized using a mixed finite-difference/spectral scheme. The temporal discretization of the primitive equations follows a scheme centered in time where an Asselin filter damps computational modes and semi-implicit corrections are implemented in order to facilitate computation with larger time steps. Spatial differences between the model layers that form spherical surfaces are represented following the spectral-transform method (Simmons et al. 1989). Discretization of the vertical dimension follows (Simmons and Burridge 1981) using on a Lorenz grid the hybrid sigma-pressure coordinates. The definition of vertical advection conserves potential and kinetic energy and the formulation of pressure gradients is defined so that it conserves angular momentum and it reduces inaccuracies over steep topography (Simmons and Jiabin 1991). In order to guarantee model stability, horizontal diffusion is required and its effects are minimized by modifying the order of the diffusion operator which limits the strongest impacts to the highest levels of the model. A flux-form semi-Lagrangian scheme is used for the transport of tracers. Paramerizations of physical processes are needed because the coarse grid resolution does not allow for their explicit representation. This is the case for the vertical mixing, which is defined as the combination of several processes: dynamics of wall-bounded turbulent flows defined through the parameterizations of the boundary and surface layers; convection and free-turbulent dynamics; and different mechanisms that simulate the transfer of momentum by gravity waves due to surface-flow interaction or atmospheric perturbations. The representation of cloud processes at smaller scales than those of the model grid uses a humidity distribution function scheme. The version of ECHAM6 used does not allow for an interactive representation of aerosols and therefore the effect of aerosols in clouds remains constant over time. The rapid radiation transfer models optimized for general circulation modelling (RRTM-G) describes the radiative transfer in the short and longwave ranges of the electromagnetic spectrum with the optical properties being updated every 2 hours. Rescaling of short and longwave

irradiances are performed as a function (respectively) of the zenith angle and on the surface temperature in time steps shorter than 2 hours. The optical properties of the surrounding medium of the radiation define the evolution of the radiative transfer. These optical properties are, in turn, described by the distribution of gases, airborne particles and condensates. Surface albedo over land-surfaces follows (Brovkin et al. 2013). Over ocean the parameterization accounts for the albedo dependency on the zenith angle and the different contributions from different ranges of the shortwave range of the electromagnetic spectrum in case of perpendicular solar radiation. The process of river runoff is interactively solved within a land hydrology submodule included in ECHAM6. There is a sea ice submodel within ECHAM6 that provides (at each atmospheric time-step) the boundary conditions of surface temperature and albedo according to the atmospheric state.

A.2 Ocean Module MPIOM

The ocean and sea ice component (MPIOM) is the free-surface ocean general circulation model of the coupled system MPI-ESM. In the horizontal dimension it is designed on an Arakawa-C grid and z-grid in the vertical. The MPIOM computes the 3D primitive equations using the hydrostatic and Boussinesq approximations. Horizontal diffusion is defined using an isopycnal formulation after (Redi 1982), with a variable diffusion coefficient determined by the grid spacing and proportional to the local isopycnal diffusion. The transport of tracers by eddies are not explicitly resolved due to the coarse model grid. Mixing due to turbulent flows in the mixed layer is simulated as a function of the wind speed, ocean depth and potential density difference to the surface (Marsland et al. 2003). Scalar tracers are advected using a second-order total variation diminishing formulation, including an advective slope-convection scheme so that statically unstable flows over sills and shelves are better represented (Marsland et al. 2003). Bottom topography is described using a partial-step formulation (Wolff et al. 1997). The ocean version used here is GR1.5 that has two poles, one located over the Antarctica and another over south-

ern Greenland. The nominal resolution of GR1.5 is 1.5° which yields to a varying grid spacing that ranges from a minimum of 15 km in Greenland to a maximum of 185 km around the tropical Pacific. The decreasing grid size towards the poles offers the advantage of a relatively fine resolution over regions where deepwater formation occurs. Atmosphere and ocean coupling occurs each 24 (model-)hours and without flux adjustments via the coupler OASIS (Valcke 2013). The freshwater fluxes that result from river runoff are passed to the ocean as part of the precipitation field computed in ECHAM6. Thus, only the upper grid cells of MPIOM are affected by river discharge.

The sea ice model included in MPIOM (Wolff et al. 1997; Marsland et al. 2003; Notz et al. 2013) computes the thermodynamic-dynamic sea ice of sea ice and ice thickness using a subgrid-scale formulation of the grid cell that is covered or free of ice. Sea ice dynamic is defined using a viscous-plastic rheology whilst sea ice thermodynamic is parameterized with a simplified zero-layer model. Snow accumulation effects and snow ice transformation are also taken into account with an assumed constant sea ice salinity of 5 g/kg (any excess salt is kept by the ocean layer below). The mass balance of ice sheets is treated in a simplified way, converting precipitation minus evaporation over the glaciers immediately into surface runoff.

The simulated sea ice has not intrinsic heat capacity leading to potential bias in the growth and decay of seasonal sea ice. Sea ice temperature at the surface is computed using a flux balance that considers conductive heat through the ice and radiative atmospheric fluxes provided to MPIOM via the coupler OASIS (Valcke 2013). In case that the sea ice surface temperature is higher than 0°C the sea ice melts using this surplus energy and releasing water to the associated ocean grid cell. Ice thickness at the ice-seawater interface varies according to the balance between the conductive heat flux across the ice and the heat flux from the ocean (Schmidt et al. 2004) where the excess of heat melts the sea ice, similar to the parameterization used for the sea ice surface.
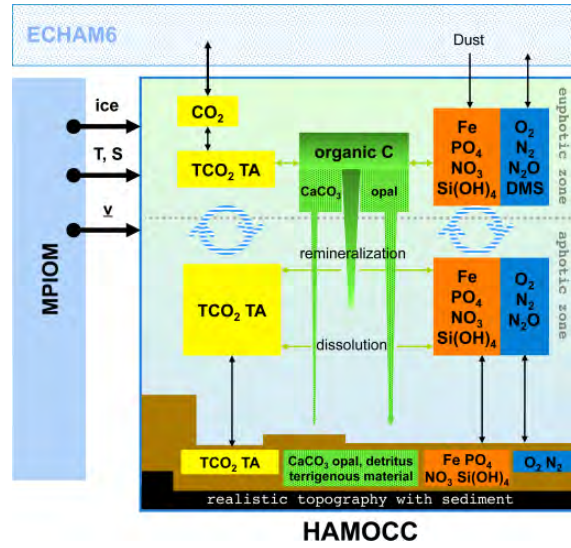
Figure A.2: Schematic diagram of the Hamburg Ocean Carbon Cycle (HAMOCC) (after Ilyina et al., 2013) used to simulate the global ocean biogeochemistry. The distribution of the tracer concentrations is determined by the 3D flow field provided by MPIOM, freshwater fluxes, precipitation/evaporation, biogeochemical processes and air-sea exchange.

A.3 Ocean Biogeochemistry HAMOCC

Biogeochemical tracers in the ocean water column and sediments are simulated with the model Hamburg Ocean Carbon Cycle (HAMOCC version 5.2, Fig 2.2) (Ilyina et al. 2013a), which is embedded in MPIOM and therefore has the same 1.5° horizontal resolution and 40 vertical levels of increasing depths. The relevant processes and parameterizations in the context of this study will be here described and a thorough description of HAMOCC can be found in Ilyina et al. (2013a) and Maier-Reimer et al. (2005). A total of 29 prognostic variables are simulated in this configuration of HAMOCC: 17 state variables within the water column and 12 in the sediments. Spatial and temporal distributions of the prognostic variables within the water column are governed by the flow field computed with MPIOM which also provides

the seawater temperature, pressure and salinity fields needed to calculate chemical constants and transformation rates in HAMOCC. Tracer concentrations also vary due to freshwater fluxes, precipitation/evaporation, biogeochemical processes and air-sea exchange for several gaseous tracers such as CO_2, O_2, DMS, N_2O, and N_2. Thermodynamic disequilibrium sets the gas exchange at the atmosphere-ocean interface. The gas transfer across the air-sea boundary is proportional to the difference in the concentrations of the gas between the atmosphere and the seawater with the exchange rate of the specific gas as proportionality constant. This exchange rate depends upon temperature and wind speed, and it is defined with the Schmidt number and the piston velocity following (Wanninkhof 1992). The temperature dependency in this parameterization has been modified for the gases CO_2 and DMS in order to avoid the bias occurring when seawater temperatures are higher than 30°C (under the approach of Wanninkhof the fit becomes negative above 42°C). Instead, the exchange rates parameters for CO_2 and DMS are defined following the approach of (Gröger and Mikolajewicz 2011). The atmospheric concentration of CO_2 is prognostically calculated by ECHAM6 and the partial pressure of seawater CO_2 is the ratio of the CO_2 concentration to its solubility SCO_2 (values given by Weiss (1974)). Atmospheric partial pressure of O_2 is prescribed as constant (preindustrial level) assuming a negligible decrease associated with the consumption of O_2 due to the fossil fuel combustion. Regarding other climate relevant gases such as DMS, N_2O and N_2, the atmospheric concentration of DMS is set to zero and therefore DMS release from the ocean does not influence the climate state. The content of N_2O in the atmosphere is its saturation value in seawater and the N_2 atmospheric concentration has a prescribed constant value. HAMOCC has a simplified marine ecosystem model nutrients-phytoplankton-zooplankton-detritus (NPZD) including 3 nutrients (phosphate, nitrate and iron) (Six and Maier-Reimer 1996). This submodel is a simplified formulation of the dynamics governing the interaction between nutrient distributions, different trophic levels of marine biota and dead organic matter (detritus). Within this submodel 7 variables are prognostically calculated: three types of nutrients (phosphate, nitrate and iron), one phytoplankton state variable, one zooplankton type, dissolved organic matter (DOM), and a single

compartment for sinking particulate organic matter. Primary production depends on temperature, light and the co-limitation of phosphorous (P), nitrate (N) and iron (Fe). Organic compounds have the same fixed stoichiometric ratio between carbon, (micro)nutrients and oxygen following the Redfield concept (Takahashi et al. 1985) (C:N:P:O_2=122:16:1:-172 and Fe:P=366e-6:1). Shell production is parameterized so that the phytoplankton detritus is splitted into opal shells and calcium carbonate ($CaCO_3$) shells. This is defined so that opal production occurs first than the production of $CaCO_3$ shells whereas silicate is available as observed in several field studies (e.g., Lochte et al. 1993). In areas where silicate is depleted, the production of $CaCO_3$ dominates. Our modeling approach provides a fair quantitative agreement with the observed distributions of nutrients and the seasonality of pCO2 at the ocean surface (e.g., Six and Maier-Reimer 1996; Schneider et al. 2008). Distinct vertical sinking velocities of settling tracers are prescribed and defined constant, with oxygen-dependent remineralization occurring at a constant rate across the entire water column. At lower O_2 levels than 0.5 micromol/L, remineralization of organic matter takes place via denitrification or sulphate reduction at prescribed constant rates. $CaCO_3$ is more soluble in cold waters and its dissolution is defined as the product of the calcite saturation state (Ω), a constant dissolution rate and the actual $CaCO_3$ concentration. Ω is the product of a constant Ca^{2+} concentration times the (prognostically calculated) carbonate ion (CO_3^{2-}) divided by the apparent solubility product of calcite. Opal dissolution is positively correlated with temperature and occurs over the whole water column. The inorganic carbon chemistry of HAMOCC is based on the approach of Maier-Reimer and Hasselmann (1987) in which the chemical constants have been modified and follow Goyet and Poisson (1989). Total alkalinity (TA) and total dissolved inorganic carbon (TCO_2) are prognostic variables distributed by the flow field in the same manner that the rest of the prognostic tracers. TCO_2 is the sum of carbonic acid ([H_2CO_3]), bicarbonate ([HCO_3^-]) and carbonate ([CO_3^{2-}]). TA considers carbonate and borate alkalinities and water dissociation products. The different carbonate species are diagnostically calculated using the mass action law for dissociation reactions (e.g., Goyet and Poisson 1989). TCO_2 and TA also vary due to different biogeochemi-

cal processes: TA remains constant whilst the uptake/release of atmospheric CO_2 by seawater increases/decreases TCO_2. Primary production reduces TCO_2 while TA rises with aerobic remineralization leading to the inverse effects. $CaCO_3$ formation/dissolution consumes/releases one mol of DIC (and therefore of TCO_2) and two mols of TA. Nitrogen fixation by photosynthetic algae and inorganic nitrogen consumption due to anaerobic remineralization also change the TA content (Zeebe and Wolf-Gladrow 2001).

HAMOCC contains a sediment module based on Heinze et al. (1999) that simulates the same processes described for the water column for the uppermost 14 cm of the ocean bottom. It considers 12 biologically active layers of increasing thickness and decreasing porosity with depth which lowest boundary includes a diagenetically consolidated burial layer. Deposition of detritus and matter from opal and $CaCO_3$ shells define the fluxes at the water-sediment upper boundary which are added to the sediment compartment. Then, the exchange of the dissolved compounds due to diffusive processes takes place between the pore water within the sediment layers and pelagic seawater. In case that the accumulated detritus or shell material within a layer exceeds a prescribed fraction defined for solid constituents, the surplus of these compounds is vertically redistributed so that it is storaged in a deeper sediment layer. This occurs until the tracer arrives to the burial layer.

A.4 Land Biosphere Module JSBACH

Land-atmosphere interaction is simulated with the land vegetation model JSBACH which is directly coupled to ECHAM6 and runs on the same horizontal grid (Reick et al. 2013). In order to represent subgrid heterogeneities, each grid cell is divided into *tiles* without a defined spatial location within the grid cell but an associated covered fraction. Each tiles includes a representation of the coexistent different types of land vegetation through the definition of the plant functional types (PFT). Thus, it is a fraction of a cell area what characterizes the extent of a specific veg-

etation type, instead of an occupied area itself. The PFT concept connects the various processes taking place over land surfaces and the mosaic of tiles because specific properties are defined for each PFT representing the processes considered in JSBACH. Some examples of the properties related to each PFT are the type of vegetation phenology, surface roughness, surface albedo and the photosynthetic pathway (C3, C4) of the type of vegetation. Uninhabitable regions such as rocky surfaces and deserts are represented by limiting the fraction of the grid cell area that is available for vegetation growth. The dynamic interaction between climate and the global distribution of land vegetation is simulated using a dynamic vegetation component (DYNVEG). In the following, some of the underlying principles governing the evolution of DYNVEG will be briefly described. The available space left free after the death of a plant might be used by a different type of plant. For PFTs this implies that the fraction of the area that it is used by a PFT might be reduced by processes such as natural death or external disturbances (fires and windthrows) and replaced by a different PFT. Competition to occupy this newly available fraction of the area is included. When uninhabitable regions shrink or broaden, the associated effects of the vegetation cover affect all vegetation types in the same manner and therefore no competition takes place. Without external disturbances, trees and shrubs dominate due to their competitive advantage of being able to take up the sunlight whilst darkening the land surface. However, compared to the evolution of grasses, the growth of woody plants is slow and therefore grasses can access faster newly available land after external disturbances.

Net primary production (NPP) is the amount of photosynthesized carbon by vegetation that enables growth and reproduction. Thus, a vegetation type with relatively high NPP implies a certain competitive advantage. That is why, competition between woody and non-woody vegetation types within the DYNVEG is parameterized based on their NPP so that PFTs with higher NPP migrate faster to free land surfaces. NPP definition follows the Biosphere-Energy-Transfer-Hydrology (BETHY) model (Knorr 2000). The PFTs are restricted by physiological constraints, that is ranges of environmental conditions that limit the establishment of the vegetation.

However, once the vegetation is established and unfavorable conditions emerge, these constraints do not prevent that vegetation evolves within this area. Bioclimatic limits are sensitive to climate change, these limits are actualized yearly. All PFTs can potentially develop in every location (i.e."seeds are everywhere") but vegetation settles only if the environmental conditions are such that NPP is positive during several years. Anthropogenic land cover change in JSBACH follows the New Hampshire Harmonized Land Use Protocol developed within the framework of the RCP scenarios (Hurtt et al. 2011). Instead of PFTs, the Harmonized Protocol makes use of two types of natural vegetation (primary and secondary) and two types of agricultural land cover (crops and pastures). This Protocol needs as input a sequence of land use transitions (Hurtt et al. 2006). Several adjustments had to be performed in order to run JSBACH under the Harmonized Protocol. For instance, the two types of natural vegetation were merged into one unique class. Thus, the land use transitions do only contain conversions between one unique type of natural vegetation, crops and pasture. Land changes from/to urban were not included in the simulations because JSBACH does not allow for this representation.

Aus dieser Dissertation hervorgegangene Vorveröffentlichungen

List of Publications

González, M. F. and T. Ilyina, 2016: Impacts of artificial ocean alkalinization on the carbon cycle and climate in Earth system simulations. Geophysical Research Letters, 43 (12), 6493-6502, doi:10.1002/2016GL068576